GEORG-AUGUST-UNIVERSITÄT
GÖTTINGEN

Fakultät für
Physik

Master's Thesis

Suche nach di-Higgs-Produktion im $\gamma\gamma WW^*$-Zerfallskanal mit dem 1-Lepton-Endzustand und der "boosted" Topologie bei ATLAS

Search for di-Higgs production in the $\gamma\gamma WW^*$ decay channel with the 1-lepton final state and the boosted topology at ATLAS

prepared by

Kira Abeling

from Twistringen

at the II. Physikalischen Institut

Thesis number:	II.Physik-UniGö-MSc-2017/08
Thesis period:	15th May 2017 until 26th October 2017
First referee:	Prof. Dr. Stan Lai
Second referee:	Prof. Dr. Arnulf Quadt

Abstract

Diese Arbeit behandelt die Suche nach di-Higgs-Produktion im $\gamma\gamma WW^*$ Zerfallskanal in den $\int \mathcal{L} dt = 36.1\,\text{fb}^{-1}$ aufgenommenen ATLAS Daten in 2015 und 2016 bei einer Schwerpunktsenergie von $\sqrt{s} = 13\,\text{TeV}$. Hierbei liegt der Fokus auf der Suche nach schweren Resonanzen mit einer Masse über $m_H \geq 500\,\text{GeV}$. Insbesondere der 1-Lepton Endzustand wird im Detail untersucht. Dadurch sind die Jets im Endzustand nicht mehr aufzulösen und werden als ein großer Jet zusammengefasst, was zu einer einzigartigen Signatur im Detektor und sehr geringer Statistik führt. Es wird eine Optimierung der Ereignisselektion durchgeführt. Die systematischen Unsicherheiten auf die zu erwartende Anzahl an Ereignissen in der Signalregion werden abgeschätzt. Um eine Kombination mit dem 0-Lepton Endzustand, welcher bisher nur mit statistischen Unsicherheiten untersucht worden ist, zu ermöglichen, wird dieser ebenfalls hinsichtlich der Systematiken berücksichtigt.

Da kein signifikanter Überschuss an Ereignissen oberhalb der Standardmodell Vorhersage in der Signalregion beobachtet wird, werden obere Grenzen auf die Wirkungsquerschnitte im 95% Vertrauensintervall gesetzt und für die beiden Endzustände kombiniert. Für die nicht resonante Produktion, die vom SM vorhergesagt wird, ergibt sich eine beobachtete (erwartete) Grenze von $\sigma_{gg\to hh} = 29\,(17)\,\text{pb}$. Diese entspricht 860 (510) mal der SM-Erwartung. Im Fall der resonanten Produktion liefert der $m_H = 1500\,\text{GeV}$ Massenpunkt die beste beobachtete (erwartete) Grenze mit $\sigma_{gg\to H} \times \mathcal{BR}_{H\to hh} = 2.6\,(1.6)\,\text{pb}$.

Abstract

In this thesis, the search for di-Higgs production in the $\gamma\gamma WW^*$ decay channel in $\int \mathcal{L} dt = 36.1\,\text{fb}^{-1}$ collected data by the ATLAS experiment in 2015 and 2016 at a centre-of-mass energy of $\sqrt{s} = 13\,\text{TeV}$ is presented. The search focusses on high resonance masses $m_H \geq 500\,\text{GeV}$ decaying in two Higgs bosons. Therefore, the jets in the final state cannot be resolved and are combined to form a large-R jet instead. In particular, the 1-lepton final state is investigated in detail resulting in a unique signature in the detector and little statistics remain. An optimisation of the event selection was performed. Systematic uncertainties on the event yields in the signal region also are evaluated. The search results are combined with those from the 0-lepton final state, where systematic uncertainties are also evaluated in the context of these studies.

Since no significant excess of events above the Standard Model prediction is found in the signal region, upper limits on the cross sections are set at the 95% confidence interval and combined for the two final states. For the non-resonant production as predicted by the Standard Model, a limit of $\sigma_{gg\to hh} = 29\,(17)\,\text{pb}$ is observed (expected). This corresponds to 860 (510) times the SM prediction. In the case of the resonant production, the most stringent limit can be set on the $m_H = 1500\,\text{GeV}$ mass point with $\sigma_{gg\to H} \times \mathcal{BR}_{H\to hh} = 2.6\,(1.6)\,\text{pb}$ observed (expected).

Contents

Nomenclature

Terminologies

Abbreviation	Meaning
SM	Standard Model of Particle Physics
MC	Monte-Carlo
BEH	Brout-Englert-Higgs
MSSM	Minimal SuperSymmetric Model
2HDM	Two Higgs Doublet Model
ggf	gluon-gluon-fusion
VBF	vector-boson-fusion
Wh	W associated Higgs production
Zh	Z associated Higgs production
$t\bar{t}h$	$t\bar{t}$ pair associated Higgs production

Particles

Abbreviation	Particle
h	light or SM-like Higgs boson
H	heavy, CP-even Higgs boson
A	CP-odd Higgs boson
$H^{\pm}$	charged Higgs boson
γ	photon
W	charged boson of the electroweak force
Z	neutral boson of the electroweak force
g	gluon
ℓ	lepton (electron or muon)
e	electron

Abbreviation	**Particle**
μ	muon
τ	tau lepton
ν	neutrino
J	large-R jet
j	small-R jet
q	quark
t	top quark
b	bottom quark
c	charm quark
s	strange quark
u	up quark
d	down quark

Quantities

Abbreviation	**Quantity**	**Unit**
c	speed of light in vacuum	(299 792 458)m/s
$\hbar$	reduced Planck constant	$(6.582119 \times 10^{-22})$ MeVs
m	invariant mass	GeV/c^2
E_T	transverse energy	GeV
p_T	transverse momentum	GeV/c
m_T	transverse mass	GeV/c^2
H_T	scalar sum of transverse energy	GeV/c
y	rapidity	–
η	pseudo-rapidity	–
ϕ	azimuthal angle	–
ΔR	distance in the detector	–
Σ	significance	–

1. Introduction

Centuries ago, the ancient Greeks tried to explain physics phenomena with smaller, indivisible particles called atoms. Over the years, many elements were discovered and the corresponding atoms referred to such indivisible particles. Up to a certain point, this theory was shown to be an adequate description of nature. Nevertheless, it became clear that atoms are not indivisible, but composed of even smaller particles. These particles are the subject of modern particle physics and the Standard Model (SM), which is one of the most accurate and successful theories to date.

The SM is a quantum field theory that describes elementary particles of spin-$\frac{1}{2}$ called fermions which are the building blocks of matter, and gauge bosons, particles of spin-1 which are the mediators of the fundamental forces. Until 2012, one postulated particle was yet to be observed: the Higgs boson, h. This scalar particle is an excitation of the Brout-Englert-Higgs (BEH) field which provides an explanation of how the particles in the SM obtain their masses [1–3]. The discovery of a resonance in the di-photon and multi-lepton spectra by ATLAS [4] and CMS [5] therefore completed the particle content of the SM. The next steps in current research are to perform precision measurements of the attributes of the Higgs boson. One important test is to measure the strength of the self-coupling since this is crucial to fully confirm the SM-like nature of the Higgs boson or to provide evidence for physics beyond the SM. Additionally, the measurement allows a direct observation of the parameters of the Higgs potential.

Despite its success, the SM is not a theory of everything. The energy scales that are considered within the SM are not sensitive to the gravitational force which is several orders of magnitude weaker than the other forces coming from gauge fields. Therefore, gravitation is not included in the SM description of the universe. Another point that cannot be explained within the SM is the current composition of the universe. Only around 5% of the universe is made of visible matter and energy. Gravitational effects as well as measurements of the microwave background indicate that there should be around six times more matter than has been observed so far. Indeed, around 25% of the universe is made of dark matter, particles not included in the SM [6]. Additionally, the fact that nearly only matter but no anti-matter is present in the universe cannot be explained by

the CP violation observed so far [7, 8].

One major approach solving these issues is the extension of the SM with supersymmetric particles. Those particles are related to the SM particles as partners by the change from spin-$\frac{1}{2}$ to an integer-valued spin and vice versa [9–13]. Even in the simplest extension, known as the minimal supersymmetric model (MSSM), the Higgs sector must be modified since a single scalar can not couple to all fermions simultaneously [14–18]. Therefore, a two Higgs doublet model (2HDM) is introduced which leads to five scalars in total [19]: two charged, $H^{\pm}$, one neutral CP odd, A, and two neutral CP even Higgs bosons, h and H, whereby h refers to the lighter, CP even Higgs boson which is consistent with the discovered one. These additional scalars are a new source of possible CP violation in the Higgs sector and could provide insight in explaining the baryon asymmetry in the universe.

This thesis presents a search for events with two simultaneously produced Higgs bosons (di-Higgs events) in $\int \mathcal{L} \mathrm{d}t = 36.1\,\mathrm{fb}^{-1}$ of data collected by the ATLAS experiment in 2015 and 2016 at the LHC. Here, the production can proceed non-resonant by the self-coupling or a box diagram as predicted by the SM, respectively, or via the decay of a heavy Higgs boson, H. The $\gamma\gamma WW^*$ decay channel with the 1-lepton final state is investigated, meaning while one Higgs boson decays into two photons, the other is considered to decay in two W bosons of which one decays hadronically and one leptonically. The event selection is optimised for resonant masses larger than $m_H = 750\,\mathrm{GeV}$ and thus, exploits the boosted topologies in which the decay products are close together in the detector and are reconstructed as combined objects.

A more detailed discussion of the SM, the BEH mechanism and two-Higgs-doublet models can be found in the Sections 2.1 and 2.2. The phenomenology of di-Higgs events including the production modes and decay channels is described in Sec. 2.3. The third chapter gives an overview of the LHC (Sec. 3.1), the ATLAS detector (Sec. 3.2), the Monte Carlo simulation used in this analysis (Sec. 3.3) and an introduction to jet reconstruction, especially in the boosted topology (Sec. 3.4). In Ch. 4, the analysis is presented, including a detailed discussion of the event topology (Sec. 4.1), the general setup (Sec. 4.2), the object definitions (Sec. 4.3), the overlap removal (Sec. 4.4), the final event selection (Sec. 4.5), the continuum background estimation (Sec. 4.6) and the optimisation based on maximising the significance (Sec. 4.7). The next chapter then discusses the statistical interpretation of the search where upper limits on the cross section times branching ratio are set (Sec. 5.1). In Sec. 5.2, the systematic uncertainties are evaluated and taken into account in the following limit setting in Sec. 5.3. Chapter 6 concludes and discusses the results and gives an outlook on possible further analyses.

2. Theory and Phenomenology

This chapter gives an overview of the theoretical foundations of the Higgs sector in the Standard Model as well as in models beyond the Standard Model. Furthermore, the production modes of single-Higgs and di-Higgs events are discussed and the main Higgs decay channels are described.

2.1. The SM and the BEH-Mechanism

This section gives a brief introduction to the mechanisms of the Standard Model and, especially, the Brout-Englert-Higgs mechanism. A more detailed description can be found in textbooks such as [20, 21] or in reviews [22, 23].

The Standard Model

There are four known fundamental interactions between elementary particles: electromagnetic, weak, strong and gravitational. Only gravitation is not included in the Standard Model of Particle Physics (SM). The other known interactions are described by individual symmetry groups in the SM. In the 1970's, the electromagnetic force [24] and the weak force [25] were combined to form the electro-weak theory by Glashow, Salam and Weinberg [26–28]. The $SU(2)_L \times U(1)_Y$ symmetry group was used for the description of the combined interaction. To this end, the hypercharge was defined as

$$Y = 2Q - 2I_3, \tag{2.1}$$

whereby Q denotes the electrical charge and I_3 the third component of the weak isospin. Within a few years of the theory of electro-weak unification, the $SU(3)_C$ symmetry group was introduced to describe strong interactions [29, 30]. Here, C is a quantum number for the strong interaction known as colour.

Since the SM is a quantum field theory, all particles and forces are represented by such quantum fields. There is a distinction between matter fields, ψ, which result in spin-$\frac{1}{2}$

particles called fermions, and gauge fields, V_μ, which describe the individual forces and the corresponding mediators, spin-1 bosons.

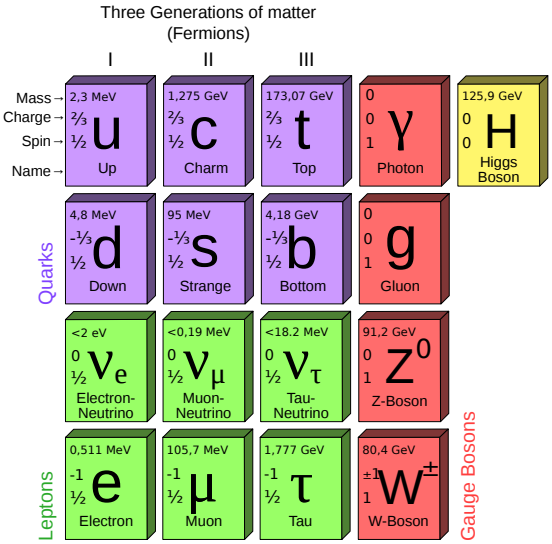

Figure 2.1.: Overview of all particles included in the SM. ©Wikimedia Commons

As depicted in Fig. 2.1, fermions are further separated into leptons and quarks, that are arranged in three generations each. The difference between these generations is the mass of the containing particles, while the charge and weak isospin stay constant among all generations. Since the weak force couples to the chirality of a particle, left-handed fermions must be treated differently from right-handed fermions. While the latter exist in weak isospin singlets, the left-handed fermions are placed in weak isospin doublets. In addition, quarks are placed in colour triplets and leptons in colour singlets, because only quarks participate in the strong interactions.

The interactions themselves are represented by gauge fields. In the electro-weak sector, one field, B_μ, corresponds to the generator of $U(1)_Y$, Y, and three fields, $W_\mu^{1,2,3}$, are related to $SU(2)_L$. Its generators are proportional to the Pauli matrices. This leads to four bosons, the photon, γ, the charged $W^\pm$-bosons and the neutral Z-boson. For strong interactions and, thus, the $SU(3)_C$ group, an octet of fields, $G_\mu^{1,\dots,8}$, is obtained. Here, the generators are proportional to the Gell-Mann matrices. The strong gauge fields result in eight gluons with different colour states, which will be in the following only referred to as "gluon", since colour is not directly observable. The field strengths are then given by

$$\begin{aligned} G^a_{\mu\nu} &= \partial_\mu G^a_\nu - \partial_\nu G^a_\mu + g_s f^{abc} G^b_\mu G^c_\nu \\ W^a_{\mu\nu} &= \partial_\mu W^a_\nu - \partial_\nu W^a_\mu + g_2 \varepsilon^{abc} W^b_\mu W^c_\nu \\ B_{\mu\nu} &= \partial_\mu B_\nu - \partial_\nu B_\mu. \end{aligned} \tag{2.2}$$

The last term for $G^a_{\mu\nu}$ and $W^a_{\mu\nu}$ results from the commutation relations, whereby g_s and g_2 denote the coupling constants and f^{abc} and ε^{abc} are tensors to ensure the correct structure of the commutators. Since $SU(2)$ and $SU(3)$ are non-abelian, self-interactions between their gauge fields are required which lead to triple and quartic gauge boson couplings.

The coupling between matter fields and gauge fields is realised by the covariant derivative defined as

$$D_\mu \psi = \Big(\partial_\mu - \underbrace{i g_s T_a G^a_\mu}_{SU(3)_C} - \underbrace{i g_2 T_b W^b_\mu}_{SU(2)_L} - \underbrace{i g_1 T B_\mu}_{U(1)_Y}\Big)\psi, \tag{2.3}$$

whereby T stands for the generator of the corresponding symmetry group. Since leptons do not interact strongly, the second term would be equal to zero for lepton spinors. Using the Lagrange formalism, the following SM Lagrangian is obtained

$$\mathcal{L} = \underbrace{-\tfrac{1}{4} G^a_{\mu\nu} G^{\mu\nu}_a - \tfrac{1}{4} W^a_{\mu\nu} W^{\mu\nu}_a - \tfrac{1}{4} B_{\mu\nu} B^{\mu\nu}}_{\text{kinematics of gauge fields}} + \underbrace{\overline{\psi}^f_L i D_\mu \gamma^\mu \psi^f_L + \overline{\psi}^f_R i D_\mu \gamma^\mu \psi^f_R}_{\text{kinematics and interactions of fermions}} . \tag{2.4}$$

Here, γ^μ denotes the Dirac matrices and ψ^f_L stands for all left-handed fermion doublets and ψ^f_R for the right-handed fermion singlets. The covariant derivative differs if f corresponds to a lepton or to a quark as mentioned above.

This Lagrangian is invariant under local $SU(3)_C \times SU(2)_L \times U(1)_Y$ gauge transformations but misses an important contribution. No mass terms for any of the fields are included, although most fermions as well as the $W^\pm$-bosons and the Z-boson have a non-zero mass [22, 31, 32]. According to theory, gauge bosons should all be massless as in the case of the gluon and photon. Regarding the strong interactions, adding mass terms for the quarks leaves the Lagrangian invariant under $SU(3)_C$ transformation as the gluon itself is massless. In the electro-weak sector, this is not the case. Apart from the massive gauge bosons, adding the mass for the fermions results in terms such as

$$-m\left(\overline{\psi}_R \psi_L + \overline{\psi}_L \psi_R\right) \tag{2.5}$$

which are not invariant under $SU(2)_L$ transformations, since ψ_R as isospin singlet behaves differently than the doublet ψ_L. Therefore, the electro-weak theory must be broken to preserve the SM in general and a way to generate masses without violating $SU(2)_L \times U(1)_Y$ gauge invariance is needed. This is provided by the BEH mechanism which is discussed in the following.

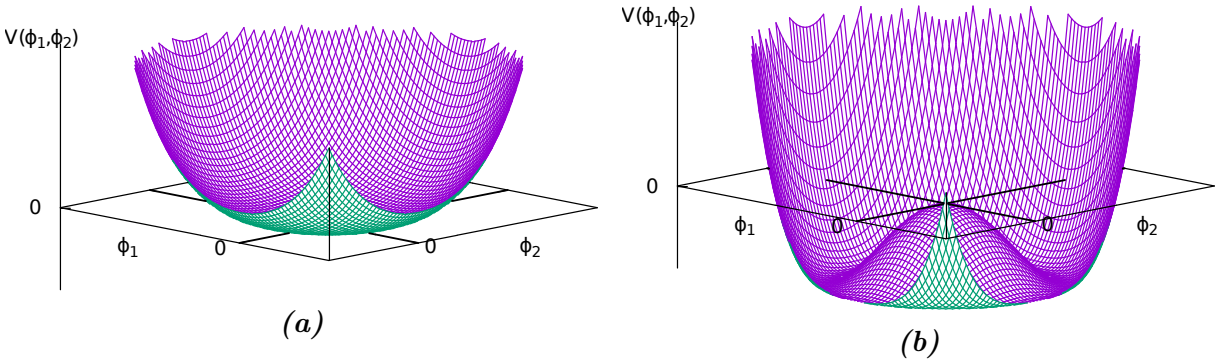

Figure 2.2.: The Higgs potential $V(\phi)$ for (a) $\mu^2 > 0$ and (b) $\mu^2 < 0$ for a complex scalar field $\phi = \phi_1 + i\phi_2$.

The BEH-Mechanism

In the 1960's, a solution to the problem of particle masses was formed simultaneously by Guralnik, Hagen, Kibble, Brout, Englert and Higgs [1–3]. This is referred to as the Brout-Englert-Higgs (BEH) mechanism which introduces a complex scalar doublet

$$\Phi = \begin{pmatrix} \phi^+ \\ \phi^0 \end{pmatrix} = \frac{1}{\sqrt{2}} \begin{pmatrix} \phi_1 + i\phi_2 \\ \phi_3 + i\phi_4 \end{pmatrix} \tag{2.6}$$

to give mass to the bosons of the electro-weak theory. This scalar doublet yields an extra term in the Lagrangian of the form

$$\mathcal{L}_h = \partial_\mu \Phi^\dagger \partial^\mu \Phi - V(\Phi) \text{ with } V(\Phi) = \mu^2 \Phi^\dagger \Phi + \lambda \left(\Phi^\dagger \Phi\right)^2. \tag{2.7}$$

There are two free parameters in the potential, V, whereby λ is restricted to positive values to ensure that the potential is bounded from below. The remaining parameter μ^2, determines the form of the potential as depicted in Fig. 2.2 for a complex scalar field $\phi = \phi_1 + i\phi_2$. If μ^2 is positive, the potential has only one minimum, while for negative values, the potential has an infinite set of equivalent minima that occur at non-zero field values. The vacuum state chooses one of those spontaneously and thus, breaks the symmetry of the Lagrangian. As per convention, the minimum is assumed to be real and it has to be uncharged to preserve the exact symmetry of quantum electrodynamics

$$\Phi_0 = \begin{pmatrix} 0 \\ v \end{pmatrix}, \text{ whereby } v = \sqrt{\frac{-\mu^2}{\lambda}}. \tag{2.8}$$

To interpret the Lagrangian correctly, the fields are expanded around the minimum

$$\Phi = \frac{1}{\sqrt{2}} \begin{pmatrix} \theta_2(x) + i\theta_1(x) \\ v + h(x) - i\theta_3(x) \end{pmatrix} = \frac{1}{\sqrt{2}} e^{i\theta_a(x)\sigma^a} \begin{pmatrix} 0 \\ v + h(x) \end{pmatrix}, \tag{2.9}$$

whereby σ^a refers to the Pauli matrices and θ_a to the massless, scalar Goldstone bosons [33, 34]. In a unitary gauge, the fields $\theta_a(x)$ are absorbed in the electro-weak bosonic fields. To couple the electro-weak fields to the remaining scalar field, $h(x)$, the derivative in the Lagrangian (Eq. 2.7) is replaced by the covariant derivative (Eq. 2.3) without considering the strong interaction term. Defining the observed electro-weak bosons as mass eigenstates of W_μ^a and B_μ

$$W_\mu^\pm = \frac{1}{\sqrt{2}}(W_\mu^1 \mp iW_\mu^2),\ Z_\mu = \frac{g_2 W_\mu^3 - g_1 B_\mu}{\sqrt{g_2^2 + g_1^2}},\ \text{and}\ A_\mu = \frac{g_2 W_\mu^3 + g_1 B_\mu}{\sqrt{g_2^2 + g_1^2}}, \tag{2.10}$$

the Lagrangian can be written as

$$\begin{aligned} \mathcal{L}_h = &\underbrace{\frac{1}{2}\partial_\mu h \partial^\mu h - \lambda v^2 h^2}_{\text{massive scalar}} \underbrace{-\lambda v h^3 - \frac{1}{4}\lambda h^4}_{\text{self-interactions}} + \underbrace{\frac{g_2^2 v^2}{4} W_\mu^- W^{+\mu} + \frac{v^2}{8(g_2^2 + g_1^2)} Z_\mu Z^\mu}_{\text{mass terms for gauge bosons}} \\ &+ \underbrace{\frac{g_2^2 v}{2} W_\mu^- W^{+\mu} h + \frac{v}{4(g_2^2 + g_1^2)} Z_\mu Z^\mu h + \frac{g_2^2}{4} W_\mu^- W^{+\mu} h^2 + \frac{1}{8(g_2^2 + g_1^2)} Z_\mu Z^\mu h^2}_{\text{interactions between the scalar and gauge fields}}. \end{aligned} \tag{2.11}$$

As mentioned, the $W_\mu^\pm$ and Z_μ gauge bosons and the scalar Higgs boson, h, have mass while the photon, A_μ, remains massless

$$m_h = \sqrt{2\lambda v^2},\ m_W = \frac{g_2 v}{2},\ m_Z = \frac{v}{2\sqrt{g_2^2 + g_1^2}},\ m_A = 0. \tag{2.12}$$

Additionally, triple and quartic couplings between the massive gauge bosons and the Higgs boson as well as self-couplings of the Higgs boson itself occur. These self-couplings are depicted in Fig. 2.3. Here, the triple coupling can be realised at tree level and has thus a greater impact on the di-Higgs production than the quartic coupling which will be neglected.

For fermions, the interactions are described by an additional term in the Lagrangian

$$\mathcal{L}_f = -\lambda_f \left(\overline{\psi}_L^f \Phi \psi_R^f + \overline{\psi}_R^f \Phi \psi_L^f \right) = -\frac{\lambda_f}{\sqrt{2}}(v + h) \left(\overline{f}_L f_R + \overline{f}_R f_L \right) \tag{2.13}$$

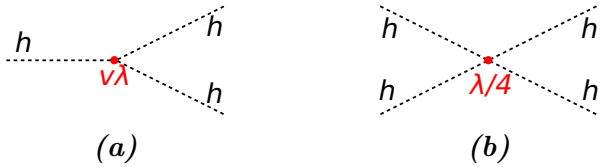

Figure 2.3.: Feynman diagrams of the (a) triple and (b) quartic self-coupling of the Higgs boson. The corresponding coupling strength is given in red.

resulting in fermion masses of

$$m_f = \frac{\lambda_f v}{\sqrt{2}}, \tag{2.14}$$

whereby λ_f denotes the Yukawa coupling [28].

In 2012, a scalar resonance was observed by ATLAS and CMS [4, 5]. To date, no deviations from the quantities predicted by the SM have been observed. Therefore, this boson is considered to be the Higgs boson with a measured mass of $m_h = 125.09 \pm 0.24\,\text{GeV}$ [35].

2.2. Two-Higgs-Doublet Models

The Higgs Sector in the Minimal Supersymmetric Model

As mentioned in Ch. 1, many physical phenomena cannot be explained within the SM. Therefore, extensions to the SM are needed. One of the most discussed extensions is Supersymmetry (SUSY) [9–13], which introduces a partner for every currently known particle with the spin differing by one half unit. These partners, especially the neutralinos, are promising dark matter candidates. SUSY is also able to solve the hierarchy problem which regards the large radiative corrections to the Higgs mass with an unnatural cancellation of $\mathcal{O}(10^{-30})$ to the Planck scale which can be cancelled by introducing further scalar bosons [36, 37]. Furthermore, all known interactions including gravity can be described within this extension. Therefore, this section gives a brief overview of a special case of SUSY, the Minimal Supersymmetric Model (MSSM) and, especially, of the corresponding Higgs sector [14–18]. More detailed reviews can be found in [38] or [39].

The MSSM is based on the same $SU(3)_C \times SU(2)_L \times U(1)_Y$ symmetry as the SM with an additional conserved, discrete symmetry, R-parity [40]. This symmetry enforces lepton and baryon number conservation and leads to the stability of the lightest SUSY particle. Only minimal particle content is added which are the supersymmetric partners of the SM particles. Since no SUSY particles have been observed yet, they must have a much larger

mass than their SM partners, if realized in nature. Therefore, SUSY must be broken in this case. In the Lagrangian, a collection of soft terms [41–44] are added including mass and coupling terms for the SUSY particles and the Higgs bosons. Together with intergenerational mixing and complex phases, this model results in 105 free parameters in addition to the 19 free parameters of the SM [45, 46]. Using constraints from experimental observations, the number of new free parameters is reduced to 22 [47].

In contrast to the SM, one complex scalar doublet is not sufficient to break the electroweak symmetry in the MSSM. Instead, two complex scalar doublets of opposite hypercharge are needed:

$$\Phi_1 = \begin{pmatrix} \phi_1^0 \\ \phi_1^- \end{pmatrix} \text{ for } Y = -1 \text{ and } \Phi_2 = \begin{pmatrix} \phi_2^+ \\ \phi_2^0 \end{pmatrix} \text{ for } Y = +1, \tag{2.15}$$

because a single doublet cannot give mass to up-type and down-type fermions simultaneously and cancel chiral anomalies [14–18]. The fields, Φ_1 and Φ_2, result in two vacuum expectation values, v_1 and v_2, whereby

$$\sqrt{v_1^2 + v_2^2} = v. \tag{2.16}$$

One also defines the parameter

$$\tan\beta := \frac{v_2}{v_1}, \tag{2.17}$$

since the phenomenology of the MSSM highly depends on this quantity. Expanding the fields around the vacuum state,

$$\Phi_1 = \frac{1}{\sqrt{2}} \begin{pmatrix} v_1 + h_1 + i\theta_1 \\ \phi_1^- \end{pmatrix} \text{ and } \Phi_2 = \frac{1}{\sqrt{2}} \begin{pmatrix} \phi_2^+ \\ v_2 + h_2 + i\theta_2 \end{pmatrix}, \tag{2.18}$$

the CP-even Higgs bosons are obtained from the real terms and CP-odd Higgs bosons as well as Goldstone bosons from the imaginary terms. The physical particles can then be calculated via

$$\begin{pmatrix} G^0 \\ A \end{pmatrix} = \begin{pmatrix} \cos\beta & \sin\beta \\ -\sin\beta & \cos\beta \end{pmatrix} \begin{pmatrix} \theta_1 \\ \theta_2 \end{pmatrix}, \quad \begin{pmatrix} G^\pm \\ H^\pm \end{pmatrix} = \begin{pmatrix} \cos\beta & \sin\beta \\ -\sin\beta & \cos\beta \end{pmatrix} \begin{pmatrix} \phi_1^\pm \\ \phi_2^\pm \end{pmatrix},$$
$$\text{and } \begin{pmatrix} H \\ h \end{pmatrix} = \begin{pmatrix} \cos\alpha & \sin\alpha \\ -\sin\alpha & \cos\alpha \end{pmatrix} \begin{pmatrix} h_1 \\ h_2 \end{pmatrix}, \tag{2.19}$$

whereby α denotes the mixing angle between the CP-even Higgs bosons, G^0 and $G^\pm$, re-

spectively denote the Goldstone bosons which are absorbed by the longitudinal component of the electro-weak bosons. Thus, this results in five Higgs-bosons: the light and heavy CP-even Higgs bosons, h and H, the neutral CP-odd Higgs boson, A, and the charged Higgs-bosons, $H^{\pm}$. The light CP-even Higgs boson can be identified as the known scalar boson, although the pure SM Higgs boson would be a mixture of both, h and H

$$h^{\mathrm{SM}} = h\sin(\alpha-\beta) - H\cos(\alpha-\beta). \tag{2.20}$$

Due to the constraints on the MSSM, from the six free parameters, four masses and two angles, only two parameters are independent at tree level, conventionally chosen to be m_A and $\tan\beta$. Given the phenomenological predictions of the MSSM for the Higgs sector, searches for the other Higgs bosons are also interesting. In particular, the heavy Higgs boson, H, can decay in two light Higgs bosons, h, and leaving unique signatures in the detector.

Two-Higgs-Doublet Models

Models with two Higgs doublets (2HDM) can also exist independently of supersymmetry. A general 2HDM [19] can have complex vacuum states with 14 free parameters. The minima can be CP-conserving, CP-violating or also charge-violating. For most 2HDMs, it is sufficient to make simplifying assumptions such as CP-conservation and cancellation of quartic terms which are odd in either of the doublets through discrete symmetries. The most general potential for two complex doublets, Φ_1 and Φ_2, with a hypercharge of $Y = +1$ is [48]

$$\begin{aligned} V = {} & \lambda_1\left(|\Phi_1|^2 - v_1^2\right)^2 + \lambda_2\left(|\Phi_2|^2 - v_2^2\right)^2 + \lambda_3\left(|\Phi_1|^2 - v_1^2 + |\Phi_2|^2 - v_2^2\right)^2 \\ & + \lambda_4\left(|\Phi_1|^2|\Phi_2|^2 - |\Phi_1^\dagger\Phi_2|^2\right) + \lambda_5\left(\mathrm{Re}(\Phi_1^\dagger\Phi_2) - v_1v_2\right)^2 + \lambda_6\left(\mathrm{Im}(\Phi_1^\dagger\Phi_2)\right)^2, \end{aligned} \tag{2.21}$$

where all parameters λ_i are real. As in the MSSM, this results in two vacuum expectation values, v_1 and v_2, fulfilling Eq. 2.16 and Eq. 2.17. Following the procedure from above and rewriting the fields with respect to their ground state,

$$\Phi_1 = \begin{pmatrix} \phi_1^+ \\ v_1 + h_1 + i\theta_1 \end{pmatrix} \text{ and } \Phi_2 = \begin{pmatrix} \phi_2^+ \\ v_2 + h_2 + i\theta_2 \end{pmatrix}, \tag{2.22}$$

one can derive the mass matrices and calculate the parameters λ_i depending on the masses and angles [49]

$$\begin{aligned}
\lambda_1 &= \frac{1}{4\cos^2(\beta)v^2}\left(\cos^2(\alpha)m_H^2 + \sin^2(\alpha)m_h^2\right) - \frac{\sin(2\alpha)}{\sin(2\beta)}\,\frac{m_H^2 - m_h^2}{4v^2} + \frac{\lambda_5}{4}\left(1 - \frac{\sin^2(\beta)}{\cos^2(\beta)}\right) ,\\
\lambda_2 &= \frac{1}{4\sin^2(\beta)v^2}\left(\sin^2(\alpha)m_H^2 + \cos^2(\alpha)m_h^2\right) - \frac{\sin(2\alpha)}{\sin(2\beta)}\,\frac{m_H^2 - m_h^2}{4v^2} + \frac{\lambda_5}{4}\left(1 - \frac{\cos^2(\beta)}{\sin^2(\beta)}\right) ,\\
\lambda_3 &= \frac{\sin(2\alpha)}{\sin(2\beta)}\,\frac{m_H^2 - m_h^2}{4v^2} - \frac{\lambda_5}{4} , \quad \lambda_4 = \frac{m_{H^\pm}^2}{v^2} , \quad \lambda_6 = \frac{m_A^2}{v^2}
\end{aligned} \tag{2.23}$$

In contrast to the MSSM, all masses and angles are independent, resulting in six free parameters. Furthermore, if $\Phi_1 \to -\Phi_1$ is fulfilled, λ_5 vanishes, otherwise λ_5 is an additional free parameter, related to the fact that $\tan\beta$ is not constrained originally.

Assuming that flavour changing neutral currents are naturally absent at tree level, which is consistent with observations to date, only four possible types of 2HDMs remain (see Tab. 2.1). While the masses are generally model independent, the couplings to fermions are not, as shown in Tab. 2.2.

Model	ψ_R^u	ψ_R^d	ψ_R^l
Type I	Φ_2	Φ_2	Φ_2
Type II	Φ_2	Φ_1	Φ_1
Lepton-specific	Φ_2	Φ_2	Φ_1
Flipped	Φ_2	Φ_1	Φ_2

Table 2.1.: 2HDMs, which include neutral flavour conversation, and the coupling of the Higgs doublets to the different types of fermions. By convention up-type quarks always couple to Φ_2.

In the type I 2HDMs [50, 51], all quarks couple to one doublet, which is conventionally chosen to be Φ_2. An interesting limit of the model is $\alpha = \frac{\pi}{2}$, the fermiophobic limit, where all fermions completely decouple from the lightest Higgs. In type II 2HDMs [51, 52], the coupling of up-type quarks is assigned to one Higgs doublet, Φ_2 per convention, the down-type quarks to the other, Φ_1 accordingly. In both cases, type I and type II, charged leptons are treated in the same manner as down-type quarks. Since the Higgs sector in the MSSM can be regarded as a highly constrained type II 2HDM, it is the most commonly studied model of these four.

There are also two other models of 2HDMs which treat leptons differently [53, 54]. In the lepton-specific 2HDM, all quarks couple to Φ_2, while the leptons couple to Φ_1. The least commonly studied model is the flipped model, wherein the quarks are treated as in the type II 2HDM, but the leptons couple to Φ_2 as the up-type quarks do.

A more detailed view and further models including flavour changing neutral currents, which are outside the scope of this thesis, can be found in [55].

Fermion	Boson	Coupling in 2HDM			
		Type I	Type II	Lepton-specific	Flipped
ψ^u	h	$\cos\alpha/\sin\beta$	$\cos\alpha/\sin\beta$	$\cos\alpha/\sin\beta$	$\cos\alpha/\sin\beta$
	H	$\sin\alpha/\sin\beta$	$\sin\alpha/\sin\beta$	$\sin\alpha/\sin\beta$	$\sin\alpha/\sin\beta$
	A	$\cot\beta$	$\cot\beta$	$\cot\beta$	$\cot\beta$
ψ^d	h	$\cos\alpha/\sin\beta$	$-\sin\alpha/\cos\beta$	$\cos\alpha/\sin\beta$	$-\sin\alpha/\cos\beta$
	H	$\sin\alpha/\sin\beta$	$\cos\alpha/\cos\beta$	$\sin\alpha/\sin\beta$	$\cos\alpha/\cos\beta$
	A	$-\cot\beta$	$\tan\beta$	$-\cot\beta$	$\tan\beta$
ψ^l	h	$\cos\alpha/\sin\beta$	$-\sin\alpha/\cos\beta$	$-\sin\alpha/\cos\beta$	$\cos\alpha/\sin\beta$
	H	$\sin\alpha/\sin\beta$	$\cos\alpha/\cos\beta$	$\cos\alpha/\cos\beta$	$\sin\alpha/\sin\beta$
	A	$-\cot\beta$	$\tan\beta$	$\tan\beta$	$-\cot\beta$

Table 2.2.: Yukawa couplings for up-type and down-type quarks and leptons to the neutral Higgs bosons h, H and A with respect to the SM in the four types of 2HDMs. The coupling of $H^\pm$ follows the coupling to A [55].

2.3. Production Modes and Decay Channels

Single-Higgs Production

The SM Higgs boson can be produced in various ways at the LHC. The four dominant mechanisms, which are considered in the analysis, are depicted in Fig. 2.4.

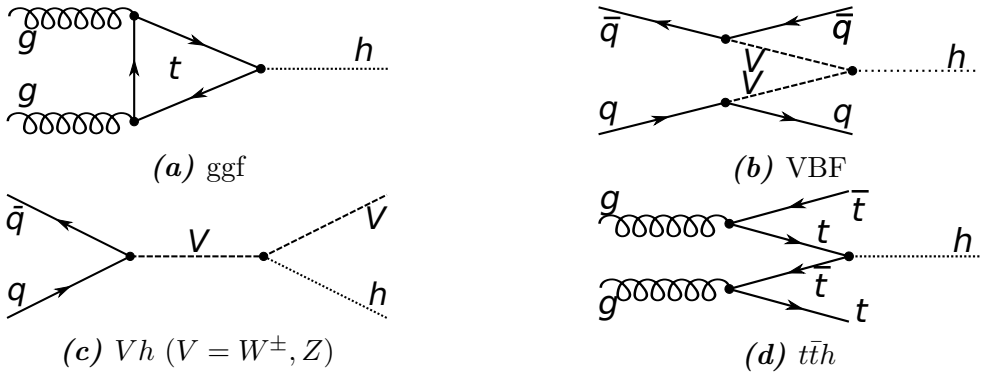

(a) ggf ***(b)*** VBF ***(c)*** Vh $(V = W^\pm, Z)$ ***(d)*** $t\bar{t}h$

Figure 2.4.: Main SM production mechanisms of the Higgs boson.

Considering proton-proton collisions at a centre-of-mass energy of $\sqrt{s} = 13\,\text{TeV}$ which reflects the current run conditions at the LHC (see Sec. 3.1), the largest cross section with

$\sigma = 44.08\,\text{pb}$ [56] is provided by gluon-gluon fusion (ggf, Fig. 2.4 (a)). Here, two gluons fuse into a quark loop which is dominated by top quarks and results in a Higgs boson. For the second most dominant process, vector boson fusion (VBF, Fig. 2.4 (b)), the cross section is with $\sigma = 3.78\,\text{pb}$ [56] already one order of magnitude smaller than for ggf. In the VBF, two quarks each radiate a vector boson, either W or Z, which then annihilate and produce a Higgs boson. Here, the quarks are scattered collinearly to the beams, resulting in a characteristic signal signature. Another possibility is associated Higgs boson production with a vector boson (Vh with $V = W,\ Z$, Fig. 2.4 (c)), whereby the vector boson can either be a $W^{\pm}$-boson ($\sigma = 1.37\,\text{pb}$ [56]) or a Z-boson ($\sigma = 0.88\,\text{pb}$ [56]). The vector boson is produced in the annihilation of two quarks and then radiates a Higgs boson. Therefore, both the Higgs boson as well as the vector boson leave a signature in the detector. With only $\sigma = 0.51\,\text{pb}$, the lowest cross section of the considered mechanisms is provided by the Higgs production in association with a top-anti-top quark pair ($t\bar{t}h$, Fig. 2.4 (d)). In this case, two gluons each split up into a $t\bar{t}$ pair. The Higgs boson is then formed by the annihilation of a top-quark and anti-top-quark, while the other decay and appear as a typical $t\bar{t}$ final state in the detector.

Di-Higgs Production

In contrast to single-Higgs production, di-Higgs production is only classified as resonant and non-resonant with two gluons in the initial state. The Feynman-diagrams of these production modes are shown in Fig. 2.5.

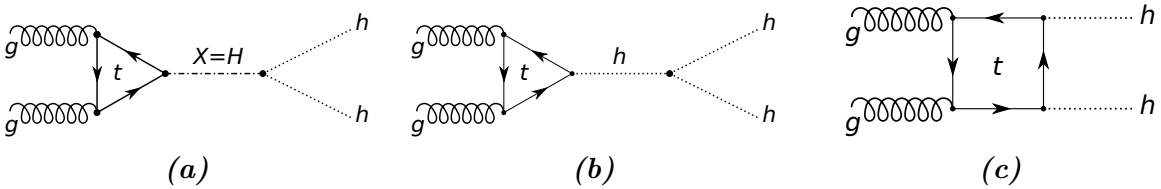

Figure 2.5.: Feynman diagrams of (a) the resonant and (b) and (c) the non-resonant di-Higgs production modes.

The resonant mode describes the decay of a heavier, scalar particle X, which is in this analysis chosen to be the heavy Higgs boson, H, as introduced by 2HDMs. The advantage of this production mode is that the kinematics of the light Higgs bosons and their decay products depend on the resonant mass which could also be reconstructed by combining all particles in the final state. Since there are no stringent constraints on the mass in 2HDMs, it can vary over a large range.

The non-resonant production mode is predicted by the SM (see Eq. 2.11) in the triple self-coupling of the Higgs boson. Therefore, measuring the coupling strength is a direct

measurement of λ and thus, of the Higgs potential. Since λ also enters the mass of the Higgs boson, an indirect measurement was already performed and a comparison to the direct measurement is a crucial test of the SM.

The self-coupling interferes destructively with the box diagram shown in Fig. 2.5 (c), resulting in a small cross section of $\sigma^{\text{SM}}_{gg\to hh}(\sqrt{s} = 13\,\text{TeV}) = 33.45\,\text{fb}$, which is out of reach of the current LHC data set [57, 58]. However, theories beyond the SM can change the coupling or interfere constructively and thus enhance the cross section to a measurable range. Therefore, a measurement of the non-resonant cross section is sensitive to new physics without specifying an exact model.

Decay Channels

The Higgs boson is an unstable particle and therefore decays after a short time into lighter particles. With a mass of $m_h = 125.09\,\text{GeV}$, it can decay to all massive particles of the SM except the top quark, which is too heavy. The main branching ratios are shown in Fig. 2.6 as a function of the Higgs mass and in Tab. 2.3 for $m_h = 125.09\,\text{GeV}$.

The highest branching ratio is given by the Higgs decaying into a $b\bar{b}$ pair, since two on-shell bottom quarks can be produced within the decay. It is followed by the decay in two W-bosons, whereby one of these is off-shell and, thus, reduces the probability of this decay. Although gluons are massless, the Higgs boson can decay to a pair of gluons via a top quark loop. Nonetheless, this channel will not be considered in further discussions because its overwhelming background at hadron colliders makes any detection impossible. The decay into a τ^+-τ^- pair is the leading channel to observe a Higgs decay into leptons. With a significantly lower branching ratio, the decay into two photons is still one of the discovery channels due to its excellent mass resolution and the small and well-modelled background. As for gluons, the coupling to photons is realised by a (top) quark loop or an additional W-boson loop which interfere such that this branching ratio is a factor of forty lower that the decay into gluons. In the following, the point-like effective coupling to photons will be considered without mentioning the loop explicitly.

In this thesis, di-Higgs events, in which one Higgs boson decays into photons and the other into W-bosons, are investigated. As W-bosons are also not stable and decay further into quarks or leptons, three final states are possible and distinguished by the number of charged leptons (electron or muon):

- 0-lepton final state – both W-bosons decay hadronically, this channel has the highest branching ratio and a contribution from the Higgs decay into two Z-bosons also decaying hadronically.

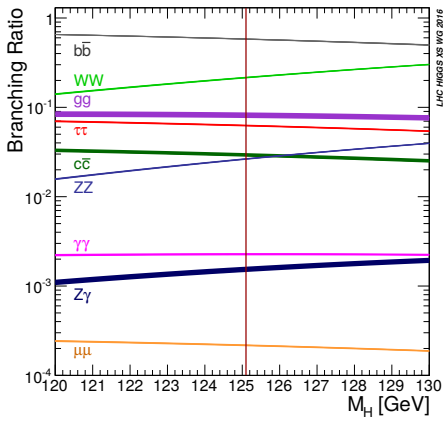

Figure 2.6.: SM Higgs branching ratios in dependency of the Higgs mass [56]. The red line indicates the measured Higgs mass of $m_H = 125.09\,\text{GeV}$.

decay mode	$\mathcal{BR}$ [%]
$b\bar{b}$	58.09
WW^*	21.52
$(4q$	10.97)
gg	8.18
$(\ell\nu qq$	6.31)
$\tau\tau$	6.26
$c\bar{c}$	2.88
ZZ^*	2.64
$(2\ell 2\nu$	1.06)
$\gamma\gamma$	0.23

Table 2.3.: SM Higgs branching ratios for $m_h = 125.09\,\text{GeV}$ [56]. The decay modes in parantheses are secondary decays (from WW^* and ZZ^*).

- 1-lepton final state – only one W-boson decays hadronically, the other leptonically, resulting in a lower branching ratio but unique signature in the detector.
- 2-lepton final state – both W-bosons decay leptonically resulting in the lowest branching ratio, although there is a contribution from ZZ^* decaying into a pair of neutrinos and charged leptons, respectively.

The branching ratios for the secondary decays are also stated in Tab. 2.3 in parentheses. In this analysis, mainly the 1-lepton final state is investigated but the 0-lepton final state is also considered in Ch. 5. The overall branching ratio for the $\gamma\gamma WW^*$ channel in the 1-lepton final state is

$$\mathcal{BR}(hh \to \gamma\gamma\ell\nu qq) = 2.9 \times 10^{-4}. \tag{2.24}$$

The complete event topology will be discussed in more detail in Sec. 4.1.

3. Experimental Setup

In this chapter, the experimental setup is presented. This includes a brief introduction of the LHC and the ATLAS experiment where the data analysed in this thesis is collected. Furthermore, the procedure for Monte Carlo event generation is described and the concept of jet reconstruction in the boosted topology is discussed.

3.1. The LHC

The Large Hadron Collider (LHC) [59, 60] is a circular proton-proton and heavy ion synchrotron operated by the European Organisation for Nuclear Research (CERN) in the tunnel originally used by the Large Electron Positron Collider (LEP) [61] located at the Swiss-French Border close to Geneva. With a circumference of 27 km, it is the largest collider in existence.

In 2010, the LHC started running with a centre-of-mass energy of $\sqrt{s} = 7\,\text{TeV}$, which was increased to $\sqrt{s} = 8\,\text{TeV}$ in 2012. The years from 2010 to 2012 are referred to as Run I [62]. After a shut down to upgrade the detectors and accelerator, Run II began in 2015. Since then, the centre-of-mass energy has been $\sqrt{s} = 13\,\text{TeV}$ but will increase to $\sqrt{s} = 14\,\text{TeV}$ later [63].

In contrast to LEP, the particles accelerated in the LHC have the same charge. Therefore, each beam technically needs its own ring with opposite magnetic fields. Since the existing tunnel limits the space for additional devices, only one tube was added and nearly all of the dipole magnets follow the design of twin-bore magnets which were proposed in 1971 [64]. This saves space but results in complicated dipole structures, which are coupled magnetically as well as mechanically.

As in other large accelerators, superconducting magnets are constructed out of superconducting cables made of niobium-titanium. The essential dipole field of over $B = 8\,\text{T}$ necessary to keep the protons at maximum energy on track is not attainable with the hitherto operating temperature of 4.2 K. Instead of supercritical, superfluid helium at a temperature of 1.9 K cools the magnets. Additionally, quadrupole magnets are implemented to (de-)focus the beam such that the particle losses are minimised and a high

particle density is provided in the interaction points. Further magnets are used to apply small corrections to the beam to increase beam stability.

In addition to the high centre-of-mass energy, a high luminosity is one of the performance goals. The aim is to reach a peak luminosity of $\mathcal{L} = 10^{34}\,\mathrm{cm}^{-2}\mathrm{s}^{-1}$ for proton-proton collisions. This can only be realised with a large number of bunches with a large number of particles per bunch. At the LHC, the physical limits are 1.15×10^{11} particles per bunch and 2808 bunches per beam. Another design parameter of the LHC is the short bunch spacing time which allows collisions every 25 ns. Due to interactions and other losses, the luminosity does not remain constant over time but has a lifetime of approximately 15 h.

Four main experiments are located at the LHC. The two larger experiments are ATLAS [65] and CMS [66], which collect the largest amount of data to test the SM with precision measurements and search for possible extensions of it. The Higgs boson was also discovered by both experiments simultaneously in 2012 [4, 5]. A smaller experiment which focuses on B-physics is LHCb [67]. The fourth main experiment is ALICE [68], which carries out research on quark-gluon plasma using heavy ion collisions.

3.2. The ATLAS Detector

For this thesis, data taken by the ATLAS experiment is analysed. Therefore, this section gives an overview on the coordinate system, the subcomponents of the detector and the trigger system. A more detailed description can be found in [65].

The Coordinate System

ATLAS uses a right-handed orthogonal coordinate system with its origin lying at the constructed interaction point. The x-axis points to the centre of the LHC and the y-axis points upwards. According to the right-handedness of the system, the direction of the z-axis is set and lies on the beam axis. Using this coordinate system, the transverse momentum of a particle can be defined as

$$p_T := \sqrt{p_x^2 + p_y^2}. \tag{3.1}$$

Since ATLAS has a cylindrical shape, the azimuthal angle ϕ and the polar angle θ are introduced, whereby ϕ is defined as the angle around the beam axis in the x-y-plane and θ as the angle between the beam axis and the outgoing particle.

Another useful variable at hadron colliders is the pseudo-rapidity defined as

$$\eta := -\ln\left(\tan\left(\frac{\theta}{2}\right)\right) = \frac{1}{2}\ln\left(\frac{|\vec{p}| + p_z}{|\vec{p}| - p_z}\right), \tag{3.2}$$

whereby $\vec{p}$ is the momentum of the particle and p_z the momentum along the z-axis. This variable has the advantages that it can be defined in terms of polar angle and the particle flow per unit pseudo-rapidity is approximately constant. Furthermore, at high energies, E, where $m \ll |\vec{p}|$ and, thus, $E \approx |\vec{p}|$, the pseudo-rapidity equals the rapidity

$$y = \frac{1}{2}\ln\left(\frac{E + p_z}{E - p_z}\right), \tag{3.3}$$

in which differences are Lorentz-invariant under boosts in the z-direction. Such an invariance is important at hadron colliders, where the fundamental interactions involve partons inside the proton, which only carry a fraction of the defined proton momentum. Therefore, collisions at the LHC are boosted relative to the centre-of-mass frame along the z-axis.

The last important variable is the distance in the η-ϕ-plane

$$\Delta R := \sqrt{\Delta\eta^2 + \Delta\phi^2}. \tag{3.4}$$

This is also invariant under boosts along the z-axis, since in the relativistic limit $\Delta\eta$ is invariant and $\Delta\phi$ has no z-dependence.

Subcomponents

The ATLAS experiment is the largest detector located at CERN with a length of 44 m and a height of 25 m. It weighs approximately 7000 tonnes and consists of several layers, each with a specific functionality. Starting from the inside, the first part is used to detect charged particles, followed by two separate calorimeters which are then surrounded by a muon spectrometer (see Fig. 3.1).

The inner detector is closest to the interaction point and is used for detecting charged particles by reconstructing the spatially resolved signals of the detector to tracks. According to the Lorentz force, charged particles travel perpendicular to magnetic fields. The particles' transverse momentum can be calculated from the curvature of its path and its charge. Therefore, a solenoid magnet which produces a magnetic field of $B = 2\,\mathrm{T}$ surrounds the inner detector. As the relative resolution decreases with increasing momentum (see Tab. 3.1), a high spatial resolution is required. Therefore, the inner detector is built from three smaller subcomponents. The silicon pixel detector is only a few centimetres

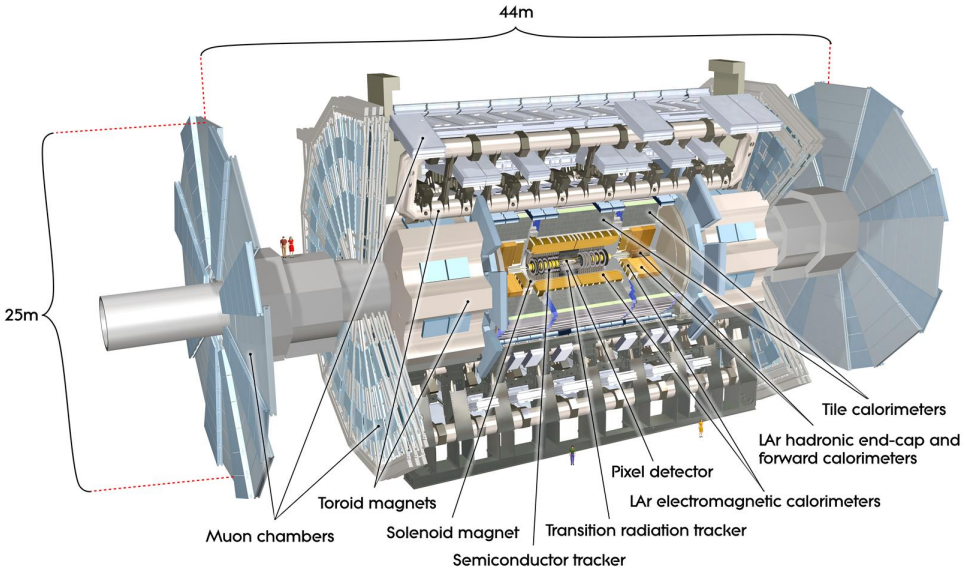

Figure 3.1.: Sketch of the ATLAS detector with its components labelled [65].

away from the collision point and has a pixel size of $50\,\mu\text{m} \times 400\,\mu\text{m}$, which allows measuring tracks directly after the interaction. After the pixel detector, the semiconductor tracker, SCT, is installed. Analogous to the pixel detector, it is made of silicon and detects the tracks of the particles but is formed in strips instead of pixels. Since the spatial separation of the tracks is larger at this point, the degraded resolution is not an issue. The outer most part of the inner detector is the transition radiation tracker, TRT. This is based on a mixture of transition radiation detector and a drift chamber. If a charged particle passes the TRT, it excites the gas, a mixture of xenon, carbon dioxide and molecular oxygen, inside the drift tubes. If the charged particle is an electron, it will emit transition radiation which will excite the xenon, providing particle identification capabilities.

The inner detector is surrounded by the electromagnetic calorimeter, ECAL, which measures the energy of electrons and photons by stopping them inside the material. This is realised by the particles showering, meaning they interact with the calorimeter material and deposit their energy by doing Bremsstrahlung and electron-positron pair production, respectively. These processes repeat on the resulting particles until the electrons and photons have such a low energy that they can be absorbed by the material easily. The ECAL is a sampling calorimeter composed of lead as the absorber and liquid argon as the active medium, where the energy is measured. The more energetic the shower, the more particles are created during the showering allowing more measurements. Thus, the resolution increases with increasing energy (see Tab. 3.1). In addition, the ECAL has a fine granularity and a special, accordion like geometry so that the response is uniform for

each particle direction.

Outside the ECAL, the hadronic calorimeter (HCAL) is placed, which also makes energy measurements. The hadrons, containing quarks and gluons, shower through interaction with the atomic nuclei. The HCAL is made of three parts with different materials. In the central region, it is composed of iron as the absorber and plastic scintillators as the active medium. The end-caps are made of copper (absorber) and liquid argon (active), in the forward region the absorber is tungsten. The resolution is worse than for the ECAL due to a larger granularity and a simpler geometry. However, it has larger shower depth and can cover a larger η range (see Tab. 3.1).

It is important to mention that although there is a distinction between ECAL and HCAL according to their setup, electrons and photons can also shower in the HCAL and hadrons in the ECAL. In general, showers from electrons and photons are shorter and narrower, so that they are covered primarily by the ECAL, whereby the showers of hadrons start later and are longer and wider.

The last part of ATLAS is the muon spectrometer. Since muons are not stopped within the calorimeters, an additional tracking detector for muons is implemented encompassing the rest of the ATLAS detector. The muons pass through a toroidal magnetic field, to measure the transverse momentum again in different types of drift chambers in the central region. Additionally, three large wheels are placed at the end-caps. Since these chambers are larger, the momentum resolution increases. A further improvement is given by the independent trigger system in the barrel region, which is an important part of the whole trigger system of the ATLAS experiment.

Detector	**Resolution**	**Coverage**
inner detector	$\sigma_{p_T}/p_T = 0.05\% \cdot p_T \oplus 1\%$	$\lvert\eta\rvert < 2.5$
ECAL	$\sigma_E/E = 10\%/\sqrt{E} \oplus 0.7\%$	$\lvert\eta\rvert < 3.2$
HCAL		
central region, end-caps	$\sigma_E/E = 50\%/\sqrt{E} \oplus 3\%$	$\lvert\eta\rvert < 3.2$
forward region	$\sigma_E/E = 100\%/\sqrt{E} \oplus 10\%$	$3.1 < \lvert\eta\rvert < 4.9$
muon spectrometer	$\sigma_{p_T}/p_T = 0.05\%$ at $p_T = 1\,\text{TeV}$	$\lvert\eta\rvert < 2.7$

Table 3.1.: Overview on the resolution and η coverage of the different detector parts with E and p_T in GeV [65].

Trigger System

With the bunch crossing spaced in 25 ns intervals, an event rate of 40 MHz needs to be processed. This corresponds to a data rate of approximately 600 Tb/s, which is unman-

ageable with the current techniques of data processing and storage. Therefore, ATLAS uses a two level trigger system to reduce the event rate and only stores a subset of events for later analysis [69].

The level-1 trigger, L1, is hardware based and uses the information provided by calorimeters and the muon spectrometer to search for events where large calorimeter deposits or a high p_T muon are present. The information on these events is collected and compared to predefined trigger items. The L1 trigger reduces the event rate to 100 kHz.

The second trigger is the software based high-level trigger (HLT). This trigger uses reconstruction and signature analysing algorithms to identify particles which allows to apply particle specific p_T thresholds. Different trigger selection criteria exist for the various analysis. This reduces the event rate by a factor of hundred to approximately 1 kHz, and events that pass the HLT are permanently stored for further analysis.

3.3. Monte Carlo Event Generators

The ATLAS experiment has two main aims: precision measurements and discoveries of phenomena beyond the SM. For both cases, it is important to know the signature the physical process leaves in the detector. It is equally important to understand the background. Since in data these processes are unavoidably mixed, a simulation of the dedicated process is needed to study their characteristics separately.

At hadron colliders, the event structure is more complex than at lepton colliders, where elementary particles with a defined energy collide. For hadron colliders, a multi-particle calculation in a multi-dimensional phase space is necessary. This can only be realized by Monte Carlo (MC) integration in Monte Carlo event generators.

In general, the simulation of a full event happens in several steps as indicated in Fig. 3.2. These will be explained briefly in this section. Further information can be found in [70, 71] and concerning ATLAS' procedure and software in [72].

The first step is to calculate the cross section for the process of interest. In general, this is a hard-scatter process, whereby the kinetic energy is converted into the production of new particles in an inelastic collision. Therefore, the matrix element, which is based on quantum field theory, can be calculated to a dedicated order of perturbation theory. In current MC event generators, this usually ranges from leading order (LO) to next-to-next-to leading order (NNLO). In quadrature, the matrix element can be interpreted as probability amplitude, from which the cross section can be calculated. Considering that the interacting partons only carry a fraction of the hadron's momentum, parton distribution functions, PDFs, which yield the probability for a certain parton momentum,

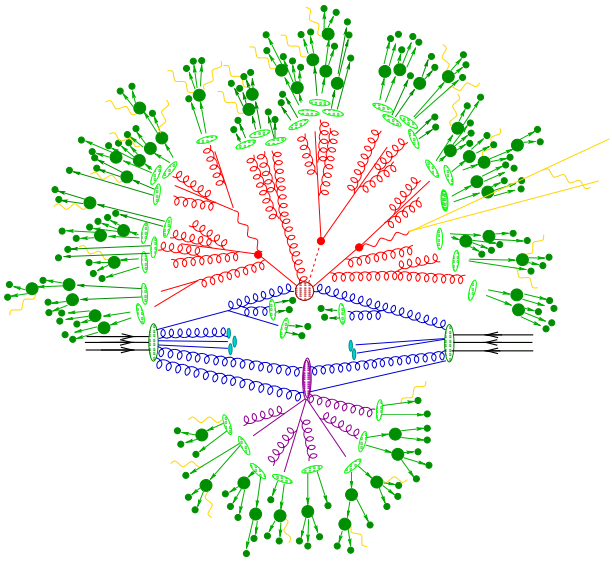

Figure 3.2.: Sketch of a hadron-hadron collision simulated by an MC event generator. The incoming hadrons are drawn in black, the corresponding interacting partons in blue. The red blob in the middle represents the hard scattered process. It is surrounded by components from simulated parton showers. The light green circles indicate a transition between partons and hadrons and the dark green circles hadron decays. Yellow lines represent electromagnetic interactions. The purple blob, is an underlying event [70].

must be included into this calculation.

In the next step, QCD corrections are applied to the hard scattering by parton showers. They include higher order initial and final state radiation. Since QCD allows self-coupling, a radiated gluon itself can radiate a gluon, which then can split into a pair of quarks. In addition, the parton shower locally conserves flavour as well as the four-momentum and does not violate unitarity. At the same time, electro-weak corrections are applied, although these have a much smaller effect.

As many particles are included in a proton bunch, it is unlikely that the process of interest is the only interaction occurring. Multiple proton-proton interactions are included as pile-up resulting in underlying events in the simulation.

Afterwards, all final partons from hard scattering and parton shower have to form colour neutral final states. This hadronisation can be realised by using one of the following two models. The string model is based on the linear dependence of the potential between quark and anti-quark on the distance. If the distance is large enough, a new pair of quarks is produced and two colour neutral final states are formed. These can again split into further pairs of quarks. Gluons are simply regarded as kinks in the connection between the quarks. The cluster model instead assumes that at each point the parton

shower can form colour singlet combinations of partons when gluons are regarded as a colour-anti-colour pair. These have a universal mass distribution independent from the considered energies. Therefore, one can link them to heavy mesonic resonances which then decay to better known hadrons.

The final step is to simulate the detector response, so that it can be analysed with the same tools as the actual data and hence is comparable to it. There are again two possibilities: full simulation by GEANT4 [73] and fast simulation by AFII [74]. While full simulation is highly time consuming in simulating the interaction of all particles with all detector components in complete detail, the default setup of AFII only has a complete simulation of the the inner detector and the muon spectrometer. The calorimeters are simulated by FastCaloSim [75]. Instead of simulating the interaction between the particles and the detector material, the energy profile of the parton showers is parametrised in the longitudinal and lateral direction. This is less accurate but significantly faster and requires less computing power. Thus, more samples of rare processes can be produced with sufficient statistics.

3.4. Jets in the Boosted Topology

As quarks and gluons hadronise or, in the case of top quarks, decay before they can be detected, only a shower of hadrons indicates their presence in the detector. These hadrons leave tracks in the inner detector, if they are charged, and an energy deposit in the calorimeter systems. All hadrons coming from one original parton are then ideally reconstructed as a single object called jet.

To reconstruct jets, different jet algorithms have been developed [76–80]. In general, sequential jet algorithms are used, of which most common ones are based on this formula

$$d_{ij} = \min\left(p_{T,i}^{k},\ p_{T,j}^{k}\right)\frac{\Delta R_{ij}^{2}}{R^{2}} \text{ with } k = \begin{cases} \text{-2} & \text{anti-}k_t \text{ (starting with hardest particles)} \\ 0 & \text{Cambridge/Aachen } (p_T \text{ independent}) \\ 2 & k_t \text{ (starting with softest particles)} \end{cases}$$

Here, k defines algorithm type and R is the size parameter. The transverse momentum of the constituent i and j, respectively, is denoted as $p_{T,i/j}$. The distance between i and j in detector coordinates is in this case defined as

$$\Delta R_{ij} = \sqrt{(y_i - y_j)^2 + (\phi_i - \phi_j)^2}.$$

The algorithm calculates d_{ij} and a cut-off value $d_{iB} = p_{T,i}^{k}$ for every pair of constituents

and then combines i and j to a proto-jet which is added to a modified list of constituents, if $d_{ij} < d_{iB}$. Otherwise i is labelled as a jet and is removed from the list of constituents. This procedure is repeated for the modified list of constituents. In ATLAS, the standard jet collection is created using the anti-k_t algorithm with $R = 0.4$, in the following referred to as small-R jets.

As the focus of the analysis is placed on searches for high resonant masses, the particles in the final state are close together in the detector. The average angular separation of two body decay with massless particles can be approximated by

$$\Delta R \approx \frac{2m}{p_T}, \tag{3.5}$$

whereby m and p_T denote the mass and transverse momentum of the mother particle. Assuming a heavy resonance of $m_H = 750\,\text{GeV}$ decaying into two light Higgs bosons, which decay to two W bosons of which at least one decays hadronically and has a transverse momentum of $p_T \approx \frac{1}{2}m_H$, one obtains an angular separation between two quarks of $\Delta R \approx 0.5$. Compared to a size parameter of $R = 0.4$, the jets cannot be resolved completely anymore. The solution to this is the usage of large-R jets, which have a larger size parameter and can contain all decay products.

The large-R jet collection is also an anti-k_t algorithm but with a size parameter of $R = 1.0$. However, the larger the jet, the more particles not belonging to the hard scattering are included in the jet (see Fig. 3.3 (a)). Therefore, a procedure called trimming is performed. First, the large-R jet constituents are reclustered with the k_t algorithm ($R = 0.2$) in smaller subjets, ensuring that particles from soft scattering processes are preferably combined (Fig. 3.3 (b)). The last step is to remove every subjet that has less than 5% of the transverse momentum of the large-R jet. In the end, a jet as sketched in Fig. 3.3 (c) remains.

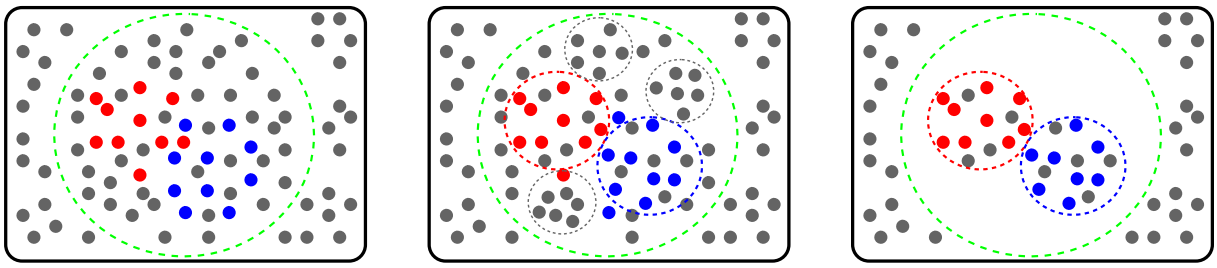

(a) ***(b)*** ***(c)***

Figure 3.3.: Illustration of the trimming procedure for a large-R jet.

One disadvantage of large-R jets is that in AFII simulation used to create signal MC

events (see Sec. 4.2) less calorimeter clusters are available which results in a poorly modelled calorimeter based mass. An alternative is the track assisted mass which mostly uses track information from the fully simulated inner detector

$$m^{TA} = \frac{p_T^{\text{calo}}}{p_T^{\text{track}}} \times m^{\text{track}}. \tag{3.6}$$

Here, the mass obtained from tracks, m^{track}, is reweighted by the p_T ratio between tracks and calorimeter to ensure that neutral hadrons are also covered in the mass.

The large-R jet also contains information about incident partons in form of substructure which can be used to assign a large-R jet to a certain decay. The first substructure variable is the N-subjettiness, τ_N [81], which is defined as

$$\begin{aligned} \tau_N(\beta) &= \frac{1}{d_0(\beta)} \sum_{i \in J} p_{T,i} \cdot \min\left(\Delta R_{1i}^{\beta}, \Delta R_{2i}^{\beta}, \ldots, \Delta R_{Ni}^{\beta}\right) \\ \text{with } d_0(\beta) &= \sum_{i \in J} p_{T,i} \cdot R^{\beta}. \end{aligned} \tag{3.7}$$

where the jet constituents i are clustered in N subjets. In the case of ΔR_{Ni}, the N denotes jet axis of the N^{th} subjet and R is again the size parameter. If the distances between all constituents and their nearest subjet axis is small, τ_N is small. If an original subjet is missing, the distances are significantly larger. Thus, the ratio $\frac{\tau_N}{\tau_{N-1}} \ll 1$ indicates that a large-R jet is best described by N subjets rather than $N-1$ subjets, indicating the presence of N initial partons.

Another set of substructure variables are energy correlation functions [82] defined as

$$ECF_0(\beta) = 1 \tag{3.8}$$

$$ECF_n(\beta) = \sum_{j_1 < \cdots < j_n \in J} \left(\prod_{i=1}^{n} p_{T,j_i}\right) \left(\prod_{i=1}^{n-1} \prod_{k=i+1}^{n} \Delta R_{j_i j_k}\right)^{\beta} \tag{3.9}$$

Previous studies have shown, that ratios between those functions were useful to find 2-prong jets for $n = 2$ [82–84]

$$C_n(\beta) = \frac{ECF_{n+1} \times ECF_{n-1}}{ECF_n^2} \tag{3.10}$$

$$D_n(\beta) = \frac{ECF_{n+1} \times ECF_{n-1} \times ECF_1^2}{ECF_n^3}. \tag{3.11}$$

4. Analysis

In this chapter, the topology of di-Higgs events considered in this thesis is described. Challenges resulting from this topology are discussed and the corresponding changes with regards to object selection are introduced. Finally, an optimisation of the signal and background separation is performed considering only statistical uncertainties.

4.1. Event Topology

In this analysis, a search for the production of di-Higgs events in the $hh \to \gamma\gamma WW^*$ decay channel is performed. In particular, the 1-lepton final state in the boosted topology as depicted in Fig. 4.1 for the resonant production is investigated, whereby only electrons and muons are considered as charged leptons. This has several advantages. Firstly, the background consists of mainly two contributions: the continuum di-photon background, which is the sum of all processes with at least two photons that do not originate from a resonance ending up in the final state, and the single-Higgs production with the Higgs boson decaying in two photons. Due to the excellent mass resolution of the di-photon system, it is possible to reduce the continuum background significantly by a cut on the SM Higgs mass window (see Sec. 4.5). The other advantage is the relatively high branching ratio of the $h \to WW^*$ decay and the presence of the charged lepton allows a better background suppression than the 0-lepton channel.

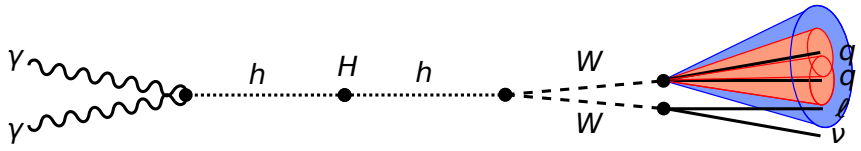

Figure 4.1.: Sketch of the decay channel in the centre-of-mass frame of the heavy Higgs.

As discussed in Sec. 2.3, the production can be either resonant or non-resonant. Since a resolved analysis in the $hh \to \gamma\gamma WW^*$ channel has been performed [85] and other channels such as $hh \to b\bar{b}\gamma\gamma$ [86] have a higher sensitivity to the non-resonant production and low resonant masses, the focus of this analysis lies on high resonant masses decaying

to boosted light Higgs-bosons. This results in the particles coming from the light Higgs boson decay being close together in the lab frame. While the effect on the photons is small due to the good granularity of the ECAL, the signature of the W-boson decays is affected by such a boosted topology as shown in Fig. 4.2.

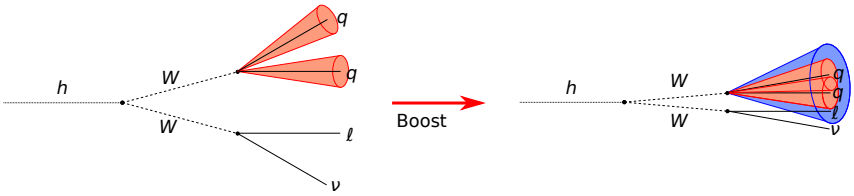

Figure 4.2.: Sketch of the effect of a boosted Higgs-boson decaying in two W-bosons resulting in the 1-lepton final state. Thereby, the resolved topology is given on the left-hand side and the boosted topology on the right-hand side. The red cones denotes small-R jets and the blue cone a large-R jet.

One point to note is the spatial separation of the small-R jets, which is significantly larger in the resolved topology on the left-hand side and in the same order than the jets' size parameter of $R = 0.4$ in the boosted topology on the right-hand side. The issue of merging jets can be resolved by the use of large-R jets, collecting all final particles of the hadronically decaying W-boson in one object. In the 1-lepton final state, the charged lepton can also be close to the small-R jets and, thus, end up inside the active area in the large-R jet. This also should be considered in the particle identification and the overlap removal (Sec. 4.4).

In summary, the final topology includes two photons, one large-R jet, one charged lepton (specifically a electron or a muon) and missing transverse energy due to the neutrino. Since the missing transverse momentum from a neutrino that is collinear to a large-R jet is not well understood, a cut on this quantity is not considered as a strict topological requirement (see Sec. 4.5).

4.2. Analysis Setup

Technical Setup

While in Run I every analysis group had to produce their own data sample in the form of `n-tuples`, Run II is more centrally organised with three types of data formats:

`xAOD` this is the standard data format for all outputs of simulations and actual collisions. Here, all information concerning reconstructed analysis objects is stored. It is the data format with the largest size.

DxAOD (derivation) this is a modification of the xAOD format, which is normally used to reduce the size of the files by removing unused variables, events and/or objects, respectively. It is also possible to add new objects or variables based on the information in the xAODs. All analysis groups usually have a set of specific derivations, which therefore do not have to be produced for every individual analysis.
This analysis uses a modified version of the HIGG1D1 derivation wherein large-R jets are included. This derivation applies a preliminary selection on the events based on reconstructed objects which can either be two photons, an electron and a photon, or a muon and a photon. Additionally, a di-photon trigger has to be passed.

n-tuples this is a file containing several variables in the form of tuples which are then used to produce histograms. By only storing necessary information, the size is reduced once again. Furthermore, the processing time is significantly shorter than for the other data formats since time intense variable calculations have been done before and can simply be accessed.

The analysis is performed with the analysis software ROOT [87] wherein several frameworks and tools are provided. To produce n-tuples from DxAODs, the ATLAS specific HGamAnalysisFramework, written in C++, is used. Within this framework, it is also possible to evaluate systematic variations (see Sec. 5.2). The n-tuples are then processed locally to apply the dedicated selection and to produce cutflows and histograms of kinematic distributions. For limit setting, HistFactory [88] is used.

Samples

Various MC samples for di-Higgs production corresponding to different resonant masses along with one non-resonant MC signal sample based on SM predictions are considered. The background estimate consists of a data-driven approach for the continuum di-photon background (see Sec. 4.6) and MC single-Higgs samples as predicted by the SM (see Sec. 2.3).

The signal samples are all generated using MADGRAPH5_aMC@NLO [89] with the CT10 tune [90] for the matrix element calculation and HERWIG++ [91] with the UEEE5 tune [92, 93] and the CTEQ6L1 PDF set [94] for the parton showering, the hadronisation and the underlying events. The detector simulation is performed as fast simulation using AFII. The signal samples are summarised in Tab. 4.1 (a) including the number of generated events.

The background samples differ in the generators used. The ggf and VBF samples are both produced using POWHEGBOX [95] with the CT10 tune for the calculation of the

matrix element and PYTHIA8 [96] with the AZNLO tune [97] and the CTEQ6L1 PDF set. The samples corresponding the Vh are generated using PYTHIA8 for both the matrix element calculation and the parton showering with the A14 tune [98] and the NNPDF23LO PDF set [99]. The $t\bar{t}h$ sample was produced using MADGRAPH5_aMC@NLO in the CT10 tune for the matrix element calculation and HERWIG++ with the UEEE5 tune and the CTEQ6L1 PDF set. In all single-Higgs background samples, the detector simulation was performed as full simulation by GEANT4. In Tab. 4.1 (b), all samples used for the different background processes are listed with the number of generated events in each sample.

Mass point m_H [GeV]	Generated events
non-resonant	970000
260	180000
300	199000
400	174000
500	179000
750	184000
1000	200000
1500	195000
2000	179000
2500	197000
3000	199000

(a) Signal samples.

Background	Generated events
ggf	1930000
VBF	984000
Wh	246200
Zh	247800
$t\bar{t}h$	976800

(b) Background samples.

Table 4.1.: List of all considered samples with their number of generated events. The complete sample names can be found in App. A.1.

Weights

Since an MC event generator cannot simulate every event with perfect accuracy, corrections are necessary to model the actual data as well as possible. Such corrections are realised by a weight

$$w = \underbrace{\frac{\sigma \times \mathcal{BR} \times \int \mathcal{L} dt \times w_{\text{mc}}}{N_{\text{ini}}}}_{\text{normalisation}} \times \underbrace{w_{\text{vt}} \times w_{\text{prw}}}_{\text{weights}} \times \underbrace{SF_\gamma \times SF_\ell \times SF_b}_{\text{object scale factors}} \tag{4.1}$$

which is applied to each event in the MC samples.

The number of generated events is arbitrary and often much higher than the number of events in data such that the MC statistics do not have a significant impact on the

analysis. Therefore, the first step is to normalise the number of generated events to the number of expected events by applying a factor $\sigma \times \mathcal{BR} \times \int \mathcal{L} dt \times w_{\text{mc}}/N_{\text{ini}}$, whereby, the cross section, σ, and the branching ratio, $\mathcal{BR}$, are generally predicted by theory for the dedicated process. The integrated luminosity, $\int \mathcal{L} dt$, gives the proper normalisation to the data set that is used for this analysis. Since $\sigma \times \mathcal{BR} \times \int \mathcal{L} dt$ gives the number of expected events in total, a further factor of N_{ini} corresponding to the reciprocal of the number of initial events in the MC samples at `xAOD` level, must be applied. An additional weight, w_{mc}, is also applied, which corresponds to an event weight determined by the MC event generator to take into account NLO loop corrections and interference and is considered in N_{ini}

$$N_{\text{ini}} = \sum_{\text{all events}} w_{\text{mc}}. \tag{4.2}$$

In this analysis, the luminosity is $\int \mathcal{L} \mathrm{d}t = 36.1\,\text{fb}^{-1}$ to match the data taken in 2015 and 2016 with the ATLAS experiment, which is determined by the procedure described in [100]. The cross sections for non-resonant di-Higgs production and single-Higgs production as well as the branching ratios are calculated based on SM predictions [56], while for the resonant di-Higgs production a cross section of $\sigma_{gg \to H \to hh} = 1\,\text{pb}$ is assumed, motivated by the upper limits set on di-Higgs production in Run I [101]. Thereby, the decay of the heavy Higgs boson in two light Higgs bosons is included. The values for the cross section, branching ratio and initial number of events are summarised in Tab. 4.2 for the different signal and single-Higgs backgrounds.

Other weights are the vertex weight, w_{vt}, which is a correction on the modelling of the z-position of the primary vertex, and a weight related to the pile-up generation, w_{prw}. Since pile-up is caused by collisions of other protons in the bunches, only an estimate is made since the calculation is time consuming and most samples are created before the run conditions are observed. The profile is then reweighted to the profile as it is measured data.

In addition, scale factors for specific particles are also part of the weight. There is a scale factor for photons, SF_γ, one for leptons, SF_ℓ and one corresponding to the b-tag efficiency, SF_b. All of these are used to correct the shape of the particle distributions to match the data.

	sample	σ [pb]	$\mathcal{BR}$	N_{ini}
signal mass point [GeV]	non-resonant	0.03341	2.9×10^{-4}	10727
	260	1.0	2.9×10^{-4}	3818
	300	1.0	2.9×10^{-4}	774
	400	1.0	2.9×10^{-4}	1942
	500	1.0	2.9×10^{-4}	5095
	750	1.0	2.9×10^{-4}	10739
	1000	1.0	2.9×10^{-4}	6414
	1500	1.0	2.9×10^{-4}	6693
	2000	1.0	2.9×10^{-4}	7289
	2500	1.0	2.9×10^{-4}	7836
	3000	1.0	2.9×10^{-4}	7492
background	ggf	44.08	2.3×10^{-3}	1930000
	VBF	3.78	2.3×10^{-3}	948000
	Wh	1.37	2.3×10^{-3}	246200
	Zh	0.88	2.3×10^{-3}	247800
	$t\bar{t}h$	0.51	2.3×10^{-3}	496082

Table 4.2.: Summary of the cross sections, branching ratios and weighted number of initial events for the signal and background MC samples. The cross sections correspond to the SM calculations [56] or, in the case of resonant signals to the order of limits set in Run I [101]. The branching ratio for the signal samples includes the $hh \to \gamma\gamma WW^*$ decay but for the background samples only the decay $h \to \gamma\gamma$ is considered.

4.3. Object Definitions

In this analysis, four different types of particles occur in the final state. Matching the signatures in the detector to the actual physical particles is based on different identification (ID) requirements the reconstructed objects must fulfil. Stricter requirements reduce the misidentification probability but can also reject an object which corresponds to the correct particle. Looser requirements enhance the acceptance but also reduce the purity of the sample. In addition, the objects must pass an isolation requirement such that particles originating from radiation are rejected. Therefore, the transverse energy within a certain distance ΔR around the considered object deducting the energy of the object itself and underlying events must be below a threshold.

Photons

Photons [102] can be reconstructed in two ways. Converted photons result in an e^+e^- pair before entering the ECAL. In this case, the electrons leave tracks in the inner detector

from which the conversion vertex can be reconstructed. Those tracks are then matched to the energy deposits in the calorimeter. Unconverted photons do not convert and instead shower inside the ECAL without matching tracks. The four-momentum can be reconstructed from the direction and the energy deposit in the ECAL.

In this analysis, both types of reconstructed photons are considered. In general, the two photons in the final state must fulfil the tight ID criteria and the "FixedCutLoose" isolation cut. The leading photon is required to have $p_{T,\gamma_1} \geq 35\,\text{GeV}$, the sub-leading one $p_{T,\gamma_2} \geq 25\,\text{GeV}$. The detection region is restricted to $|\eta| < 2.37$, whereby the transition region between central area and the end-caps of the calorimeter, $1.37 < |\eta| < 1.52$ known as the crack region, is rejected.

Electrons

The reconstruction of electrons [103] is identical to the method used for converted photons, where the tracks in the inner detector are matched to clusters of energy deposits in the ECAL, but no conversion vertex is found.

Electrons are required to fulfil the medium ID criteria and a "Loose" isolation cut. The p_T threshold is set to $p_{T,e} \geq 10\,\text{GeV}$, since the tracks provide additional information and increases the detection quality. Corresponding to the η coverage of the inner detector, electrons can be detected within $|\eta| < 2.47$ excluding the crack region.

Muons

Muons [104] are solely reconstructed by the tracks they leave in the inner detector and the muon spectrometer. The reconstruction is performed independently and the information is merged afterwards.

The muons are required to pass the medium ID criterion as well as the "GradientLoose" isolation cut. Corresponding to the η coverage of the muon spectrometer, they are restricted to $|\eta| < 2.7$. The p_T threshold is set to $p_{T,\mu} \geq 10\,\text{GeV}$. The crack region does not have to be removed, since the ECAL is not considered in the reconstruction.

Jets

In this analysis, large-R jets [105] are mainly considered. Here, the standard jet collection `AntiKt10LCTopoTrimmedPtFrac5SmallR20` as described in Sec. 3.4 is used. The large-R jets are based on locally calibrated topoclusters, whose calibration is independent of the object but used to adjust the calorimeter response, signal losses and energy loss due to

dead material. However, the energy and mass calibration of the jet is object dependent and in the case of large-R jets only valid for $p_{T,J} > 200\,\text{GeV}$ and $|\eta| < 2.0$.

Small-R jets [106] play a role in the overlap removal (see Sec. 4.4) and the veto on b-jets (see Sec. 4.5). These jets are based on topoclusters at the electromagnetic scale. They have a p_T threshold of $p_{T,j} > 25\,\text{GeV}$ and lie within $|\eta| < 4.4$, b-tagged jets are required to fulfil $|\eta| < 2.5$ since also tracking information is necessary.

4.4. Overlap Removal

Since this is the first analysis in the `HGamAnalysisFramework` taking the boosted topology and leptons into account, adjustments in the object selection were made. This mostly concerns the overlap removal (OLR) described in this section.

Nominal Overlap Removal

In ATLAS, objects are reconstructed independently of each other from detector responses (tracking information or energy deposits). Therefore, the OLR is designed to prevent a detector response to be assigned to more than one object by removing particles that are likely to contain energy from a different particle. The sequential steps of nominal OLR in the `HGamAnalysisFramework` are as follows:

1. Reconstructed photons are treated with the highest priority. First, all electrons which overlap with photons, satisfying $\Delta R_{\gamma e} < 0.4$, are removed.

2. Then, the small-R jets are compared to photons and are rejected if $\Delta R_{\gamma j} < 0.4$. This ensures that no photon is mislabelled as jet. Given that jets can also be faked by electrons, all jets within $\Delta R_{ej} < 0.2$ are removed.

3. It is also possible that electrons which result from the hadronisation are misidentified as primary decay products. Therefore, electrons which are within $\Delta R_{je} < 0.4$ of a small-R jet are removed.

4. Finally, muons are considered. Similar to the other objects, they are initially compared to the photons and are removed if $\Delta R_{\gamma\mu} < 0.4$. Then any muon which is $\Delta R_{j\mu} < 0.4$ of a small-R jet is also removed. This ensures that the muons are related to the hard scattered process and do not result from hadron decays.

Because this analysis uses the boosted topology and the reconstruction of hadrons as large-R jets, alternative OLR schemes are investigated.

Boosted leptons

The first adjustment on the nominal OLR only concerns the leptons in their OLR with small-R jets. As depicted in Fig. 4.2 in the beginning of this chapter, the boosted topology causes the final particles to leave signatures in the detector that are close together. Therefore, many leptons will be removed due to their small distance to small-R jets although they do not originate from a hadron decay.

The aim of this modification is to accept prompt leptons that are close to small-R jets while still removing those from the decays of hadrons. Since the latter leptons tend to have a lower transverse momentum than prompt ones, the ΔR threshold for leptons is made p_T dependent according to

$$\Delta R_{j\ell} = \min\left(0.4;\ 0.04 + \frac{10\,\text{GeV}}{p_{T,\ell}}\right). \tag{4.3}$$

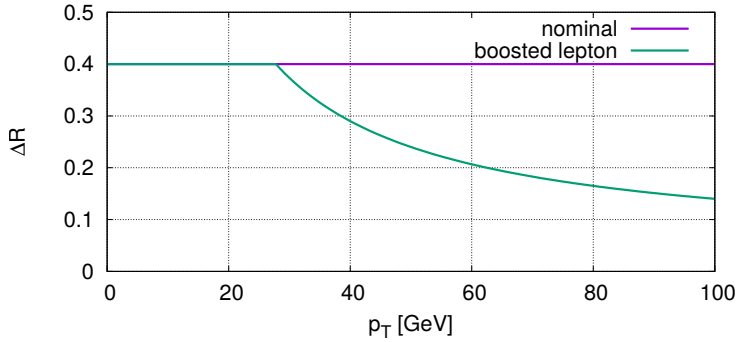

Figure 4.3.: Behaviour of the cut-off value $\Delta R_{j\ell}$ in dependency of the lepton $p_{T,\ell}$. The violet constant at $\Delta R = 0.4$ refers to the nominal OLR, the green curve to the boosted lepton OLR.

As shown in Fig. 4.3, the p_T dependent OLR alters the nominal OLR for leptons with $p_{T,\ell} \geq 27.8\,\text{GeV}$. Thus, some leptons that would have been incorrectly removed before are now kept.

The effect of this modification on the objects in the signal samples for mass points above $m_H = 500\,\text{GeV}$ is depicted in Fig. 4.4. The relative change in the number of leptons increases for increasing resonant masses (see Fig. 4.4 (a)). Generally, more muons (red) than electrons (black) are additionally kept since all jets within $\Delta R_{ej} < 0.2$ have been removed. In Fig. 4.4 (b), it can be seen that the relative gain in the 1-lepton final state (red) is significantly larger than the effect on the other final states (black and green).

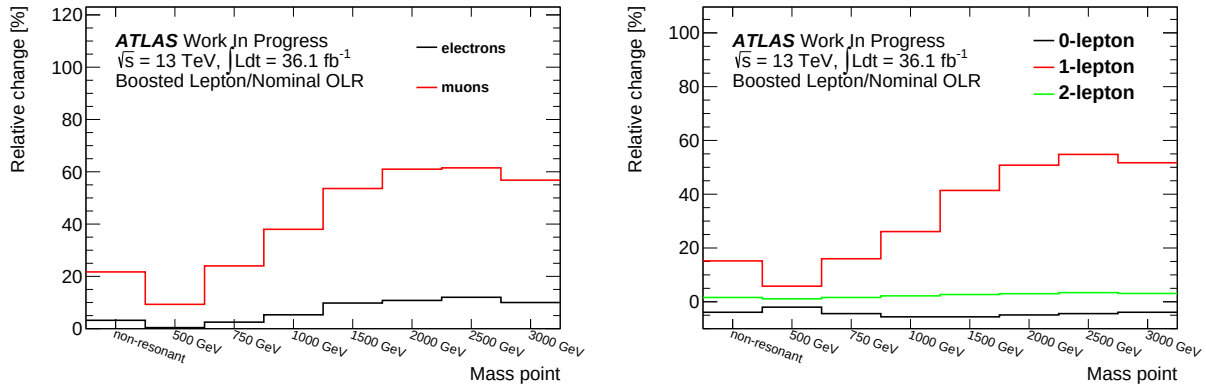

(a) ***(b)***

Figure 4.4.: Relative change in the number of (a) particles and (b) events passing the preselection (Sec. 4.5) by adjusting the nominal OLR to boosted leptons. The corresponding numbers can be found in App. A.2.

OLR between large-R jets and photons

Since large-R jets have not been used with the `HGamAnalysisFramework` before, they are not included in the nominal OLR. The distribution of the $\Delta R_{\gamma J}^{\text{min}}$ between the leading large-R jet and the nearest of the two leading photons with the nominal OLR applied is shown in Fig. 4.5 (a) for the $m_H = 750\,\text{GeV}$ sample. Due to the high mass of the resonance, it is produced approximately at rest in the lab frame. Therefore, the light Higgs bosons are produced back-to-back resulting in a large ΔR between the photons and the large-R jet or lepton, respectively. The peak at small ΔR values is the result of at least one photon being mislabelled as large-R jet.

This is supported by the difference between the calorimeter based mass, m^{calo} and the track assisted mass, m^{TA} depicted in Fig. 4.5 (b). The calorimeter based mass peaks at $m_J \approx 0\,\text{GeV}$, which equals the photon mass, and at $m_J \approx 140\,\text{GeV}$, which results from the di-photon system representing the Higgs mass with the calibration usually applied to hadrons. The track assisted mass only peaks at $m_J = 0\,\text{GeV}$ coming from both single photon and di-photon system, since photons do not leave tracks in the inner detector.

Analogous to the procedure between small-R jets and photons in the nominal OLR, a distance based OLR for large-R jets and the two leading photons is introduced. This should ensure that only photons from a Higgs decay cause the rejection of a large-R jet. The condition to remove a large-R jet is adjusted to the size parameter of $R = 1.0$ and is set to

$$\Delta R_{\gamma_{1,2}J} < 1.0. \tag{4.4}$$

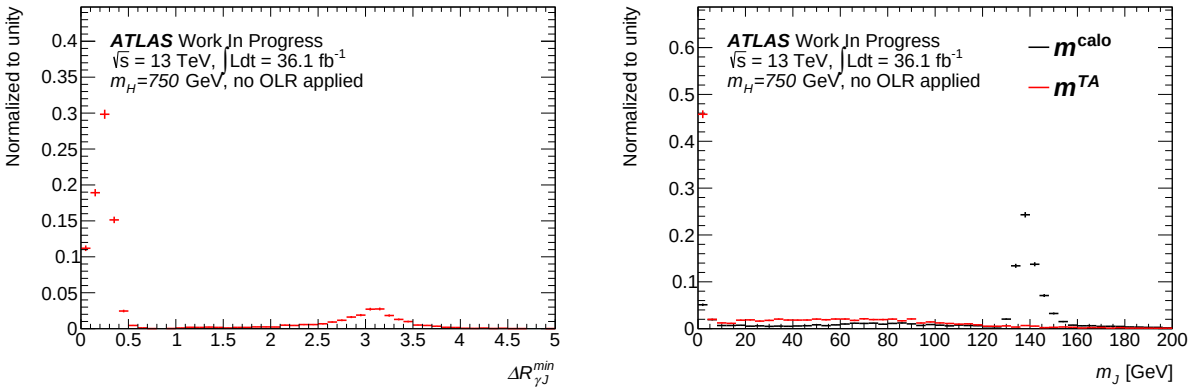

(a) *(b)*

Figure 4.5.: Distributions of (a) $\Delta R_{\gamma J}^{\min}$ between the leading large-R jet and the nearest of the two leading photons and (b) of m^{TA} and m^{calo} in comparison with the nominal OLR applied.

This corrects the distributions to the expected: in Fig. 4.6 (a) the peak of $\Delta R_{\gamma J}^{\min}$ distribution is shifted to higher values and also the mass distributions in Fig. 4.6 (b) become similar and now peak roughly at the W-boson mass at $m_J \approx 80\,\text{GeV}$ and the shoulder at lower values results from the off-shell W-boson.

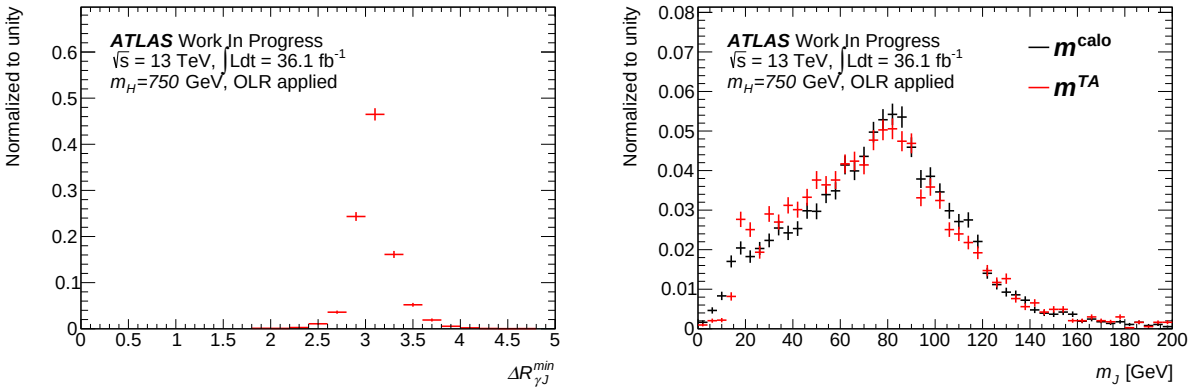

(a) *(b)*

Figure 4.6.: Distributions of (a) $\Delta R_{\gamma J}^{\min}$ between the leading large-R jet and the nearest of the two leading photons and (b) of m^{TA} and m^{calo} in comparison with the adjusted OLR applied.

OLR between large-R jets and electrons

The remaining modification on the OLR concerns the treatment of leptons and large-R jets. In the 1-lepton final state and the boosted topology, the probability that a lepton is

within the cone of a large-R jet is non-negligible. This signature is so unique that it was not studied before and a complete new procedure needs to be developed.

While electrons can also be misidentified as large-R jets due to their showering in the calorimeter, muons are not expected to deposit enough energy in the calorimeters to cause a large-R jet. Therefore, only an OLR between large-R jets and electrons needs to be developed. In contrast to the OLR with photons, no ΔR cut is possible because this would reject all events where the lepton is inside the large-R jet which is the case for nearly all signal events. Thus, other kinematic based cuts are investigated.

The strategy is to compare muons and electrons both inside and outside a large-R jet. If the kinematic distributions are similar for both types of leptons outside the large-R jet, the behaviour of muons inside the large-R jet can be used as a reference for those electrons which do not fake a large-R jet. To ensure the correct kinematics, the four vectors of the "lepton-jet system", $p^{\ell+J}$, are defined as following

$$\text{inside:} \quad \begin{matrix} p^{e+J} = p^J \\ p^{\mu+J} = p^\mu + p^J \end{matrix} \quad \text{and outside:} \quad \begin{matrix} p^{e+J} = p^e + p^J \\ p^{\mu+J} = p^\mu + p^J \end{matrix} , \tag{4.5}$$

whereby a lepton is considered to be inside the large-R jet, if $\Delta R_{\ell J} < 0.8$, and outside the large-R jet, if $\Delta R_{\ell J} > 1.2$. To avoid edge effects, the region $0.8 \leq \Delta R_{\ell J} \leq 1.2$ is excluded from this study since here, the lepton's energy may only partially contribute to the large-R jet's energy. For large-R jets, the track-assisted mass is used.

The investigated variables are the mass of the lepton-jet system, $m_{\ell+J}$, and the p_T ratio between the lepton and the lepton-jet system, $\frac{p_{T,\ell}}{p_{T,\ell+J}}$. Since the lepton-jet system includes nearly all final particles of the light Higgs-boson decay in two W-bosons, $m_{\ell+J}$ should be significantly larger than the electron mass which results from an electron misidentified as large-R jet. Due to the same origin of a W-boson from the same Higgs-boson decay, the lepton is expected to have roughly the same transverse momentum as the large-R jet at maximum, since it has to share the W-boson p_T with the neutrino. Therefore, $\frac{p_{T,\ell}}{p_{T,\ell+J}} \gg 0.5$ is a strong indication that the electron is mislabelled as large-R jet.

The corresponding distributions for the $m_H = 750\,\text{GeV}$ mass point are depicted in Fig. 4.7 for $m_{\ell+J}$ and Fig. 4.8 for $\frac{p_{T,\ell}}{p_{T,\ell+J}}$. The distributions for the non-resonant production mode and further mass points can be found in App. B.1. For leptons outside the jet, the distributions are nearly identical within statistical uncertainties (see Figures 4.7 (a) and 4.8 (a)). Therefore, muon-jet systems can be used as a reference for the behaviour of electron-jet systems in which the large-R jet is not caused by an electron.

Considering the distributions for the leptons inside the large-R jet, the differences are significant (see Figures 4.7 (b) and 4.8 (b)). The mass of the electron-jet system is shifted

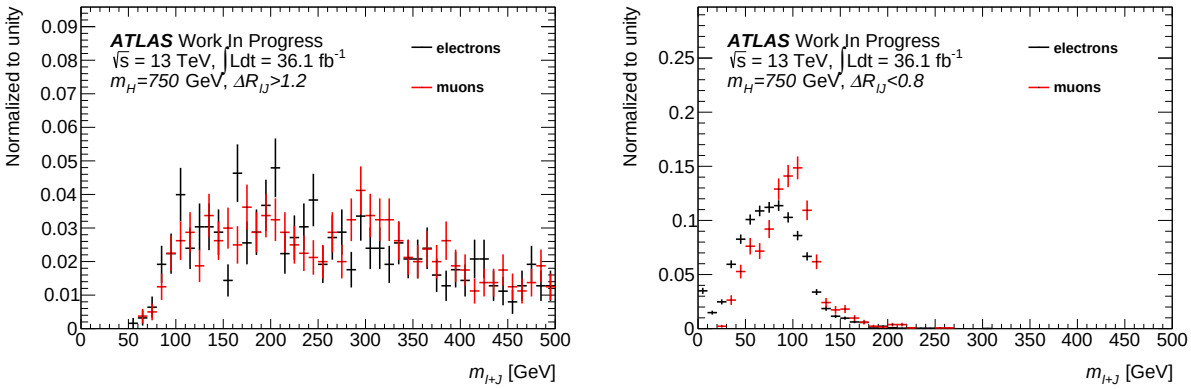

(a) *(b)*

Figure 4.7.: Mass of the lepton-jet-system whereby the lepton is (a) outside and (b) inside the large-R jet for $m_H = 750\,\text{GeV}$ mass point.

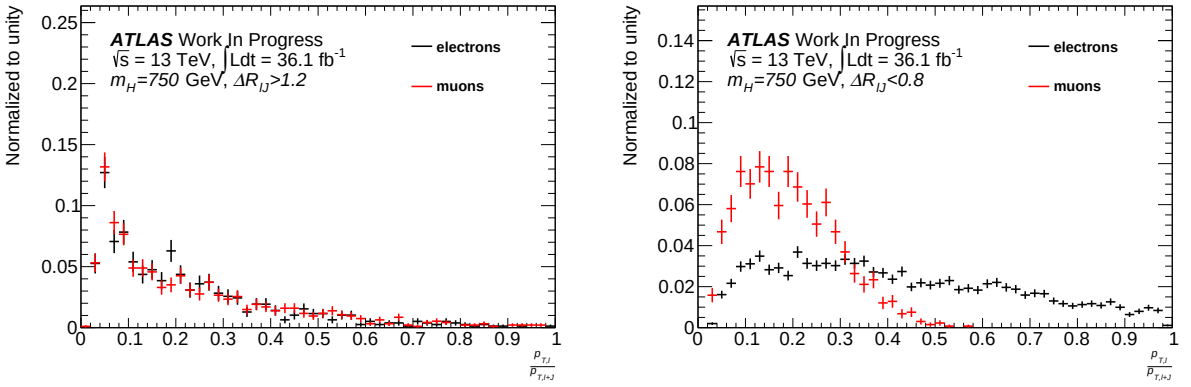

(a) *(b)*

Figure 4.8.: p_T ratio of the lepton and the lepton-jet-system whereby the lepton is (a) outside and (b) inside the large-R jet for $m_H = 750\,\text{GeV}$ mass point.

to slightly lower values and exhibits an additional peak at $m_{\ell+J} \approx 0$ corresponding to an electron seeding a large-R jet without any other energy deposit. Such large-R jets should be removed. The p_T ratio exhibits a completely different shape for the muon-jet and electron-jet systems. Here, the muons carry up to 60% of the p_T of the muon-jet system and the distribution exhibits a broad peak at around 20%. In contrast, an appreciable fraction of electrons may carry more than 90% of the p_T of the electron-jet system and with the p_T ratio distribution being rather flat, indicating that many of these large-R jets are dominated by electron energy deposits.

Based on the investigations presented above, it was decided to remove large-R jets with $m^{TA} < 15\,\text{GeV}$ and $\frac{p_{T,e}}{p_{T,e+J}} > 0.8$, if $\Delta R_{eJ} < 1.0$. The purpose of these cuts is to remove all large-R jets which are caused by an electron and a small amount of pile-up. As

shown in Fig. 4.9, the distributions in the electron channel still display differences to the reference distributions in the muon channel. Nevertheless, events dominated by purely energy deposits have been removed. Regarding higher mass points (see App. B.1), the distributions in the electron and muon channel start to converge.

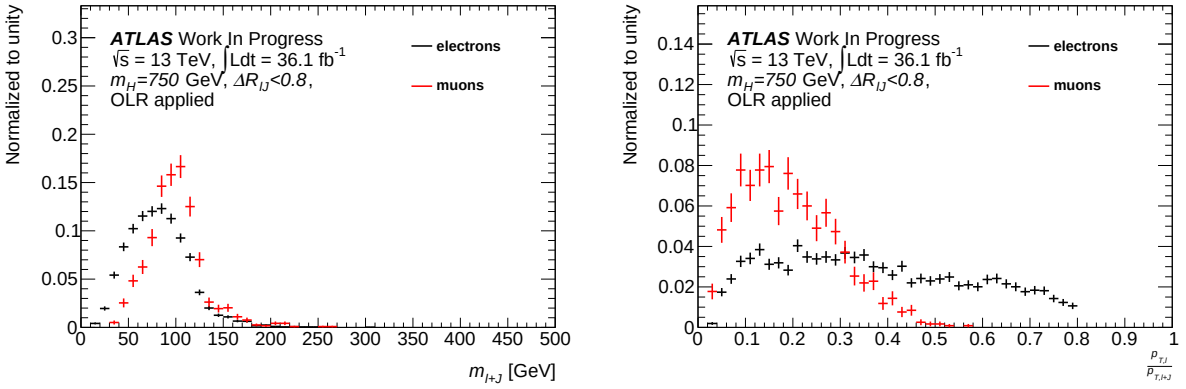

(a) *(b)*

Figure 4.9.: Distributions of (a) the mass of the lepton-jet system and (b) the p_T ratio between the lepton and lepton-jet system after the OLR is adjusted to remove large-R jets caused by electrons for $m_H = 750\,\text{GeV}$ mass point.

Nonetheless, in calculations the electron momentum must be subtracted from the large-R jet momentum, if $\Delta R_{eJ} < 1.0$ since they are still overlapping.

Summary

The completely modified OLR applied sequentially on all objects is as follows

1. Any electron within $\Delta R_{\gamma e} < 0.4$ of a photon is removed.
2. Any small-R jet within $\Delta R_{\gamma j} < 0.4$ of a photon is removed. Additionally, any small-R jet within $\Delta R_{ej} < 0.2$ is removed.
3. Any electron within $\Delta R_{je} < \min\left(0.4;\ 0.04 + \frac{10\,\text{GeV}}{p_{T,e}}\right)$ of a small-R jet is removed.
4. Any muon within $\Delta R_{\gamma\mu} < 0.4$ of a photon is removed and any muon within $\Delta R_{j\mu} < \min\left(0.4;\ 0.04 + \frac{10\,\text{GeV}}{p_{T,\mu}}\right)$ is also removed.
5. Any large-R jet within $\Delta R_{\gamma_{1,2}J} < 1.0$ is removed.
6. If an electron is within $\Delta R_{eJ} < 1.0$ of any large-R jet, this large-R jet satisfying $m^{TA} < 15\,\text{GeV}$ or $\frac{p_{T,e}}{p_{T,e+J}} > 0.8$ is removed.

4.5. Event Selection

In this section, event-level cuts are introduced to differentiate between signal and background based on the expected event topology of the signal. The entirety of these cuts will be referred to as preselection in the following. The derivation selection was applied beforehand and, therefore, is not added to this list but considered as starting point.

The first criterion is the data quality (DQ). This requirement ensures that no data events are used multiple times and that the data is collected during luminosity blocks with stable beam conditions and no major detector defects. This is realised by the Good Run List (GRL). Such luminosity blocks refer to a small period of data taking in which the conditions are constant. Then, the trigger criteria are applied. In this analysis, a di-photon trigger based on the HLT is used, where the leading photon is required to pass $p_{T,\gamma_1} \geq 35\,\text{GeV}$, the sub-leading one $p_{T,\gamma_2} \geq 25\,\text{GeV}$.

After this, at least two photons satisfying the loose ID criterion are required. These are referred to as loose photons. The two leading photons must match the trigger photons within $\Delta R = 0.07$.

Furthermore, the ID is set to tight and a loose isolation based on a fixed cut is required for the two leading photons. In the following, photons fulfilling these two criteria are referred to as tight photons.

To ensure that the photons are consistent with $h \to \gamma\gamma$ decays, relative p_T^γ cuts, i.e. $\frac{p_{T,\gamma_1}}{m_{\gamma\gamma}} > 0.35$ and $\frac{p_{T,\gamma_2}}{m_{\gamma\gamma}} > 0.25$ are applied. Furthermore, $m_{\gamma\gamma}$ is restricted to $94.49\,\text{GeV} < m_{\gamma\gamma} < 162.49\,\text{GeV}$ used as fit range for the continuum background estimate (see Sec. 4.6). For the signal and single-Higgs backgrounds, respectively, it is constrained to the signal region $|m_{\gamma\gamma} - m_h| < 2\sigma_{\gamma\gamma}$, whereby $m_h = 125.09\,\text{GeV}$ denotes the mass of the Higgs boson and $\sigma_{\gamma\gamma} = 1.7\,\text{GeV}$ the mass resolution of the di-photon spectrum. For the selection of data events, this mass window cut is inverted at first to blind the signal region.

To preserve orthogonality to the $hh \to \gamma\gamma b\bar{b}$ decay channel, a b-tag algorithm with an efficiency of 77% [107] is applied on small-R jets. Only events without any b-tagged small-R jet pass this step, with this condition referred to as a b-veto.

The final requirements in the preselection demand at least one large-R jet and exactly one charged lepton according to the signal topology discussed in Sec. 4.1.

The effect of this preselection on the different signal and background samples is listed in Tab. 4.3. Although ggf has the highest cross section of all single Higgs backgrounds, it is one of the minor backgrounds together with VBF, while $t\bar{t}h$ fits the topological requirements best and thus gives the highest yield of the single-Higgs backgrounds. Concerning the $m_{\gamma\gamma}$ sidebands, the low statistics are challenging for a stable continuum background estimate and are discussed in detail in the following section.

mass point [GeV]	Yield
non-resonant	0.0051
260	0.0020
300	0.0124
400	0.0338
500	0.1337
750	0.6200
1000	0.9066
1500	0.9238
2000	0.6205
2500	0.5367
3000	0.3324

(a)

background	Yield
ggf	0.0097
VBF	0.0023
Wh	0.0672
Zh	0.0234
$t\bar{t}h$	0.3666
$m_{\gamma\gamma}$ sidebands	16

(b)

Table 4.3.: Expected yields for the non-resonant production mode, the resonant mass points and the single-Higgs backgrounds after preselection assuming $\int \mathcal{L} \mathrm{d}t = 36.1\,\mathrm{fb}^{-1}$. For the resonant signals, $\sigma = 1\,\mathrm{pb}$ is set. The other processes use the SM cross sections. The $m_{\gamma\gamma}$ sidebands refer to the continuum background obtained from data. More detailed cutflows can be found in App. A.3.

Concerning the signal yields for different resonant masses, it is clear that after the preselection, the boosted topology is not sensitive to masses below $m_H = 500\,\mathrm{GeV}$. Therefore, those will neither be considered in the optimisation (Sec. 4.7) nor in the limit setting (Ch. 5). There is also a sensitivity decrease for masses above $m_H = 1500\,\mathrm{GeV}$. The reason is due to photon isolation requirements. In Fig. 4.10, the distance between the two leading photons, $\Delta R_{\gamma\gamma}$, is depicted for the different mass points. The distance decreases with an increasing resonant mass. For the $m_H = 1500\,\mathrm{GeV}$ mass point, some photons begin to overlap and thus fail the isolation requirement. For the $m_H = 3000\,\mathrm{GeV}$, most of the photon pairs are separated by $\Delta R_{\gamma\gamma} = 0.2$.

4.6. Continuum Background Estimation

The continuum background estimation follows a data driven approach since various processes can end up in a photons plus lepton plus jets final state although the number of events passing the large-R jet requirement is comparably small. Simulating all these processes would introduce systematic uncertainties on the modelling and the knowledge of the exact background composition. Since the signal region is clearly defined by the di-photon mass spectrum, it can be blinded easily such that no possible signal events influence the background estimate.

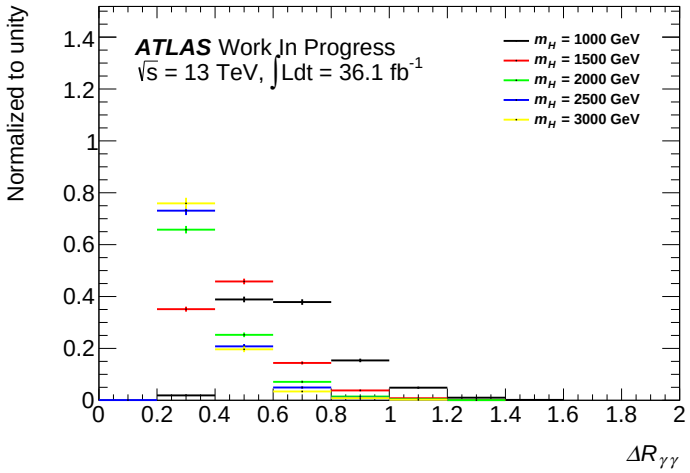

Figure 4.10.: Distance between the two leading photons for the different resonant masses.

This is done by fitting the data events in the sidebands defined by the fit range with an exponential of the form

$$f(x) = \exp(a + b \cdot x). \tag{4.6}$$

The expected number of continuum background events in the signal region is obtained by integrating the exponential in the signal region. As the signal signature is quite unique, only 16 events of the continuum background remain in the sidebands as depicted in the Tab. 4.3 (b).

To gain more statistics, a control region with a looser preselection can be introduced. The background estimate obtained in such a control region is then extrapolated to the previous signal region. For such an extrapolation to be valid, the kinematic distributions that are being considered should have the same shape in the signal and control regions. This ensures a correct extrapolation of the background estimate that is unbiased.

Regarding the detailed cutflow for the $m_{\gamma\gamma}$ sidebands in Tab. 4.4 (a), it is clear that the largest reduction results from the topological requirements of at least one large-R jet and exactly one charged lepton, which are crucial for the event selection. This is followed by the stricter, tight photon requirements. Removing these photon requirements results in 190 events in the sidebands of the continuum background (see Tab. 4.4 (b)).

Fig. 4.11 shows the $m_{\gamma\gamma}$ sidebands after preselection with the loose and tight photon criteria applied. A decrease in the statistical uncertainties can be clearly seen for the loose photon criteria. Comparing the exponentials fitted to the corresponding $m_{\gamma\gamma}$ distributions, it can be seen that they are very similar especially in the signal region.

Cuts	Events remaining
N_{DxAOD}	111112680
DQ	97814823
> 2 loose photons	29968480
trigger match	29887286
photon ID	4436503
photon isolation	1640858
rel. p_T^γ cuts	1431673
fit range	492673
sidebands	447374
b-veto	444164
≥ 1 large-R jet	2203
1 lepton	16

(a) Tight photons.

Cuts	Events remaining
N_{DxAOD}	111112680
DQ	97814823
> 2 loose photons	29968480
trigger match	29887286
photon ID	29887286
photon isolation	29887286
rel. p_T^γ cuts	23879083
fit range	8316379
sidebands	7593241
b-veto	7524681
≥ 1 large-R jet	47050
1 lepton	190

(b) Loose photons.

Table 4.4.: Cutflows of the sidebands for different photon criteria.

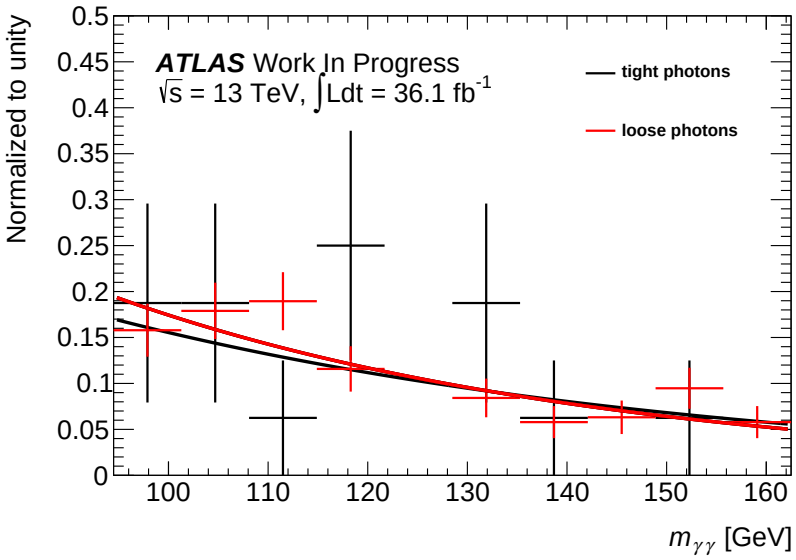

Figure 4.11.: Comparison of the $m_{\gamma\gamma}$ sideband distributions and the fitted exponentials from tight (black) and loose (red) photons. The error bars correspond to statistical uncertainties only.

Given that the control region uses loose photon criteria and the signal region uses tight photon criteria, with all other selection criteria being identical, an extrapolation of the background estimate can be realised by multiplying the estimated continuum background, N_{fit}, in the loose control region with the factor $N_{\text{SB}}^{\text{T}}/N_{\text{SB}}^{\text{L}}$, where N_{SB}^{T} represents the number of sideband events with the tight photon selection applied and N_{SB}^{L} is the number of sideband events with the loose photon selection applied. The final number of expected

continuum background events in the signal region is then given by

$$N_{\gamma\gamma} = N_{\text{fit}} \times \frac{N_{\text{SB}}^{\text{T}}}{N_{\text{SB}}^{\text{L}}}, \tag{4.7}$$

To estimate the statistical uncertainty of $N_{\gamma\gamma}$, the statistical uncertainties on all contributions are propagated as

$$\sigma_{N_{\gamma\gamma}} = \sqrt{\left(\frac{N_{\text{SB}}^{\text{T}}}{N_{\text{SB}}^{\text{L}}}\right)^2 \sigma_{N_{\text{fit}}}^2 + \left(\frac{N_{\text{fit}}}{N_{\text{SB}}^{\text{L}}}\right)^2 \sigma_{N_{\text{SB}}^{\text{T}}}^2 + \left(-\frac{N_{\text{fit}} \times N_{\text{SB}}^{\text{L}}}{\left(N_{\text{SB}}^{\text{L}}\right)^2}\right)^2 \sigma_{N_{\text{SB}}^{\text{L}}}^2}, \tag{4.8}$$

assuming that all variables are statistically independent. Here, $\sigma_{N_{\text{fit}}}$ also includes the uncertainties on the fit parameters a and b.

4.7. Optimisation

Although the preselection rejects many background events, further separation between signal and background is necessary by implementing cuts on kinematic variables. The optimal cuts are chosen by maximising the Asimov significance [108]

$$\Sigma = \sqrt{2 \times \left((s+b)\ln\left(1+\frac{s}{b}\right) - s\right)}, \tag{4.9}$$

which is more robust in the low statics limit than the commonly used definition

$$\Sigma_0 = \frac{s}{\sqrt{s+b}}\,.$$

In both cases, s denotes the expected signal yield and b the overall expected background yield with the currently investigated cut applied. Using error propagation, the uncertainty on the Asimov significance is given as

$$\sigma_\Sigma = \frac{1}{\Sigma} \times \sqrt{\left(\ln\left(1+\frac{s}{b}\right) \times \sigma_s\right)^2 + \left(\left(\ln\left(1+\frac{s}{b}\right) - \frac{s}{b}\right) \times \sigma_b\right)^2}, \tag{4.10}$$

$$\text{whereby } \sigma_b = \sqrt{\sigma_{N_{\gamma\gamma}}^2 + \sigma_{N_{\text{ggf}}}^2 + \sigma_{N_{\text{VBF}}}^2 + \sigma_{N_{Wh}}^2 + \sigma_{N_{Zh}}^2 + \sigma_{N_{t\bar{t}h}}^2}.$$

Each variable is scanned individually for the cut value yielding the highest significance corresponding to the optimal separation between signal and background. The expected yield of continuum background events is obtained in the loose control region and extrapolated to the signal region with tight photon criteria as discussed in Sec. 4.6. The scan

is aborted if $N_{\mathrm{SB}}^{\mathrm{L}} < 10$ to ensure a relatively stable fit. To be less dependent on the statistics of the sideband events corresponding to tight photons, the reweighting, $\frac{N_{\mathrm{SB}}^{\mathrm{T}}}{N_{\mathrm{SB}}^{\mathrm{L}}}$, is fixed before the optimisation and does not change during the variable scan for the best cut value. After the optimised cut is applied, the reweighting is modified according to the new selection and is fixed during the scan for cuts on further variables. Therefore, the obtained significances do not correspond to the final signal significances but nonetheless indicate which variable yields the highest separation power independently of statistical fluctuations.

Since the focus lies on heavy resonances and the resolved analysis only investigates resonant masses up to $m_H = 500\,\mathrm{GeV}$ [85], the $m_H = 750\,\mathrm{GeV}$ mass point is taken as reference signal in the optimisation. The optimised cuts are then applied to the other mass points as well. Therefore, the cuts are not optimised for the other mass hypotheses but the signal sensitivity is not effected since the considered variables are chosen in a way that the separation power increases or stays constant for increasing resonant masses. The optimised cuts will also be applied to the non-resonant signal sample since the boosted topology is already insensitive to this production mode and it is unlikely that a separate optimisation increase the significance significantly.

Possible Variables

In the following, the variables with the potentially highest separation power between signal and background are discussed briefly. The variables can be split in three categories: those using photon kinematics only, those using the kinematics of the W-boson decay products only, and those that use the kinematics of the entire event.

Regarding the photon kinematics of the event, two possible separation variables apart from the di-photon mass, $m_{\gamma\gamma}$, which is already used in the preselection, are expected to have a high separation power:

- the transverse momentum of the di-photon system, $p_{T,\gamma\gamma}$, has the advantages of the good ECAL resolution and a dependency on the investigated signal mass. The light Higgs bosons carry a large transverse momentum related to the resonant mass which is then transferred to the photons. Therefore, the p_T tends towards higher values for signal than for background events.

- the distance between the two photons, $\Delta R_{\gamma\gamma}$, profits from the high position resolution of the photons. Due to the boost of the light Higgs boson, this distance is smaller for signal than for background events.

Concerning the kinematics of the Higgs boson decay in two W-bosons, the large-R jet, the charged lepton and missing transverse energy from the undetected neutrino are considered. Therefore, various combinations from the corresponding kinematic variables are possible. The most promising ones are listed below:

- the missing transverse energy, E_T^{miss}, is considered to result in rather high values since it corresponds to approximately $\frac{1}{8}$ of the resonant mass if it results from the neutrino, ν. In reality, the missing transverse energy also results from detector mismeasurements, which affect the resolution of this variable.

- the transverse mass of the combined system of lepton, large-R jet and missing transverse energy, $m_{T,\ell\nu J}$, should yield the transverse Higgs mass, if the missing transverse energy matches the momentum of the neutrino.

- the mass of the lepton-jet system, $m_{\ell J}$, has the advantage that it will mainly result in values between the W-boson mass and the Higgs mass but without the need to consider missing transverse energy.

- the distance between the charged lepton and the large-R jet, $\Delta R_{\ell J}$, has the advantage that it is independent from energy scales of the calorimeter and, thus, has a better resolution than the mass variables discussed before. This variable depends on the resonant mass in the same manner as $\Delta R_{\gamma\gamma}$.

- the substructure variables C_2 and D_2 (see Sec. 3.4) have been found to separate large-R jets coming from W-boson decays from regular hadronic jet activity.

There are also variables which combine photon kinematics with W-boson related kinematics in the event. Again, several combinations are possible but only the most promising will be introduced below:

- the transverse mass of all considered objects, $m_{T,\text{all}}$, includes both photons, the lepton, the large-R jet and the missing transverse energy. This corresponds to the transverse mass of the resonance and, therefore, should be relatively high for signal events.

- the scalar sum of the transverse energy of all selected objects, H_T, will also result in large values for the signal events since all objects are expected to have a large transverse energy, which is not necessarily the case for the background processes.

- the distance between the lepton or large-R jet, respectively, and the closest photon, $\Delta R_{\gamma\ell}^{\text{min}}$ or $\Delta R_{\gamma J}^{\text{min}}$, uses the fact that the two Higgs-bosons are produced back-to-back

and, therefore, the distance is large compared to the distances in the background signatures.

A plot showing the separation power between the $m_H = 750\,\text{GeV}$ mass point and the leading backgrounds can be found in App. B.2 for each variable. The distributions of the variables yielding the best cut value are discussed in detail in conjunction with the significance distribution later in this section.

Consistency checks

As discussed in Sec. 4.6, a loose control region is used to estimate the continuum background. Therefore, the shape of variables described before needs to be checked for consistency between the loose and tight selections such that a correct extrapolation of the continuum background estimate is ensured.

In Fig. 4.12, the distributions, normalised to unity, for the $m_{\gamma\gamma}$ sidebands with loose and tight photon criteria are compared in the variables $p_{T,\gamma\gamma}$ and $\Delta R_{\ell J}$. While the comparison is limited by the statistics of the $m_{\gamma\gamma}$ sidebands with the tight photon criteria applied, there is no statistically significant deviation between the compared distributions.

The other variables also pass this consistency check and the corresponding plots can be found in App. B.3.

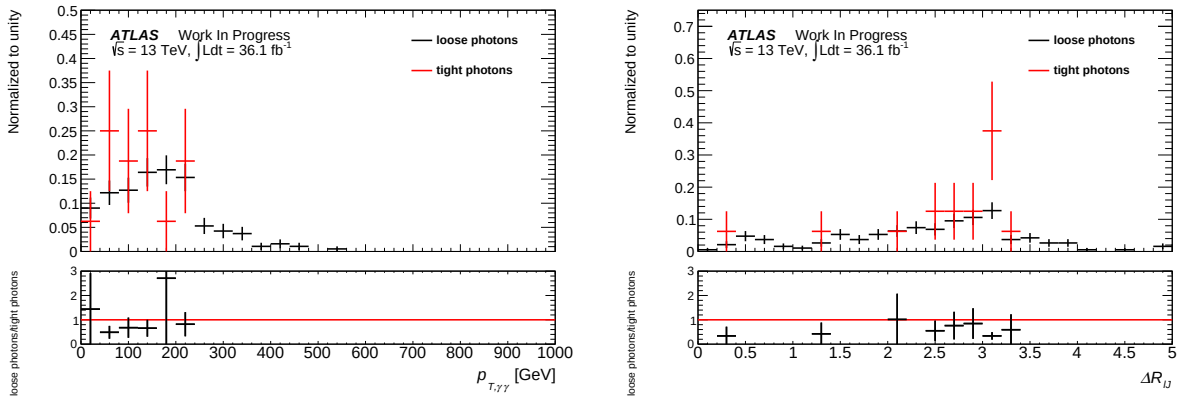

Figure 4.12.: Consistency checks between the loose and tight photon criteria for (a) the transverse momentum of the di-photon system and (b) the distance between the lepton and the large-R jet.

In addition, the sidebands are used to estimate the number of background events in the signal region. Therefore, correlations between the di-photon mass and the considered variable would bias the background estimate. If the distributions of the upper and lower sidebands are consistent, then such a bias is deemed to be small.

In Fig. 4.13, the distributions of $p_{T,\gamma\gamma}$ and $\Delta R_{\ell J}$ are separately shown for upper and lower $m_{\gamma\gamma}$ sidebands with loose photon criteria. In the case of $\Delta R_{\ell J}$, some deviations between upper and lower sideband are visible. Nonetheless, no large shifts or significant shape differences are observed. Therefore, the shapes of these variables are deemed to be uncorrelated with $m_{\gamma\gamma}$, and thus the biases resulting from the background using sideband events in the control region can be ignored.

The other variables also pass this consistency check and the corresponding plots can be found in App. B.4.

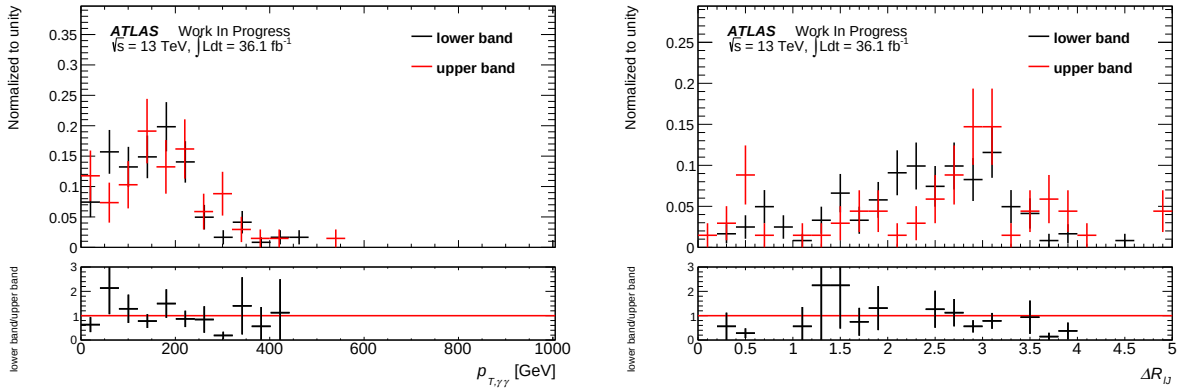

(a) *(b)*

Figure 4.13.: Consistency checks between the upper and lower $m_{\gamma\gamma}$ sidebands for (a) the transverse momentum of the di-photon system and (b) the distance between the lepton and the large-R jet. Here, only the loose photon criteria are applied.

Systematic uncertainties from these assumptions are discussed in Sec. 5.2.

Optimisation

In this analysis, the optimisation is performed in three steps. In the first step, only the preselection is applied and all variables are scanned for a cut yielding the highest significance across all variables. This cut is then applied and the optimisation procedure is repeated to obtain the best cut on a second variable. As a final step, the cut on the first variable is re-optimised since the two variables can be correlated and looser cut on the first variable could yield a higher final significance.

In Tab. 4.5, the variables with the corresponding cut yielding the highest significance for the $m_H = 750\,\text{GeV}$ mass point are listed. The initial sidebands are fixed to $N_{\text{SB}}^{\text{T}} = 16$ and $N_{\text{SB}}^{\text{L}} = 190$ as obtained in Sec. 4.6 after the preselection.

In Fig. 4.14 (a), the evolution of the significance depending on the cut value is shown for $p_{T,\gamma\gamma}$ which is the variable yielding the best separation between signal and background.

Cut	Significance	N_{sig}	$N_{\gamma\gamma}$	$N_{\text{single-}h}$
$p_{T,\gamma\gamma} > 240\,\text{GeV}$	0.75 ± 0.05	0.562 ± 0.010	0.24 ± 0.08	0.161 ± 0.007
$\Delta R_{\ell J} < 1.2$	0.74 ± 0.05	0.498 ± 0.010	0.21 ± 0.07	0.109 ± 0.006
$\Delta R_{\gamma\gamma} < 1.0$	0.71 ± 0.05	0.472 ± 0.010	0.18 ± 0.07	0.130 ± 0.007
$m_{T,\ell\nu J} < 140\,\text{GeV}$	0.67 ± 0.06	0.414 ± 0.009	0.20 ± 0.07	0.067 ± 0.005
$m_{\ell J} < 130\,\text{GeV}$	0.60 ± 0.05	0.470 ± 0.010	0.37 ± 0.12	0.106 ± 0.007

Table 4.5.: Overview on the leading five variables yielding the highest significance in the first optimisation step.

The significance rises smoothly until the cut $p_{T,\gamma\gamma} > 240\,\text{GeV}$ is reached resulting in $\Sigma = 0.75$ before the significance decreases again. Afterwards, the significance decreases again. Regarding the signal and main background distributions in Fig. 4.14 (b), the optimal cut value $p_{T,\gamma\gamma} > 240\,\text{GeV}$ (dashed pink line) shows the point where the additional signal rejection is still smaller than the additional background rejection which is not the case for a harder cut. The distributions corresponding to the other variables given in Tab. 4.5 are shown in App. B.5.

To allow an optimisation of a second variable and retain signal acceptance, a slightly looser cut of

$$p_{T,\gamma\gamma} > 200\,\text{GeV} \tag{4.11}$$

is applied since this is the point where the signal starts increasing (solid pink line in Fig. 4.14 (b)). At this point, a large number of expected background events is rejected while nearly all expected signal events are kept.

Applying this slightly loosened cut on $p_{T,\gamma\gamma}$, only $N_{\text{SB}}^{\text{T}} = 3$ events and $N_{\text{SB}}^{\text{L}} = 62$ events remain in the $m_{\gamma\gamma}$ sidebands. With such statistics, an optimisation of a second cut that could further increase the signal significance is possible.

In Tab. 4.6, the four variables yielding in the highest significance are summarised. The cut on $m_{\ell J} < 140\,\text{GeV}$ yields the highest significance of $\Sigma = 0.96$ directly followed by the cut on $\Delta R_{\ell J} < 1.6$ yielding $\Sigma = 0.96$. While the significance of a cut on $m_{\ell J}$ yields a clear maximum in Fig. 4.15 (a) resulting from the increasing signal peak over the mostly constant background (Fig. 4.15 (b)), the significance of a cut on $\Delta R_{\ell J}$ (Fig. 4.16 (a)) is purely limited by the background statistics ($N_{\text{SB}}^{\text{L}} < 10$) as nearly no signal is cut away (Fig. 4.16 (b)). Given the low expected signal yield, $\Delta R_{\ell J} < 1.6$ is preferred over $m_{\ell J} < 140\,\text{GeV}$ to result with a higher signal acceptance. The distributions corresponding to the other variables given in Tab. 4.6 are also shown in App. B.5.

After the $\Delta R_{\ell J} < 1.6$ cut is applied, no events in the tight photons sidebands remain.

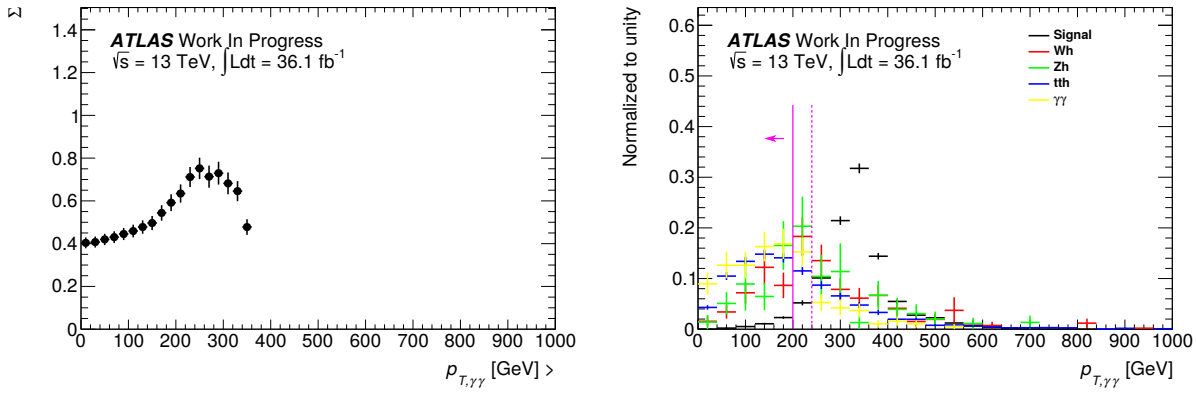

(a) *(b)*

Figure 4.14.: Distributions of (a) the significance and of (b) the $m_H = 750\,\text{GeV}$ mass point and the main background compositions for $p_{T,\gamma\gamma}$ as the variable yielding the best separation between signal and background in the first optimisation step. Thereby, the dashed pink line gives the best cut value, the solid pink line the actual applied cut value with the arrow indicating which part would be cut away.

Cut	Significance	N_{sig}	$N_{\gamma\gamma}$	$N_{\text{single-}h}$
$m_{\ell J} < 140\,\text{GeV}$	0.96 ± 0.10	0.474 ± 0.010	0.07 ± 0.05	0.062 ± 0.005
$\Delta R_{\ell J} < 1.6$	0.96 ± 0.09	0.510 ± 0.010	0.07 ± 0.05	0.087 ± 0.005
$m_{T,\ell\nu J} < 180\,\text{GeV}$	0.95 ± 0.10	0.470 ± 0.010	0.07 ± 0.05	0.062 ± 0.005
$\Delta R_{\gamma\ell} > 2.4$	0.87 ± 0.10	0.558 ± 0.011	0.14 ± 0.09	0.122 ± 0.007

Table 4.6.: Overview on the leading five variables yielding the highest significance in the second optimisation step.

Therefore, it is set to $N_{\text{SB}}^{\text{T}} = 1$ for further optimisation, to obtain an expected number of continuum background events which is thus slightly overestimated. In the loose photons sidebands 15 events remain. The last step, is to re-optimise $p_{T,\gamma\gamma}$ to ensure that any looser cut does not yield a higher maximum significance due to unconsidered correlations. The re-optimisation yields the same cut value of $p_{T,\gamma\gamma} > 200\,\text{GeV}$ with a final significance of

$$\Sigma = 0.92 \pm 0.17 \text{ whereby} \tag{4.12}$$
$$N_{\text{sig}} = 0.51 \pm 0.01,\ N_{\gamma\gamma} = 0.09 \pm 0.10 \text{ and } N_{\text{single-}h} = 0.087 \pm 0.005.$$

In Tab. 4.7, the number of expected signal and background yields after the preselection, the two optimised cut values is summarised. The signal is here represented by the non-resonant production mode and the $m_H = 750\,\text{GeV}$ mass point used for optimisation.

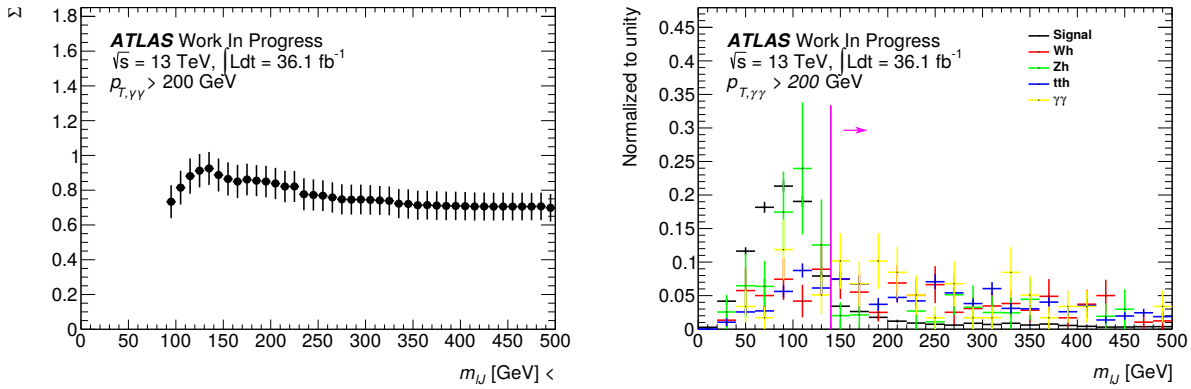

(a) *(b)*

Figure 4.15.: Distributions of (a) the significance and of (b) the $m_H = 750\,\text{GeV}$ mass point and the main background compositions for $m_{\ell J}$ as the variable yielding the best separation between signal and background in the second optimisation step. Thereby, the solid pink line gives the best cut value with the arrow indicating which part would be cut away.

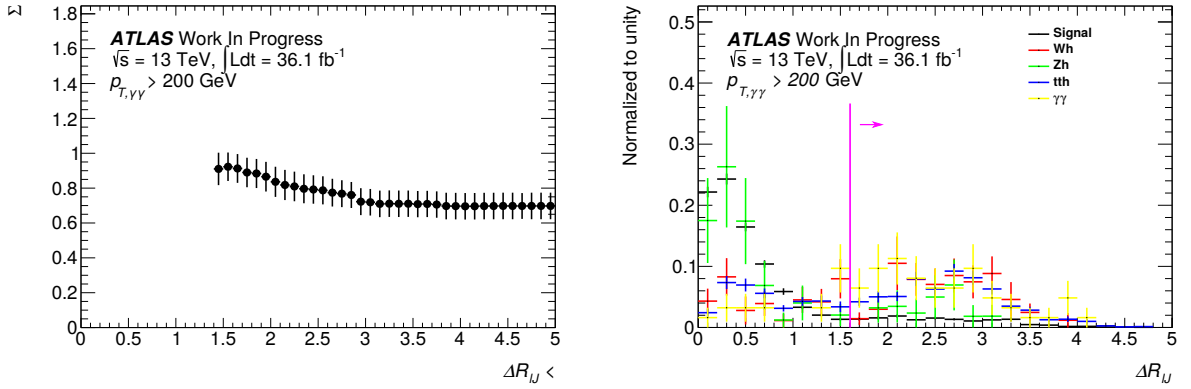

(a) *(b)*

Figure 4.16.: Distributions of (a) the significance and of (b) the $m_H = 750\,\text{GeV}$ mass point and the main background compositions for $\Delta R_{\ell J}$ as the variable yielding the second best separation between signal and background in the second optimisation step. Thereby, the solid pink line gives the best cut value with the arrow indicating which part would be cut away.

Fitting the Continuum Background

With the small event statistics, it is also necessary to check the quality of the fit of the $m_{\gamma\gamma}$ spectrum. The parameters a and b at different optimisation steps are listed in Tab. 4.8. The uncertainty on the fit parameters rises for decreasing statistics in the sidebands.

Cut	$N_{\text{non-res.}}$	$N_{750\,\text{GeV}}$	$N_{\gamma\gamma}$	$N_{\text{single-}h}$	$\Sigma_{750\,\text{GeV}}$
Preselection	0.005	0.620	1.69	0.469	0.40
$p_{T,\gamma\gamma} > 200\,\text{GeV}$	0.004	0.595	0.27	0.222	0.73
$\Delta R_{\ell J} < 1.6$	0.003	0.510	0.09	0.087	0.89

Table 4.7.: Expected yields for the non-resonant production, the $m_H = 750\,\text{GeV}$ mass point, the continuum background and the single-Higgs backgrounds at sequential applied cuts and the signal significance for the $m_H = 750\,\text{GeV}$ mass point. A more detailed cutflow including the other mass points as well can be found in App. A.3.

The χ^2 can be used as a measure of the fit quality [109]. It is defined as

$$\chi^2 = \sum_{\text{bins}} \frac{(O_i - E - i)^2}{E_i} \tag{4.13}$$

whereby O_i denotes the number of observed events in bin i and E_i the number of expected events predicted by the fit. The reduced χ^2 is then the χ^2 divided by the number of degrees of freedom, Ndf. If a fit is appropriate, the reduced χ^2 has an expectation value of one. As shown in Tab. 4.8, this only holds for the preselection and the quality decreases with harder cuts but this is expected.

Cut	N_{SB}^{L}	a	b	χ^2/Ndf
Preselection	190	5.5 ± 0.5	-0.020 ± 0.004	1.148
$p_{T,\gamma\gamma} > 200\,\text{GeV}$	62	2.9 ± 1.0	-0.010 ± 0.008	1.675
$\Delta R_{\ell J} < 1.6$	15	0.0 ± 1.7	0.003 ± 0.013	0.308
($b \leq 0$ required)		0.4 ± 0.3	0.00 ± 0.03	0.316

Table 4.8.: Evolution of the fit parameters and the reduced χ^2 depending on the applied selection and left statistics. In the last row, the exponential is restricted by $b \leq 0$.

It is important to note that after the $\Delta R_{\ell J}$ cut, the fit returns a rising instead of a falling exponential (see Fig. 4.17 (a)). This is most likely due to statistical fluctuations and a small correlation between $m_{\gamma\gamma}$ and $p_{T,\gamma\gamma}$ which was not visible in the consistency checks. Since the $m_{\gamma\gamma}$ spectrum is expected to be falling, the fit parameter b is restricted to $b \leq 0$. This results in values, given in the last row of Tab. 4.8. The fit then returns a constant, which is shown in Fig. 4.17 (b), and returns a slightly better reduced χ^2 than the unrestricted exponential.

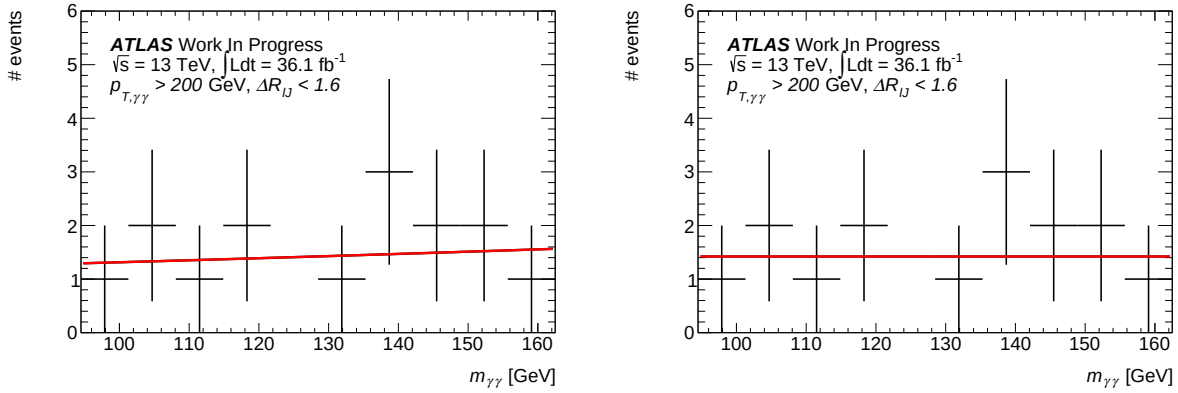

Figure 4.17.: Mass spectrum of the di-photon system with all optimised cuts applied (a) without and (b) with restricting the fit parameter $b \leq 0$.

5. Statistical Interpretation

In this chapter, exclusion limits are set on $\sigma_{gg\to H} \times \mathcal{BR}_{H\to hh}$ for resonant masses between $m_H = 500\,\text{GeV}$ and $m_H = 3000\,\text{GeV}$ and on $\sigma_{gg\to hh}$ for the non-resonant production mode. The statistical power of the 1-lepton final state is combined with that of the 0-lepton final state. Initially, only statistical uncertainties are considered for these limits. The systematic uncertainties will be discussed afterwards and then included in the limit setting. The observed limits are obtained from the unblinded signal region after the optimised selection criteria.

5.1. Limits with Statistical Uncertainties Only

In Tab. 5.1, the yields for the different signal and background samples after optimisation are summarised for both the 1-lepton and 0-lepton final states. The optimisation in the 0-lepton final state is described in detail in [110].

In the 1-lepton final state, zero data events are observed in the signal region which is consistent with the expected background estimate of 0.18 ± 0.10 events. In contrast, with seven observed data events in the signal region a small excess over the expected background estimate of 3.4 ± 0.5 events is observed in the 0-lepton final state, which is nonetheless consistent within three standard deviations that are needed to identify the excess as an evidence of new physics.

In both final states, the mass point of $m_H = 1500\,\text{GeV}$ gives the highest expected yield, followed by $m_H = 1000\,\text{GeV}$. The analysis has very little sensitivity to non-resonant di-Higgs production and to resonant masses below $m_H = 500\,\text{GeV}$ resulting in small expected yields for such signals.

Regarding the background composition in the 1-lepton final state, the continuum background estimate is approximately the number of expected single-Higgs background events, whereby $t\bar{t}h$ is the dominant process. For the 0-lepton final state, the continuum background is slightly larger than the single-Higgs background, which is dominated by ggf.

However, both channels have their own advantages. While the 1-lepton final state has a higher signal over background ratio, the 0-lepton state profits from the larger signal

acceptance and is therefore less limited by statistical uncertainties.

	sample	Yield 1 lepton	Yield 0 lepton
signal mass point [GeV]	non-resonant	0.0029 ± 0.0001	0.0068 ± 0.0001
	500	0.045 ± 0.003	0.021 ± 0.002
	750	0.51 ± 0.01	1.67 ± 0.02
	1000	0.79 ± 0.01	2.47 ± 0.02
	1500	0.79 ± 0.01	2.60 ± 0.02
	2000	0.62 ± 0.01	1.75 ± 0.02
	2500	0.424 ± 0.008	0.97 ± 0.01
	3000	0.243 ± 0.006	0.58 ± 0.01
background	continuum background	0.09 ± 0.10	1.8 ± 0.5
	ggf	0.0005 ± 0.0005	0.75 ± 0.05
	VBF	0.0004 ± 0.0003	0.086 ± 0.006
	Wh	0.016 ± 0.003	0.140 ± 0.009
	Zh	0.011 ± 0.002	0.102 ± 0.007
	$t\bar{t}h$	0.059 ± 0.004	0.126 ± 0.006
	Σ_{bkg}	0.18 ± 0.10	3.4 ± 0.5
	observed	0	7

Table 5.1.: Summary of the expected yields for the different signal mass points and the backgrounds in both the 1-lepton and 0-lepton final states, using $\int \mathcal{L} dt = 36.1\,\text{fb}^{-1}$ and cross sections according to SM predictions for single-Higgs production and non-resonant di-Higgs production. For resonant di-Higgs production, $\sigma = 1\,\text{p}$ is assumed. Σ_{bkg} denotes the sum of all backgrounds. The last row gives the number of observed events in the signal region in the complete 2015 and 2016 data set. Detailed cutflows can be found in App. A.3.

Given the observed events in the signal region, no evidence for resonant nor non-resonant production of di-Higgs events is found. Therefore, upper CL_s limits [111] on the cross section are set.

The CL_s upper limit setting was developed at Lep to avoid spurious exclusions for low statistic samples. In this method, two tests are performed simultaneously. If X is a random sample from a probability distribution with a real, non-negative parameter, θ, and $1-\alpha'$ is the dedicated confidence interval, the hypothesis $H_0 : \theta = \theta_0$ is tested against the alternative hypothesis $H_1 : \theta = 0$ (background-only) using

$$\frac{\mathcal{P}\left(\theta_{\text{up}}(X) < \theta | \theta_0\right)}{\mathcal{P}\left(\theta_{\text{up}}(X) < \theta | 0\right)} \leq \alpha' \text{ for all } \theta. \tag{5.1}$$

Here, the numerator corresponds to the probability, α, that a nonexistent effect is erroneously detected (type-I error), while the denominator corresponds to the statistical power, $1 - \beta$, with β giving the probability to fail the detection of an existing effect (type-II error). Thus, if Eq. 5.1 is fulfilled, the hypothesis H_0 is rejected.

The actual limit setting is then realised by creating a test statistic, $q_\theta(X)$, from the input yields and finding the value of θ which satisfies

$$\frac{\mathcal{P}\left(q_\theta(X) < q_\theta^*|\theta\right)}{\mathcal{P}\left(q_\theta(X) < q_\theta^*|0\right)} = \alpha', \tag{5.2}$$

whereby q_θ^* is the expected or observed outcome of the experiment. The expected outcome is given by an Asimov data set, which provides the median experimental sensitivity corresponding to the yields given in Tab. 5.1 but without knowledge of the actual data [108].

In this analysis, the upper limits are set at a $1 - \alpha' = 95\%$ confidence level using code based on `HistFactory` which can also take into account statistical and systematic variations to define 1σ and 2σ bands. Here, σ stands for the standard deviation and an excess greater than 3σ would be an evidence of new physics.

The limits obtained in the 1-lepton and 0-lepton final states as well as the combination of these can be found in Fig. 5.1 as a function of considered resonant masses. The limits on non-resonant di-Higgs production are summarised in Tab. 5.2. In the 1-lepton final state, the observed (expected) limit is $\sigma_{gg\to hh} = 23\ \left(26^{+15}_{-7}\right)$ pb, corresponding to 790 (690) times the SM prediction. This is a more stringent limit than in the 0-lepton channel, in which $\sigma_{gg\to hh} = 48\ \left(27^{+13}_{-7}\right)$ pb is observed (expected) corresponding to 1450 (810) times the SM prediction. As expected, only little sensitivity is given to non-resonant di-Higgs production in both final states due to the boosted topology considered in this analysis.

Instead the limits on the high resonant masses are more stringent. The lowest exclusion limit in the 1-lepton final state is obtained for the $m_H = 1000\,\text{GeV}$ mass point with $\sigma_{gg\to H} \times \mathcal{BR}_{H\to hh} = 2.6\ \left(3.0^{+1.7}_{-0.9}\right)$ pb observed (expected) and in the 0-lepton final state is obtained for $m_H = 1500\,\text{GeV}$ mass point with $\sigma_{gg\to H} \times \mathcal{BR}_{H\to hh} = 3.7\ \left(2.1^{+1.0}_{-0.6}\right)$ pb. As mentioned before, the 0-lepton final state profits from its higher signal acceptance and is thus slightly more sensitive at high resonant masses. Nonetheless, the observed limits are all within 1σ and 2σ in the 1-lepton and 0-lepton final state, respectively, of the expected limits (see Figures 5.1 (a) and (b)).

By combining both final states, the limits can be improved. For non-resonant di-Higgs production, a combined upper limit of $\sigma_{gg\to hh} = 27\ \left(16^{+8}_{-4}\right)$ pb is observed (expected) corresponding to 810 (490) times the SM prediction. Here, the lowest upper limit is given

by the $m_H = 1500\,\text{GeV}$ mass point with $\sigma_{gg\to H} \times \mathcal{BR}_{H\to hh} = 2.5\,\left(1.5^{+0.7}_{-0.4}\right)$ pb observed (expected), which is already very close to the assumed cross section of 1 pb. As shown in Fig. 5.1 (c), the observed upper limit is within the 2σ band of the expected limits, consistent with a statistical fluctuation causing this excess.

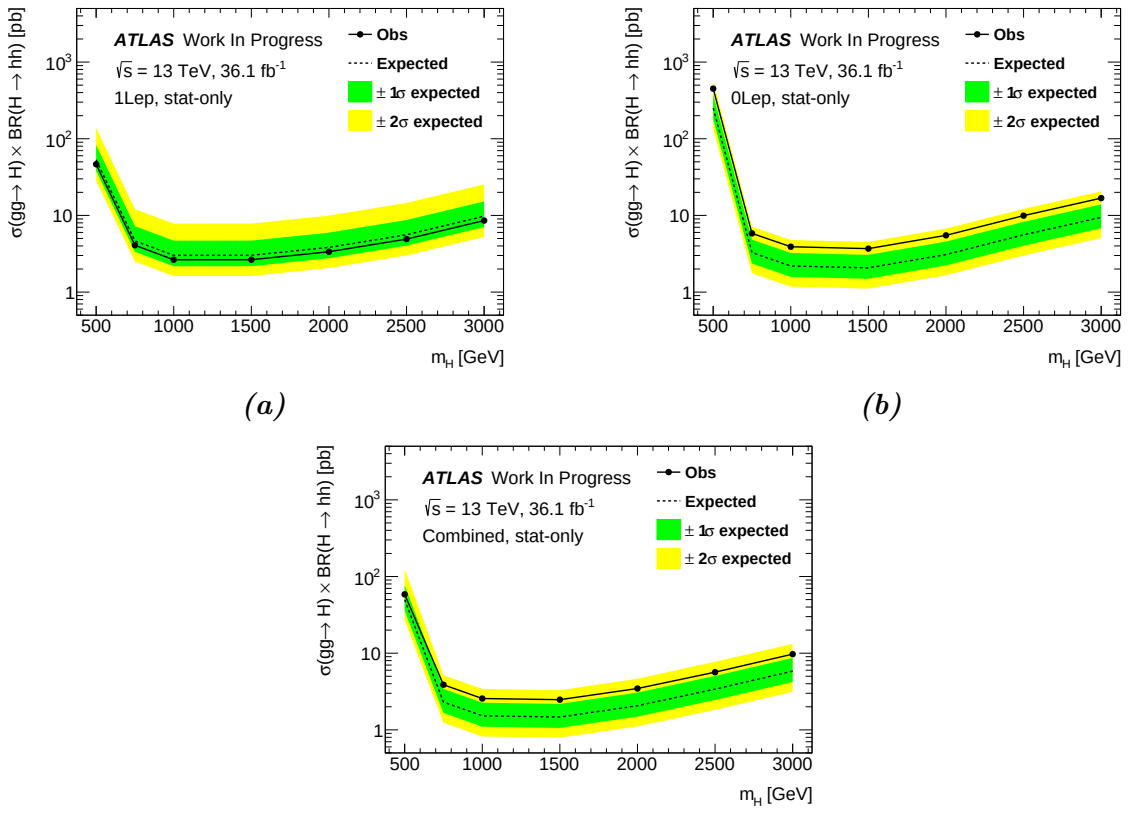

Figure 5.1.: Limits on $\sigma_{gg\to H} \times \mathcal{BR}_{H\to hh}$ in pb as a function of the resonant mass in the (a) 1-lepton and (b) 0-lepton final states and (c) the combination of these with statistical uncertainties only. The actual values can be found in App. A.5.

5.2. Systematic Uncertainties

In this section, the systematic uncertainties will be introduced for both the 1-lepton and 0-lepton final states. Here, the uncertainties are discussed in form of relative uncertainties on the expected event yield and are distinguished in those which are based on theoretical predictions and those that come from the imperfect modelling of the experiment in the simulation. As the continuum background is estimated using a data driven approach, these uncertainties are only applied on the signal and single-Higgs samples since the data does not depend on theoretical predictions or modelling in simulation. Instead, uncertainties

	1-lepton		0-lepton		combined	
	σ [pb]	$\sigma/\sigma_{\mathrm{SM}}$	σ [pb]	$\sigma/\sigma_{\mathrm{SM}}$	σ [pb]	$\sigma/\sigma_{\mathrm{SM}}$
Median	26	790	27	810	16	490
Observed	23	690	48	1450	27	810
$+2\sigma$	69	2060	59	1770	37	1110
$+1\sigma$	41	1230	40	1200	24	730
-1σ	19	570	20	590	12	350
-2σ	14	430	15	440	9	260

Table 5.2.: Obtained upper limits on $\sigma_{gg\to hh}$ for non-resonant di-Higgs production in pb and in terms of σ_{SM} as predicted by the SM for the 1-lepton and 0-lepton final states and the combination of these with statistical uncertainties only.

on the fitting procedure are estimated and a spurious signal estimate is determined for the continuum background.

Due to time constraints, it was not possible to evaluate all uncertainties. However, the considered set contains all the uncertainties which are expected to be most important.

Theoretical Uncertainties

The theoretical uncertainties contain variations on the cross sections, the branching ratios and the PDFs. These are independent from the considered final state since they only affect the production and primary decays. Uncertainties on the W-boson decay are not explicitly included, since inclusive signal samples are used and the final state only results from the applied topological selection.

Therefore, the systematic variation on the branching ratio for the various single-Higgs backgrounds is $\pm 1.7\%$, resulting from the $h \to \gamma\gamma$ decay [56]. In case of the signal samples, the uncertainty from the $h \to WW^*$ must also be included, yielding an uncertainty of $\pm 2.0\%$.

The uncertainties on the cross sections are composed of different factors which are listed in Tab. 5.3 for the signal and background samples [56]. In the end, all of these components are added in quadrature to form an overall uncertainty as single systematic variation. In the case of the resonant di-Higgs production, no systematic variation is considered, since the cross section is only a reference value inspired by the limits set in Run I [101].

Due to time constraints for this thesis, the PDF uncertainties apart from the cross section calculation are neglected. Since the large-R jet collection is infrared safe such that soft partons will not affect the jet reconstruction, a variation of the PDFs used in the hadronisation simulation is assumed to be a minor effect compared to the other systematic

sample	cross section [pb]	scale unc. [%]	theory unc. [%]	α_s unc. [%]	PDF unc. [%]	overall unc. [%]
non-resonant	0.003341	$^{+4.3}_{-6.0}$	± 5	± 2.3	± 2.1	$^{+7.3}_{-8.4}$
resonant	1.0	–	–	–	–	–
ggf	44.08	$^{+7.6}_{-8.1}$	–	± 2.5	± 1.8	$^{+8.2}_{-8.7}$
VBF	3.78	$^{+0.4}_{-0.3}$	–	± 0.5	± 2.1	± 2.1
Wh	1.37	$^{+0.5}_{-0.7}$	–	± 0.9	± 1.7	± 2.0
Zh	0.88	$^{+3.8}_{-3.0}$	–	± 0.9	± 1.3	$^{+4.1}_{-3.5}$
$t\bar{t}h$	0.51	$^{+5.8}_{-9.2}$	–	± 2.0	± 3.0	$^{+6.8}_{-9.9}$

Table 5.3.: Relative uncertainties in % on the cross section for the different samples [56]. For the resonant signal samples, no uncertainties are available, since the cross section is not predicted by any theory but adopted from the limits obtained in Run I.

uncertainties and the statistical uncertainty.

Modelling Uncertainties

Modelling uncertainties result from the imperfect data modelling by the MC simulation. This mostly concerns particle identification efficiencies as well as energy scales and resolutions. Nonetheless, other modelling parameters such as pile-up reweighting and luminosity are also affected.

In the following, the individual systematic variations are described briefly. Here, only the average impact of the uncertainties is given. The actual values for all signal and background samples can be found in App. A.4.

- the e-γ scale and resolution corresponds to the energy bias and the detector resolution concerning electromagnetic showers. Since the calorimeters consist of active and inactive material such as absorber material, read-out electronics or defective cells, the simulated energy must be adjusted to the scale and the resolution of the calorimeter. These adjustments are based on test measurements and thus have an uncertainty.

  While the effect from the scale variation is similar for all signal and background files and of the order of a few percent, the resolution impact depends on the considered sample. For the non-resonant production and resonant masses up to $m_H = 1000\,\text{GeV}$, the uncertainty is of the order of 1%, while the high resonant masses show large uncertainties greater than 10%. The impact on the background samples is in between. This can be explained by the requirement of two well-reconstructed photons not being satisfied due to the worse resolution. Therefore,

the uncertainty is also highly asymmetric, since only few events are gained by a better photon resolution. The effect is comparable for both final states.

- the photon trigger efficiency has a comparably small uncertainty of 0.4% [112]. Since the di-photon trigger is the only one of the available triggers applied, uncertainties on electron and muon triggers are not considered.

- the uncertainties on the photon, electron and muon efficiencies correspond to uncertainties on the applied scale factors. These are used to match the shape of the particle distributions measured in data. The photon efficiency yields the largest variation of the order of a few percent for all signal and background samples in both final states. The effect on the muon and electron efficiencies is comparable and of the order of less than 1% for all samples in the 1-lepton final state and negligible in the 0-lepton final state.

- the jet energy scale (JES) describes the uncertainty concerning the bias on the jet energy. To evaluate this, the small-R and large-R jets are varied simultaneously but using two different configurations. Since hadrons form larger and wider showers in the calorimeter than electrons or photons, the uncertainty is, in general, also larger. However, more photons (and electrons) than jets are part of the selected topology. Therefore, the uncertainties are of the same order of a few percent.

- the small-R jet energy resolution (SRJER) is treated independently from the resolution of large-R jets since they are considered to be different objects. However, no effect is observable for the systematic variation on SRJER in either final states.

- the large-R jet energy and mass resolution (LRJER and LRJMR) are derived by varying the p_T and mass of the large-R jets. While for the energy resolution the p_T is smeared by a Gaussian distribution with a width of 2%, only a relative error is provided for the mass. Therefore, the distribution of the ratio of the mass between ΔR-matched truth and reconstructed jets is fitted with a Gaussian distribution. The obtained width is combined with the relative uncertainty to a new width, which is then used to smear the mass of the large-R jet. These variations are of the order of a few percent in both final states and need to be symmetrised afterwards.

- the substructure resolution is only relevant for the 0-lepton final state, since no substructure variables are considered in the 1-lepton final state. This is neglected due to time constraints.

- flavour tagging is a complex procedure to identify jets coming from b- or c-hadrons. Due to the b-veto in the preselection (see Sec. 4.5), a variation in the tagging efficiency has an impact on the event estimate. However, no effect is observed in both final states and, thus, this variation is not further investigated in the following.

- the pile-up reweighting (PRW) is a correction applied to the MC samples to match the actual data. Nonetheless, the reweighting has an uncertainty due to a limited set of measurements to determine the amount and shape of pile-up. This yields a relative change on the number of expected events ranging from 1% to 2%.

A luminosity of $\int \mathcal{L} \mathrm{d}t = 36.1\,\mathrm{fb}^{-1}$ is used in the MC reweighting to match the data set collected by ATLAS in 2015 and 2016. However, this value corresponds to the GRL and calculated from luminosity blocks which yields a relative uncertainty of $\pm 3.2\%$ following the method described in [100].

Since all signal samples are produced using the AFII detector simulation which, in general, results in observables that are comparable to those from the full detector simulation using GEANT4, this also has to be considered as possible source for imperfect modelling. Therefore, statistically independent sets of events for the $m_H = 1500\,\mathrm{GeV}$ and the $m_H = 3000\,\mathrm{GeV}$ mass points are simulated with GEANT4. The full sample names are given in App. A.1. The difference in the expected event yields after the complete selection between full and fast simulation at both mass points is then treated as systematic uncertainty. To ensure that this uncertainty is not underestimated, the largest effect is symmetrised and applied to all other signal samples as well. Thus, the systematic variation is taken to be $\pm 6.4\%$ for the 1-lepton final state and $\pm 7.4\%$ for the 0-lepton final state.

Fit Uncertainties

Until now, only uncertainties on the MC samples have been considered. In the following, uncertainties on the continuum background estimate are discussed.

The first assumption concerns the fit range. To preserve as much statistics as possible, the fit range was widened from $105\,\mathrm{GeV} \leq m_{\gamma\gamma} \leq 160\,\mathrm{GeV}$ to $94.49\,\mathrm{GeV} \leq m_{\gamma\gamma} \leq 162.49\,\mathrm{GeV}$. This range is divided into ten bins with a width of $6.8\,\mathrm{GeV}$ each. This choice is motivated by aiming to contain the complete signal region in one bin. To have a measure of the systematic uncertainty, the fit range is varied by plus and minus one bin on each edge. The effect is depicted in Fig. 5.2. In the 0-lepton final state, both variations result in a higher event yield, of which the largest one is chosen and symmetrised to yield an uncertainty of $\pm 34.7\%$ on the continuum background yield. In contrast in the 1-lepton

final state, the variation results in an asymmetric uncertainty of +33.3% and −11.1% due to changes in the number of sideband events used in the extrapolation to the signal region.

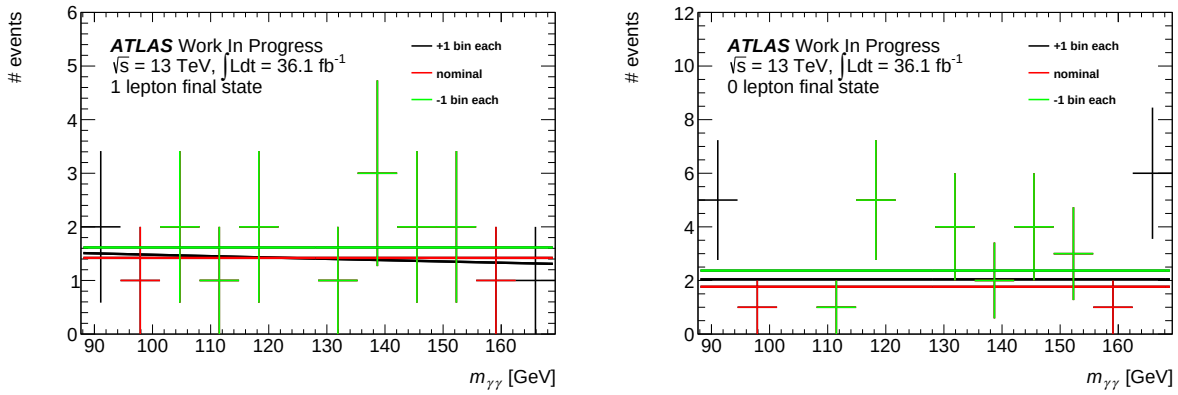

(a) *(b)*

Figure 5.2.: Effect of the systematic variation on the fit range (a) in the 1-lepton final state with loose photons and (b) in the 0-lepton final state. The inner data points are overlaid by the data points of the smaller fit range. In (a) the difference shown is not equivalent to the systematic uncertainty, since the change in the extrapolation factor is not considered.

The second assumption concerns the signal region ($|m_{\gamma\gamma} - m_h| < 2\sigma_{\gamma\gamma}$) and is that the impact of single-Higgs production on the fit outside the $\sigma_{\gamma\gamma}$ is negligible. The corresponding uncertainty is derived from blinding events inside a $3\sigma_{\gamma\gamma}$ band and determining the yield for the continuum background within $|m_{\gamma\gamma} - m_h| < 2\sigma_{\gamma\gamma}$. This uncertainty is then symmetrised and found to be ±5.1% in the 0-lepton final state, and is deemed to be negligible for the 1-lepton final state.

Another uncertainty arises from the assumption of a falling exponential form of the $m_{\gamma\gamma}$ fit. As discussed in Sec. 4.7, the slope of the exponential is constrained to be $b \leq 0$. To evaluate the uncertainty, the difference on the background estimate are calculated with and without restricting b. The results are shown in Fig. 5.3 and yield a relative uncertainty on the event estimate of ±1.1% in the 1-lepton final state and ±1.7% in the 0-lepton final state.

Another uncertainty that is only relevant for the 1-lepton final state concerns the extrapolation from loose to tight photons. As depicted in Fig. 5.4, the $m_{\gamma\gamma}$ distributions are similar between the loose photon control region and the tight photon signal region. To estimate the uncertainty on this extrapolation, the difference between the predicted fractions of events in the signal region from a fit to the $m_{\gamma\gamma}$ spectrum using the tight photon and loose photon selection is considered. Here, no large-R jet or lepton selection

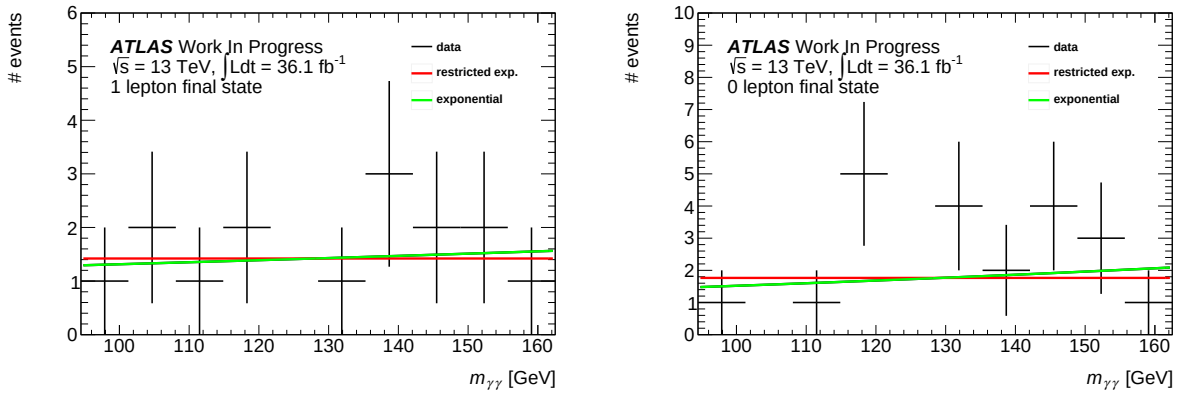

Figure 5.3.: Effect of the restricted exponential (red) compared to the unrestricted exponential (green) (a) in the 1-lepton final state with loose photons and (b) in the 0-lepton final state.

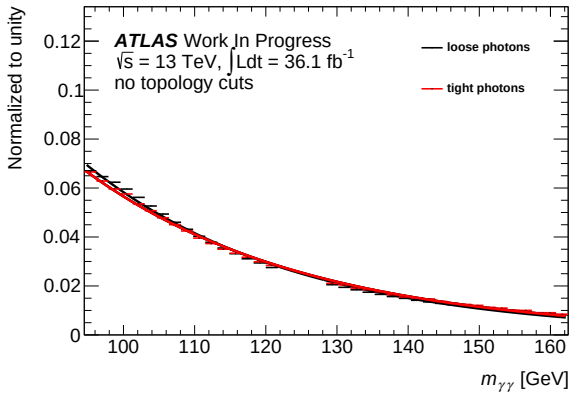

Figure 5.4.: Difference between the $m_{\gamma\gamma}$ distributions using loose photons (black) and tight photons (red) without the large-R jet and lepton requirements.

is required to ensure that the evaluated systematic variation is not sensitive to statistical fluctuations. This systematic variation gives a relative uncertainty of $\pm 0.8\%$.

Spurious Signal

The final uncertainty that is evaluated concerns the probability that signal-like events arise from a sample of pure background events due to statistical fluctuations or to the specific selection criteria. Since a background-only sample with sufficiently large statistics is required, this can only be realised by the use of MC samples of photons plus jets (plus leptons). For the 1-lepton final state, a $\gamma\gamma\ell\nu jj$ sample with 2097000 generated events is available. This was created using the generators MADGRAPH for the matrix element calculation and PYTHIA 8 with AU2 tune [113] and the NN23PDFLO and MSTW2008LO PDF sets [114] for parton showering. Considering the 0-lepton final state, an even larger

$\gamma\gamma$+jets sample generated by SHERPA [115] in the CT10 tune with 104779895 generated events can be used.

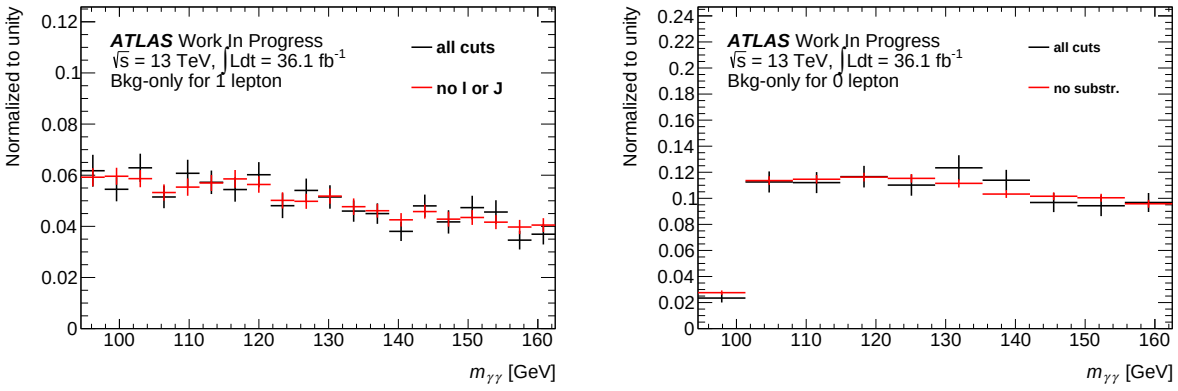

(a) *(b)*

Figure 5.5.: Background-only di-photon mass distributions at different selection stages (a) in the one lepton final state and (b) in the zero lepton final state.

Here, the $m_{\gamma\gamma}$ distributions from these samples as shown in Fig. 5.5 are fitted with an exponential in the dedicated fit range to extract the slope of the distribution. The selection is loosened in the 1-lepton final state by removing the requirements on the large-R jet and the lepton, since this doubles the statistics and the slope of the distribution is not affected by these criteria. In the 0-lepton final state, the cuts on the substructure variables are removed to increase the statistics by a factor of seven without affecting the shape significantly. Additionally, the first bin is removed because this mass range was not considered in the event generation and, thus, is not modelled properly.

Then, pseudo experiments are generated with a $m_{\gamma\gamma}$ distribution using the fundamental form of the previous fit. These correspond to an arbitrary often repeated ATLAS experiment in the current setup. The number of events per pseudo experiment is based on a Poisson distribution with the mean corresponding to the continuum background-only estimate in data in the complete fit range.

The $m_{\gamma\gamma}$ distribution resulting from the pseudo-experiment is then fitted to the function

$$f(m_{\gamma\gamma}) = \exp(a + b \cdot m_{\gamma\gamma}) + c \cdot \exp\left(-\frac{(m_{\gamma\gamma} - m_h)^2}{2\sigma_{\gamma\gamma}^2}\right), \tag{5.3}$$

whereby b is restricted to non-positive values. Here, the exponential describes the form of the background, while the Gaussian distribution with its mean at the Higgs mass and the width of the di-photon mass resolution corresponds to the spurious signal that assesses how robust the fit is in predicting background yields. Therefore, the integral of

the Gaussian, N_{int}, is a measure for the number of signal events resulting from statistical fluctuations of the background.

After generating $N_{\text{it}} = 10^7$ pseudo experiments, the absolute mean

$$N_{\text{SpuSi}} = \sum_{i=1}^{N_{\text{it}}} \frac{|N_{\text{int},i}|}{N_{\text{it}}} \tag{5.4}$$

is used to estimate the systematic variation on the background yield. For the 1-lepton state, $N_{\text{SpuSi}} = 0.04$ is obtained and $N_{\text{SpuSi}} = 0.59$ for the 0-lepton final state. These correspond to a relative uncertainty of $\pm 44.4\%$ and $\pm 33.5\%$, respectively on the continuum background estimate.

Summary

In the Tables A.9 to A.12 in App. A.4, all considered systematic uncertainties are summarised for the different signal mass points and backgrounds in both final states. They are given in terms of relative uncertainties in the signal region. Systematic uncertainties which are larger than 100% are restricted to 100% because these are dominated by statistical fluctuations. This only affects the jet energy scale for the ggf process in the 1-lepton final state.

In general, all systematic uncertainties are of the order of the statistical uncertainty or below. Exceptions are the e-γ resolution for high mass points and the jet energy scale for the $m_H = 500\,\text{GeV}$ sample in both final states. Regarding the continuum background, the largest uncertainty is given by the statistical uncertainty followed by the spurious signal and the uncertainty on the fit range, which are also highly dependent on the statistics.

Nonetheless, the systematic variations are reasonable and the most important are considered. Not included are resolution effects on substructure variables which are only relevant for the 0-lepton final state and uncertainties on the parton distribution functions. These were not investigated due to time limitations.

5.3. Limits with Statistical and Systematic Uncertainties

The systematic uncertainties are now included in the limit setting in addition to the statistical uncertainties. Thereby, the general procedure does not change. The number of observed events is unaffected and upper CL_s limits on the cross section times branching ratio are set at a 95% confidence level.

The resulting limits are plotted in Fig. 5.6 as a function of the considered resonant masses and summarised in Tab. 5.4 for non-resonant production.

For non-resonant di-Higgs production in the 1-lepton final state, an exclusion limit on the cross section of $\sigma_{gg\to hh} = 24\ \left(27^{+15}_{-8}\right)$ pb is observed (expected). This corresponds to 710 (800) times the SM prediction, respectively. Again, the 0-lepton final state yields a higher upper limit with $\sigma_{gg\to hh} = 48\ \left(28^{+13}_{-8}\right)$ pb observed (expected) corresponding to 1450 (830) times the SM prediction. In the combination, a lower upper limit is found with $\sigma_{gg\to hh} = 29\ \left(17^{+9}_{-5}\,\text{pb}\right)$ observed (expected) corresponding to 860 (510) times the SM prediction.

In the 1-lepton final state, the best result is obtained for $m_H = 1000\,\text{GeV}$ mass point with an upper limit of $\sigma_{gg\to H} \times \mathcal{BR}_{H\to hh} = 2.7\ \left(3.0^{+1.7}_{-0.8}\right)$ pb observed (expected). In the 0-lepton final state and in the combination of both final states, the $m_H = 1500\,\text{GeV}$ mass point yields the most stringent limit with $\sigma_{gg\to H} \times \mathcal{BR}_{H\to hh} = 3.8\ \left(2.2^{+1.1}_{-0.6}\right)$ pb and $\sigma_{gg\to H} \times \mathcal{BR}_{H\to hh} = 2.6\ \left(1.6^{+0.8}_{-0.4}\right)$ pb observed (expected), respectively.

	1-lepton		0-lepton		combined	
	σ [pb]	$\sigma/\sigma_{\text{SM}}$	σ [pb]	$\sigma/\sigma_{\text{SM}}$	σ [pb]	$\sigma/\sigma_{\text{SM}}$
Median	27	800	28	830	17	510
Observed	24	710	48	1450	29	860
$+2\sigma$	73	2190	62	1860	40	1200
$+1\sigma$	42	1270	41	1230	26	770
-1σ	19	580	20	600	12	370
-2σ	15	430	15	450	9	280

Table 5.4.: Obtained upper limits on $\sigma_{gg\to hh}$ for non-resonant di-Higgs production in pb and in terms of σ_{SM} as predicted by the SM for the 1-lepton and 0-lepton final states and the combination of these with statistical and systematic uncertainties included.

Compared to the upper limits obtained with statistical uncertainties only, the values for the limits with systematic uncertainties included increase only slightly since this analysis is dominated by the statistical limitations. All observed limits are still within the 2σ bands of the expected upper limit as shown in Fig. 5.6.

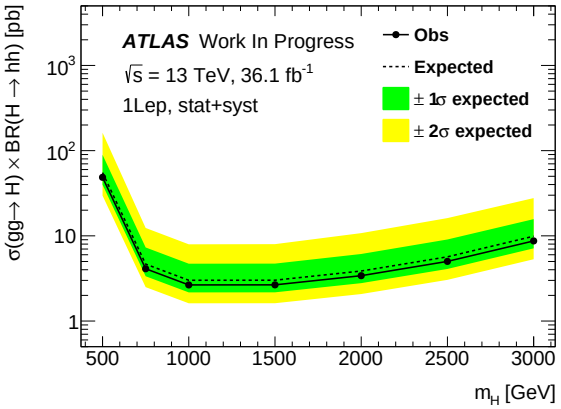

(a) One lepton final state.

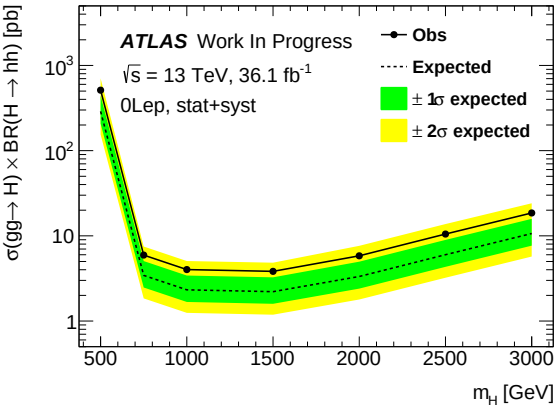

(b) Zero lepton final state.

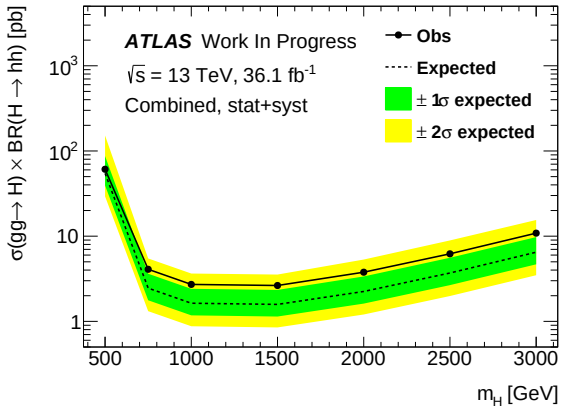

(c) Combined.

Figure 5.6.: Limits on $\sigma_{gg\to H} \times \mathcal{BR}_{H\to hh}$ in pb as a function of the resonant mass in the 1-lepton and 0-lepton final states with statistical and systematic uncertainties included.

6. Conclusion and Outlook

In this analysis, a search for di-Higgs production was performed. The non-resonant production mode as predicted by the SM and heavy resonances with a mass above $m_H = 500\,\text{GeV}$ decaying to light Higgs boson pairs were considered. Thus, the boosted topology was used in the event selection. Due to the clean signature and relatively high branching ratio, the $\gamma\gamma WW^*$ decay channel was mainly investigated in the 1-lepton final state ($WW^* \to qq\ell\nu$) which resulted in a unique topology requirement of two photons, at least one large-R jet and exactly one lepton, i.e. electron or muon. The 0-lepton ($WW^* \to 4q$) final state was investigated based on the studies in [110], particularly in the evaluation of systematic uncertainties and obtaining upper limits on the cross section.

The main backgrounds were continuum di-photon production and single-Higgs production with the Higgs boson decaying in two photons. For the continuum background, a data driven approach with blinded signal region was used, while the single-Higgs and signal samples were simulated using MC event generators. The analysis was highly limited by the continuum background statistics. Thus, the loose photon control region was chosen to enhance the statistics without changing the event selection significantly.

To maximise the signal significance, an optimisation on the $m_H = 750\,\text{GeV}$ mass point was performed which resulted in two cuts being added to the event selection:

- $p_{T,\gamma\gamma} > 200\,\text{GeV}$ and
- $\Delta R_{\ell J} < 1.6$

These yield a maximum significance of $\Sigma = 0.92 \pm 0.17$. The predicted yields for the final optimised selection are

$$N_{\text{sig}}^{\text{non-res}} = 0.0029 \pm 0.0001,\ N_{\text{sig}}^{750\,\text{GeV}} = 0.51 \pm 0.01,$$
$$N_{\gamma\gamma} = 0.09 \pm 0.10 \text{ and } N_{\text{single-}h} = 0.087 \pm 0.005.$$

A luminosity of $\int \mathcal{L} \mathrm{d}t = 36.1\,\text{fb}^{-1}$ is used to match the data collect by ATLAS in 2015 and 2016. The cross section is determined by the SM predictions for non-resonant di-Higgs production and single-Higgs production. For the resonant production, an assumed cross section of $\sigma = 1\,\text{pb}$ is used.

Systematic variations were taken into account and evaluated for both final states. Overall, the largest uncertainty resulted from the statistical limitation of the continuum background followed by systematic variations of the fit range and the spurious signal.

In the unblinded signal region, no excess was observed in the 1-lepton final state and, thus, limits on the cross section were set and combined with the 0-lepton final state. For the non-resonant production, a combined upper limit of $\sigma_{gg\to hh} = 29\ \left(17^{+9}_{-5}\right)$ pb was observed (expected) corresponding to 860 (510) times the SM prediction. The best combined limit was found for the $m_H = 1500\,\text{GeV}$ mass point with $\sigma_{gg\to H} \times \mathcal{BR}_{H\to hh} = 2.6\ \left(1.6^{+0.8}_{-0.5}\right)$ pb observed (expected).

As it was not expected to have any sensitivity to small resonance masses or the non-resonant production mode, the results are quite promising. Especially, the high resonant masses around $m_H = 1000\,\text{GeV}$ nearly reached the upper limits determined in Run I. At this point only a combination of the $\gamma\gamma WW^*$ channels was performed. A future combination with the $b\bar{b}\gamma\gamma$ and $b\bar{b}WW^*$ channels is possible. This allows a simple combination with those channels as well, whereby the $b\bar{b}\gamma\gamma$ channel is regarded as the most promising one for a discovery at moment.

However, with increasing statistics, this channel will provide a beneficial signal over background ratio itself. Due to its topological requirements of at least one large-R jet and exactly one lepton, a large amount of background coming from pile-up can be rejected which is a large advantage for the high luminosity LHC coming in the near future. With an expected integrated luminosity of approximately $\int \mathcal{L}dt = 3000\,\text{fb}^{-1}$ in 2030, the Higgs self-coupling as it is predicted by the SM is expected to be measurable. This will be one more important test of whether the recently discovered scalar boson is truly the Higgs boson predicted by the SM. The search for heavy resonances will also become more sensitive and harder cuts can be applied or multivariate analysis techniques can be used.

A. Additional Tables

A.1. MC Samples

In this section, the full names of all considered samples are listed. These are distinguished in signal samples (Tab. A.1), single-Higgs samples (Tab. A.2) and the samples used to obtain a distribution estimate of a pure continuum background for the spurious signal (Tab. A.3).

Mass point [GeV]	Sample name
non-resonant	mc15_13TeV.342621.aMcAtNloHerwigppEvtGen_UEEE5_CTEQ6L1_CT10ME_hh_yyWW.merge.AOD.e4419_a766_a821_r7676
260	mc15_13TeV.343756.aMcAtNloHerwigppEvtGen_UEEE5_CTEQ6L1_CT10ME_Xhh_m260_yyWW.merge.AOD.e5153_a766_a821_r7676
300	mc15_13TeV.343758.aMcAtNloHerwigppEvtGen_UEEE5_CTEQ6L1_CT10ME_Xhh_m300_yyWW.merge.AOD.e5153_a766_a821_r7676
400	mc15_13TeV.343761.aMcAtNloHerwigppEvtGen_UEEE5_CTEQ6L1_CT10ME_Xhh_m400_yyWW.merge.AOD.e5153_a766_a821_r7676
500	mc15_13TeV.343763.aMcAtNloHerwigppEvtGen_UEEE5_CTEQ6L1_CT10ME_Xhh_m500_yyWW.merge.AOD.e5153_a766_a821_r7676
750	mc15_13TeV.343818.aMcAtNloHerwigppEvtGen_UEEE5_CTEQ6L1_CT10ME_Xhh_m750_yyWW.merge.AOD.e5153_a766_a821_r7676
1000	mc15_13TeV.343819.aMcAtNloHerwigppEvtGen_UEEE5_CTEQ6L1_CT10ME_Xhh_m1000_yyWW.merge.AOD.e5153_a766_a821_r7676
1500	mc15_13TeV.343820.aMcAtNloHerwigppEvtGen_UEEE5_CTEQ6L1_CT10ME_Xhh_m1500_yyWW.merge.AOD.e5153_a766_a821_r7676
2000	mc15_13TeV.343821.aMcAtNloHerwigppEvtGen_UEEE5_CTEQ6L1_CT10ME_Xhh_m2000_yyWW.merge.AOD.e5153_a766_a821_r7676
2500	mc15_13TeV.343822.aMcAtNloHerwigppEvtGen_UEEE5_CTEQ6L1_CT10ME_Xhh_m2500_yyWW.merge.AOD.e5153_a766_a821_r7676

Mass point [GeV]	Sample name
3000	mc15_13TeV.343823.aMcAtNloHerwigppEvtGen_UEEE5_CTEQ6L1_ CT10ME_Xhh_m3000_yyWW.merge.AOD.e5153_a766_a821_r7676
1500 (FullSim)	mc15_13TeV.343820.aMcAtNloHerwigppEvtGen_UEEE5_CTEQ6L1_ CT10ME_Xhh_m1500_yyWW.merge.AOD.e5153_s2726_r7772_r7676
3000 (FullSim)	mc15_13TeV.343823.aMcAtNloHerwigppEvtGen_UEEE5_CTEQ6L1_ CT10ME_Xhh_m3000_yyWW.merge.AOD.e5153_s2726_r7772_r7676

Table A.1.: Full signal signal samples names for the non-resonant production as well as for all available mass points. All those samples are lepton number inclusive.

Background	Sample name
ggf	mc15_13TeV.341000.PowhegPythia8EvtGen_CT10_AZNLOCTEQ6L1_ ggH125_gamgam.merge.AOD.e3806_s2984_r8585_r7676
vbf	mc15_13TeV.341001.PowhegPythia8EvtGen_CT10_AZNLOCTEQ6L1_ VBFH125_gamgam.merge.AOD.e3806_s2608_r7772_r7676
Wh	mc15_13TeV.341067.Pythia8EvtGen_A14NNPDF23LO_WH125_gamgam. merge.AOD.e3796_s2608_s2183_r7772_r7676
Zh	mc15_13TeV.341068.Pythia8EvtGen_A14NNPDF23LO_ZH125_gamgam. merge.AOD.e3796_s2608_s2183_r7772_r7676
$t\bar{t}h$	mc15_13TeV.341081.aMcAtNloHerwigppEvtGen_UEEE5_CTEQ6L1_ CT10ME_ttH125_gamgam.merge.AOD.e4277_s2608_s2183_r7772_r7676

Table A.2.: Single-Higgs background sample names with the dedicated Higgs decay in two photons.

Background	Sample name
$\gamma\gamma\ell\nu jj$	mc15_13TeV.343363.MGPy8_AU2_M8LO_nn23lo1ME_sm_lnugamgamjj_ qcd2_13TeV.merge.AOD.e4852_a766_a821_r7676
$\gamma\gamma$+jets	mc15_13TeV.341939.Sherpa_CT10_2DP20_myy_100_165.merge.AOD. e4407_a766_a818_r7676

Table A.3.: Samples names to estimate the pure continuum di-photon background in the spurious signal calculation.

A.2. Overlap Removal

Mass point [GeV]	electrons	muons	0 lepton events	1 lepton events	2 lepton events
non-res.	3.2%	21.7%	-3.9%	15.2%	1.6%
500	0.4%	9.3%	-2.0%	5.8%	1.1%
750	2.5%	24.0%	-4.4%	16.0%	1.6%
1000	5.3%	38.0%	-5.6%	26.1%	2.2%
1500	9.8%	53.6%	-5.6%	41.4%	2.7%
2000	10.8%	61.0%	-4.9%	50.8%	3.0%
2500	12.0%	61.5%	-4.4%	54.8%	3.4%
3000	10.0%	56.8%	-3.9%	51.7%	3.1%

Table A.4.: Overview on the relative change of the overall amount of leptons and of the events with a dedicated final state from the nominal OLR to the p_T dependent OLR. This values are calculated after the preselection without any requirements on leptons or large-R jets, respectively.

A.3. Cutflows

In this section, detailed cutflows on the expected event estimate for all signal and single-Higgs samples are given in both final states. Additionally, the number of events in the $m_{\gamma\gamma}$ sidebands as well as the number of observed events in the signal region can be found in tables considering the singe-Higgs backgrounds.

Selection	Mass point m_H [GeV]										
	non-resonant	260	300	400	500	750	1000	1500	2000	2500	3000
N_{DxAOD}	0.389	10.994	19.985	11.470	11.600	12.583	12.982	13.490	13.550	11.325	8.780
DQ	0.372	10.559	19.090	10.849	11.078	12.253	12.739	13.332	13.431	11.226	8.688
≥ 2 loose photons	0.309	8.895	15.867	8.982	9.165	10.332	10.921	11.637	11.830	9.848	7.475
trigger match	0.308	8.855	15.796	8.940	9.123	10.275	10.848	11.536	11.715	9.757	7.406
photon ID	0.308	8.855	15.796	8.940	9.123	10.275	10.848	11.536	11.715	9.757	7.406
isolation	0.271	7.275	13.243	7.819	8.151	9.335	9.961	10.700	10.925	8.959	6.279
rel. p_T^γ cuts	0.247	6.739	11.842	7.032	7.514	8.911	9.645	10.473	10.763	8.819	6.167
fit range	0.247	6.723	11.822	7.003	7.478	8.879	9.617	10.453	10.748	8.808	6.159
signal region	0.224	5.913	10.460	6.322	6.845	8.265	8.979	9.771	10.035	8.191	5.728
b-veto	0.220	5.859	10.353	6.230	6.733	8.095	8.785	9.566	9.832	8.029	5.599
≥ 1 large-R jet	0.035	0.008	0.056	0.182	0.968	4.565	6.275	7.940	8.563	7.087	4.960
1 lepton	0.005	0.002	0.012	0.034	0.134	0.620	0.907	0.924	0.753	0.537	0.332
$p_{T,\gamma\gamma} > 200\,\text{GeV}$	0.004	0.000	0.002	0.011	0.070	0.595	0.895	0.920	0.751	0.536	0.332
$\Delta R_{\ell J} < 1.6$	0.003	0.000	0.000	0.002	0.045	0.510	0.788	0.787	0.620	0.424	0.243

Table A.5.: Detailed cutflow for all signal samples in the 1-lepton final state. As mentioned in Sec. 4.5, mass points below $m_H < 500\,\text{GeV}$ show no sensitivity in the boosted topology.

Selection	$\gamma\gamma$ observed	$\gamma\gamma$ sidebands	ggf	vbf	Wh	Zh	$t\bar{t}h$
N_{DxAOD}	111112680	111112680	2239.772	208.918	65.392	42.729	30.793
DQ	97814823	97814823	2157.697	199.255	62.731	40.963	29.549
≥ 2 loose photons	29968480	29968480	1805.201	166.523	49.428	33.053	24.336
trigger match	29887286	29887286	1801.832	166.104	49.259	32.962	24.173
photon ID	4436503	29887286	1565.059	143.701	42.308	28.332	20.128
isolation	1640858	29887286	1401.291	129.837	37.312	24.941	16.576
rel. p_T^γ cuts	1431673	23879083	1300.577	117.945	34.182	22.784	15.120
fit range	492673	8316379	1300.329	117.831	33.955	22.656	15.040
signal region	45299	7593241*	1174.530	107.677	30.880	20.614	13.937
b-veto	44924	7524681	1167.366	106.609	30.676	18.974	5.264
≥ 1 large-R jet	266	47050	13.828	2.886	1.814	1.094	1.564
1 lepton	4	190	0.010	0.002	0.067	0.023	0.367
$p_{T,\gamma\gamma} > 200\,\text{GeV}$	1	62	0.003	0.002	0.045	0.014	0.157
$\Delta R_{\ell J} < 1.6$	0	15	0.001	0.000	0.017	0.011	0.059

Table A.6.: Detailed cutflow of the number of observed events in the unblinded signal region, the number of events in the $m_{\gamma\gamma}$ sidebands using loose photon criteria and all considered single-Higgs backgrounds in the 1-lepton final state.
* This cut is inverted to blind the signal region.

Selection	Mass point m_H [GeV]										
	non-resonant	260	300	400	500	750	1000	1500	2000	2500	3000
N_{DxAOD}	0.389	10.994	19.985	11.470	11.600	12.583	12.982	13.490	13.550	11.325	8.780
DQ	0.372	10.559	19.090	10.849	11.078	12.253	12.739	13.332	13.431	11.226	8.688
≥ 2 loose photons	0.302	8.797	15.622	8.805	8.931	9.966	10.502	11.191	11.383	9.421	7.072
trigger match	0.300	8.758	15.557	8.766	8.894	9.913	10.436	11.098	11.279	9.339	7.009
photon ID	0.300	8.758	15.557	8.766	8.894	9.913	10.436	11.098	11.279	9.339	7.009
isolation	0.267	7.202	13.077	7.702	8.000	9.107	9.689	10.426	10.655	8.717	6.120
rel. p_T^γ cuts	0.243	6.668	11.681	6.921	7.370	8.695	9.384	10.211	10.503	8.588	6.016
fit range	0.242	6.657	11.668	6.909	7.354	8.685	9.375	10.205	10.500	8.586	6.014
signal region	0.220	5.857	10.334	6.241	6.732	8.084	8.752	9.537	9.803	7.985	5.591
b-veto	0.217	5.804	10.228	6.149	6.621	7.916	8.563	9.336	9.605	7.827	5.466
≥ 1 large-R jet	0.035	0.008	0.055	0.180	0.948	4.455	6.108	7.747	8.370	6.915	4.844
0 lepton	0.029	0.005	0.041	0.143	0.805	3.804	5.151	6.747	7.527	6.304	4.446
$p_{T,\gamma\gamma} > 275\,\text{GeV}$	0.013	0.000	0.000	0.011	0.070	3.045	4.876	6.665	7.498	6.291	4.441
$\tau_{42} < 0.475$	0.008	0.000	0.000	0.003	0.027	1.823	2.886	3.936	4.448	3.742	2.621
$C_1 > 0.08$	0.007	0.000	0.000	0.002	0.021	1.672	2.471	2.601	1.747	0.970	0.581

Table A.7.: Detailed cutflow for all signal samples in the 0-lepton final state [110].

Selection	$\gamma\gamma$ observed	$\gamma\gamma$ sidebands	ggf	vbf	Wh	Zh	$t\bar{t}h$
N_{DxAOD}	111112680	111112680	2239.772	208.918	65.392	42.729	30.793
DQ	97814823	97814823	2157.696	199.255	62.731	40.963	29.549
≥ 2 loose photons	29866531	29866531	1800.586	164.575	48.283	32.380	23.313
trigger match	29794061	29794061	1797.335	164.216	48.131	32.300	23.175
photon ID	4422423	4422423	1562.192	142.637	41.513	27.862	19.539
isolation	1635695	1635695	1398.934	129.003	36.667	24.554	16.145
rel. p_T^γ cuts	1427304	1427304	1298.330	117.165	33.559	22.408	14.708
fit range	490962	490962	1298.185	117.104	33.441	22.340	14.670
signal region	45134	445828*	1172.598	107.026	30.457	20.342	13.608
b-veto	44764	442646	1165.448	105.963	30.256	18.713	5.124
≥ 1 large-R jet	264	2176	13.726	2.859	1.782	1.069	1.516
0 lepton	260	2158	13.716	2.857	1.716	1.007	1.126
$p_{T,\gamma\gamma} > 275\,\text{GeV}$	41	283	6.555	1.274	0.693	0.447	0.270
$\tau_{42} < 0.475$	14	42	1.087	0.234	0.183	0.123	0.140
$C_1 > 0.08$	7	21	0.748	0.086	0.14	0.102	0.126

Table A.8.: Detailed cutflow of the observed events in the unblinded signal region, the number of events in the $m_{\gamma\gamma}$ sidebands and all considered single-Higgs backgrounds in the 0-lepton final state [110].

* This cut is inverted to blind the signal region.

A.4. Systematic Uncertainties

uncertainty	Non-res.	Mass point m_H [GeV]						
		500	750	1000	1500	2000	2500	3000
stat	3.1	6.7	2.0	1.5	1.4	1.6	1.9	2.5
	-3.1	-6.7	-2.0	-1.5	-1.4	-1.6	-1.9	-2.5
σ	7.3	0.0	0.0	0.0	0.0	0.0	0.0	0.0
	-8.4	0.0	0.0	0.0	0.0	0.0	0.0	0.0
$\mathcal{BR}$	2.0	2.0	2.0	2.0	2.0	2.0	2.0	2.0
	-2.0	-2.0	-2.0	-2.0	-2.0	-2.0	-2.0	-2.0
$\int \mathcal{L} dt$	3.2	3.2	3.2	3.2	3.2	3.2	3.2	3.2
	-3.2	-3.2	-3.2	-3.2	-3.2	-3.2	-3.2	-3.2
FastSim	6.4	6.4	6.4	6.4	6.4	6.4	6.4	6.4
	-6.4	-6.4	-6.4	-6.4	-6.4	-6.4	-6.4	-6.4
e-γ res.	0.0	1.0	0.5	0.0	0.0	0.0	0.0	0.0
	-0.8	0.0	-1.0	-0.9	-5.3	-13.0	-15.1	-13.5
e-γ scale	0.0	0.1	0.0	0.0	0.0	0.0	0.0	0.0
	-2.2	-3.0	-2.1	-2.1	-2.8	-3.5	-3.4	-3.8
γ eff.	2.6	2.4	2.6	2.8	3.1	3.4	3.6	3.7
	-2.6	-2.4	-2.6	-2.8	-3.1	-3.3	-3.5	-3.6
γ trigger	0.4	0.4	0.4	0.4	0.4	0.4	0.4	0.4
	-0.4	-0.4	-0.4	-0.4	-0.4	-0.4	-0.4	-0.4
e eff.	0.8	0.7	0.8	0.8	0.8	0.8	0.8	0.8
	-0.8	-0.7	-0.8	-0.8	-0.8	-0.8	-0.8	-0.8
μ eff.	0.2	0.3	0.2	0.3	0.4	0.5	0.6	0.6
	-0.2	-0.2	-0.2	-0.3	-0.4	-0.5	-0.6	-0.6
JES	9.8	16.2	4.9	2.7	1.5	0.9	0.6	0.5
	-6.8	-18.9	-5.5	-3.2	-1.4	-0.9	-0.6	-0.6
LRJMR	2.7	0.4	0.0	0.8	0.9	1.8	1.4	2.4
	-2.7	-0.4	0.0	-0.8	-0.9	-1.8	-1.4	-2.4
LRJER	2.3	0.4	0.0	0.7	0.6	2.0	1.1	2.5
	-2.3	-0.4	0.0	-0.7	-0.6	-2.0	-1.1	-2.5
PRW	2.6	0.0	0.0	0.8	1.0	2.0	0.6	1.3
	-0.4	-2.1	-0.2	0.0	-0.7	-0.5	-0.9	-2.5

Table A.9.: Summary of all considered relative variations on the expected event yield of the signals in the 1-lepton final state. All entries are given in %.

uncertainty	single-Higgs background					Continuum
	ggf	vbf	Wh	Zh	$t\bar{t}h$	background
stat	100.0	75.0	17.6	18.2	6.8	106.3
	-100.0	-75.0	-17.6	-18.2	-6.8	-100.0
σ	8.2	2.1	2.0	4.1	6.8	0.0
	-8.7	-2.1	-2.0	-3.5	-9.9	0.0
$\mathcal{BR}$	1.7	1.7	1.7	1.7	1.7	0.0
	-1.7	-1.7	-1.7	-1.7	-1.7	0.0
$\int \mathcal{L} dt$	3.2	3.2	3.2	3.2	3.2	0.0
	-3.2	-3.2	-3.2	-3.2	-3.2	0.0
FastSim	0.0	0.0	0.0	0.0	0.0	0.0
	0.0	0.0	0.0	0.0	0.0	0.0
e-γ res.	0.3	0.0	0.0	0.0	0.7	0.0
	0.0	-0.3	-2.8	0.0	-0.7	0.0
e-γ scale	0.3	0.0	0.3	0.1	0.0	0.0
	0.0	0.0	-5.1	0.0	-2.3	0.0
γ eff.	1.8	1.7	2.2	2.5	2.3	0.0
	-1.8	-1.7	-2.2	-2.4	-2.2	0.0
γ trigger	0.4	0.4	0.4	0.4	0.4	0.0
	-0.4	-0.4	-0.4	-0.4	-0.4	0.0
e eff.	3.6	0.5	0.9	1.3	0.7	0.0
	-3.6	-0.5	-0.9	-1.3	-0.7	0.0
μ eff.	0.0	0.0	0.3	0.1	0.5	0.0
	0.0	0.0	-0.3	-0.1	-0.6	0.0
JES	100.0	0.0	16.3	6.7	5.0	0.0
	-100.0	0.0	-6.4	-3.1	-4.3	0.0
LRJMR	20.3	7.4	2.7	6.6	0.6	0.0
	-20.3	-7.4	-2.7	-6.6	-0.6	0.0
LRJER	20.3	7.4	3.0	6.1	1.0	0.0
	-20.3	-7.4	-3.0	-6.1	-1.0	0.0
PRW	17.9	7.4	11.9	0.0	1.3	0.0
	-20.3	-3.1	0.0	-9.7	-1.8	0.0
Fitrange	0.0	0.0	0.0	0.0	0.0	33.3
	0.0	0.0	0.0	0.0	0.0	-11.1
Fitform	0.0	0.0	0.0	0.0	0.0	1.1
	0.0	0.0	0.0	0.0	0.0	-1.1
loose photons	0.0	0.0	0.0	0.0	0.0	0.8
	0.0	0.0	0.0	0.0	0.0	-0.8
SpuSi	0.0	0.0	0.0	0.0	0.0	44.4
	0.0	0.0	0.0	0.0	0.0	-44.4

Table A.10.: Summary of all considered relative variations on the expected event yield of the backgrounds in the 1-lepton final state. All entries are given in %.

uncertainty	Non-res.	Mass point m_H [GeV] 500	750	1000	1500	2000	2500	3000
stat	1.6	9.5	1.1	0.8	0.8	1.0	1.2	1.7
	-1.6	-9.5	-1.1	-0.8	-0.8	-1.0	-1.2	-1.7
σ	7.3	0.0	0.0	0.0	0.0	0.0	0.0	0.0
	-8.4	0.0	0.0	0.0	0.0	0.0	0.0	0.0
$\mathcal{BR}$	2.0	2.0	2.0	2.0	2.0	2.0	2.0	2.0
	-2.0	-2.0	-2.0	-2.0	-2.0	-2.0	-2.0	-2.0
$\int \mathcal{L} dt$	3.2	3.2	3.2	3.2	3.2	3.2	3.2	3.2
	-3.2	-3.2	-3.2	-3.2	-3.2	-3.2	-3.2	-3.2
FastSim	7.4	7.4	7.4	7.4	7.4	7.4	7.4	7.4
	-7.4	-7.4	-7.4	-7.4	-7.4	-7.4	-7.4	-7.4
e-γ res.	0.3	3.2	0.4	0.4	0.0	0.0	0.0	0.0
	-0.6	0.0	-1.1	-1.1	-4.4	-11.0	-10.9	-9.5
e-γ scale	0.4	4.2	0.0	0.0	0.0	0.0	0.0	0.0
	-3.8	0.0	-3.1	-2.5	-2.7	-3.3	-3.8	-4.5
γ eff.	2.6	2.5	2.6	2.8	3.1	3.4	3.6	3.7
	-2.6	-2.5	-2.6	-2.8	-3.1	-3.3	-3.5	-3.7
γ trigger	0.0	0.0	0.0	0.0	0.0	0.0	0.0	0.4
	0.0	0.0	0.0	0.0	0.0	0.0	0.0	-0.4
e eff.	0.0	0.0	0.0	0.0	0.0	0.0	0.0	0.0
	0.0	0.0	0.0	0.0	0.0	0.0	0.0	0.0
μ eff.	0.0	0.0	0.0	0.0	0.0	0.0	0.0	0.0
	0.0	0.0	0.0	0.0	0.0	0.0	0.0	0.0
JES	2.2	4.4	1.2	0.7	0.2	0.1	0.2	0.2
	-2.5	-10.6	-1.3	-0.7	-0.3	-0.1	-0.1	-0.1
LRJMR	1.3	8.7	0.7	0.3	1.0	1.3	1.1	0.5
	-1.3	-8.7	-0.7	-0.3	-1.0	-1.3	-1.1	0.0
LRJER	1.3	8.7	0.7	0.3	1.0	1.2	1.2	0.4
	-1.3	-8.7	-0.7	-0.3	-1.0	-1.2	-1.2	0.0
PRW	0.7	8.7	0.7	0.6	0.6	1.2	0.8	0.4
	-1.3	-5.3	-0.1	-0.3	-1.0	-1.3	-1.2	-0.5

Table A.11.: Summary of all considered relative uncertainties on the expected event yield of the signals in the 0-lepton final state. All entries are given in %.

uncertainty	single-Higgs background					Continuum
	ggf	vbf	Wh	Zh	$t\bar{t}h$	background
stat	6.3	7.0	6.4	6.9	4.0	26.7
	-6.8	-7.0	-6.4	-6.9	-4.0	-26.7
σ	8.2	2.1	2.0	4.1	6.8	0.0
	-8.7	-2.1	-2.0	-3.5	-9.9	0.0
$\mathcal{BR}$	1.7	1.7	1.7	1.7	1.7	0.0
	-1.7	-1.7	-1.7	-1.7	-1.7	0.0
$\int \mathcal{L} dt$	3.2	3.2	3.2	3.2	3.2	0.0
	-3.2	-3.2	-3.2	-3.2	-3.2	0.0
FastSim	0.0	0.0	0.0	0.0	0.0	0.0
	0.0	0.0	0.0	0.0	0.0	0.0
e-γ res.	0.0	0.6	0.4	0.9	0.6	0.0
	-4.1	-3.7	-3.4	-1.2	-0.8	0.0
e-γ scale	0.5	0.0	0.0	0.0	0.0	0.0
	-3.2	-7.5	-5.0	-0.9	-2.0	0.0
γ eff.	2.7	2.5	2.6	2.5	2.6	0.0
	-2.6	-2.5	-2.6	-2.5	-2.6	0.0
γ trigger	0.0	0.0	0.0	0.0	0.0	0.0
	0.0	0.0	0.0	0.0	0.0	0.0
e eff.	0.0	0.0	0.0	0.0	0.0	0.0
	0.0	0.0	0.0	0.0	-0.1	0.0
μ eff.	0.0	0.0	0.0	0.0	0.0	0.0
	0.0	0.0	0.0	0.0	-0.1	0.0
JES	0.5	3.5	1.3	2.1	2.3	0.0
	-0.3	-1.8	-0.7	-1.1	-1.8	0.0
LRJMR	1.7	6.9	2.3	0.8	1.6	0.0
	-1.7	-6.9	-2.3	-0.8	-1.6	0.0
LRJER	2.2	7.1	2.3	0.8	1.7	0.0
	-2.2	-7.1	-2.3	-0.8	-1.7	0.0
PRW	0.4	3.8	2.8	0.9	1.0	0.0
	-2.2	-7.1	-2.3	-0.8	-1.7	0.0
Fitrange	0.0	0.0	0.0	0.0	0.0	34.7
	0.0	0.0	0.0	0.0	0.0	-34.7
Fitform	0.0	0.0	0.0	0.0	0.0	1.7
	0.0	0.0	0.0	0.0	0.0	-1.7
Mass window	0.0	0.0	0.0	0.0	0.0	5.1
	0.0	0.0	0.0	0.0	0.0	-5.1
SpuSi	0.0	0.0	0.0	0.0	0.0	33.5
	0.0	0.0	0.0	0.0	0.0	-33.5

Table A.12.: Summary of all considered relative uncertainties on the expected event yield of the backgrounds in the 0-lepton final state. All entries are given in %.

A.5. Limits

In this section, tables summarizing the upper limits set with statistical uncertainties only (Tab. A.13) and with systematic uncertainties included (Tab. A.14) are given. Here, the 1-lepton and 0-lepton final states are shown individually and combined.

mass	non-res.	500 GeV	750 GeV	1000 GeV	1500 GeV	2000 GeV	2500 GeV	3000 GeV
Median	26.48	53.06	4.66	3.01	3.02	3.83	5.60	9.75
Observed	23.21	46.48	4.08	2.64	2.65	3.36	4.91	8.57
$+2\sigma$	68.77	138.94	12.08	7.82	7.83	9.94	14.53	25.38
$+1\sigma$	41.21	82.79	7.25	4.69	4.69	5.96	8.72	15.22
-1σ	19.08	38.23	3.35	2.17	2.18	2.76	4.03	7.03
-2σ	14.21	28.48	2.50	1.62	1.62	2.06	3.00	5.24

(a) 1-lepton final state.

mass	non-res.	500 GeV	750 GeV	1000 GeV	1500 GeV	2000 GeV	2500 GeV	3000 GeV
Median	27.16	251.22	3.27	2.19	2.07	3.09	5.58	9.44
Observed	48.37	450.25	5.83	3.90	3.69	5.50	9.93	16.80
$+2\sigma$	59.24	566.71	7.14	4.78	4.51	6.73	12.16	20.58
$+1\sigma$	40.11	375.23	4.83	3.24	3.06	4.56	8.23	13.94
-1σ	19.57	181.02	2.36	1.58	1.49	2.23	4.02	6.80
-2σ	14.58	134.84	1.76	1.18	1.11	1.66	2.99	5.07

(b) 0-lepton final state.

mass	non-res.	500 GeV	750 GeV	1000 GeV	1500 GeV	2000 GeV	2500 GeV	3000 GeV
Median	16.30	49.99	2.31	1.53	1.47	2.06	3.40	5.83
Observed	27.10	58.57	3.88	2.56	2.48	3.46	5.65	9.72
$+2\sigma$	37.10	126.08	5.16	3.41	3.29	4.64	7.72	13.23
$+1\sigma$	24.26	77.00	3.42	2.26	2.18	3.06	5.05	8.67
-1σ	11.75	36.02	1.66	1.10	1.06	1.49	2.45	4.20
-2σ	8.75	26.83	1.24	0.82	0.79	1.11	1.82	3.13

(c) Combined.

Table A.13.: Limits on $\sigma_{gg\to H} \times \mathcal{BR}_{H\to hh}$ and $\sigma_{gg\to hh}$ in pb for the different mass points in the 1-lepton and 0-lepton final states and the combination of these with statistical uncertainties only.

mass	non-res.	500 GeV	750 GeV	1000 GeV	1500 GeV	2000 GeV	2500 GeV	3000 GeV
Median	26.84	55.22	4.66	3.01	3.01	3.86	5.67	9.90
Observed	23.67	48.62	4.11	2.65	2.66	3.41	5.01	8.71
$+2\sigma$	73.09	162.24	12.37	7.95	7.99	10.76	16.16	27.74
$+1\sigma$	42.41	89.38	7.30	4.71	4.72	6.12	9.06	15.70
-1σ	19.34	39.79	3.35	2.17	2.17	2.78	4.09	7.13
-2σ	14.41	29.64	2.50	1.62	1.62	2.07	3.04	5.31

(a) 1-lepton final state.

mass	non-res.	500 GeV	750 GeV	1000 GeV	1500 GeV	2000 GeV	2500 GeV	3000 GeV
Median	27.73	289.03	3.44	2.32	2.21	3.33	6.00	10.65
Observed	48.38	512.68	5.94	4.02	3.83	5.83	10.50	18.56
$+2\sigma$	62.13	706.05	7.49	5.06	4.84	7.63	13.75	24.11
$+1\sigma$	41.19	442.76	5.06	3.42	3.26	4.97	8.96	15.82
-1σ	19.98	208.26	2.48	1.67	1.59	2.40	4.33	7.67
-2σ	14.89	155.13	1.84	1.25	1.19	1.79	3.22	5.71

(b) 0-lepton final state.

mass	non-res.	500 GeV	750 GeV	1000 GeV	1500 GeV	2000 GeV	2500 GeV	3000 GeV
Median	17.19	54.64	2.45	1.63	1.58	2.24	3.70	6.48
Observed	28.70	61.01	4.09	2.71	2.64	3.78	6.21	10.85
$+2\sigma$	40.13	151.85	5.48	3.64	3.54	5.32	8.91	15.48
$+1\sigma$	25.73	87.16	3.62	2.41	2.34	3.37	5.58	9.75
-1σ	12.39	39.37	1.77	1.18	1.14	1.62	2.66	4.67
-2σ	9.23	29.33	1.32	0.88	0.85	1.20	1.98	3.48

(c) Combined.

Table A.14.: Limits on $\sigma_{gg\to H} \times \mathcal{BR}_{H\to hh}$ and $\sigma_{gg\to hh}$ in pb for the different mass points in the 1-lepton and 0-lepton final states and the combination of these with statistical and systematic uncertainties included.

B. Additional Graphics

B.1. Overlap Removal

In this section, the distributions of the electron-jet system and the muon-jet system are compared for further signal mass points and non-resonant di-Higgs production.

Regarding the other resonant mass points, it is clear that the need but also the efficiency of the OLR modifications to remove large-R jets caused by electrons (see Sec. 4.4) increases with increasing masses. While for non-resonant production (Figures B.1 to B.3) and the $m_H = 750\,\text{GeV}$ mass point (discussed in Sec. 4.4) the differences between electron-jet systems and muon-jet system with the lepton being inside the large-R jet occur with and without the OLR modifications. Going to the $m_H = 1500\,\text{GeV}$ mass point (Figures B.4 to B.6) and the $m_H = 3000\,\text{GeV}$ mass point (Figures B.7 to B.9), the differences between electron-jet systems and muon-jet systems become larger for very low masses and a high p_T ratio but agreement with the modified OLR applied is significantly better (see Fig. B.9).

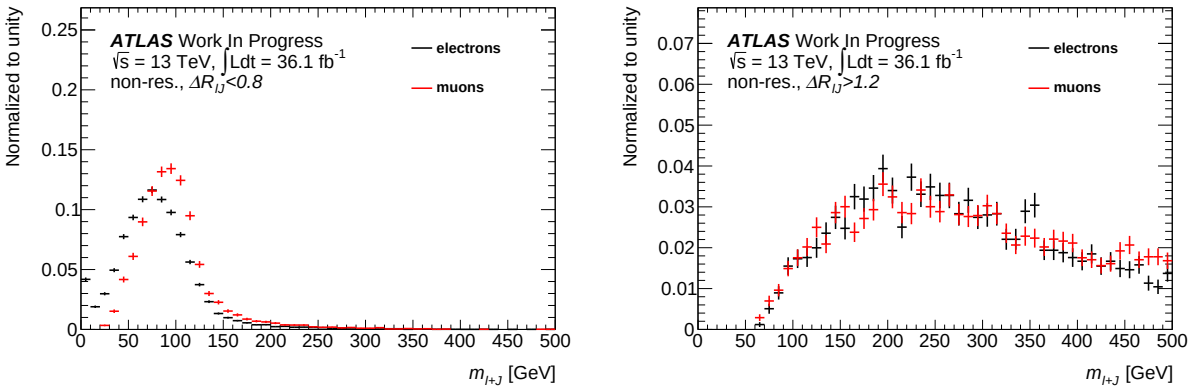

Figure B.1.: Mass of the lepton-jet whereby the lepton is (a) inside and (b) outside the large-R jet for the non-resonant production mode.

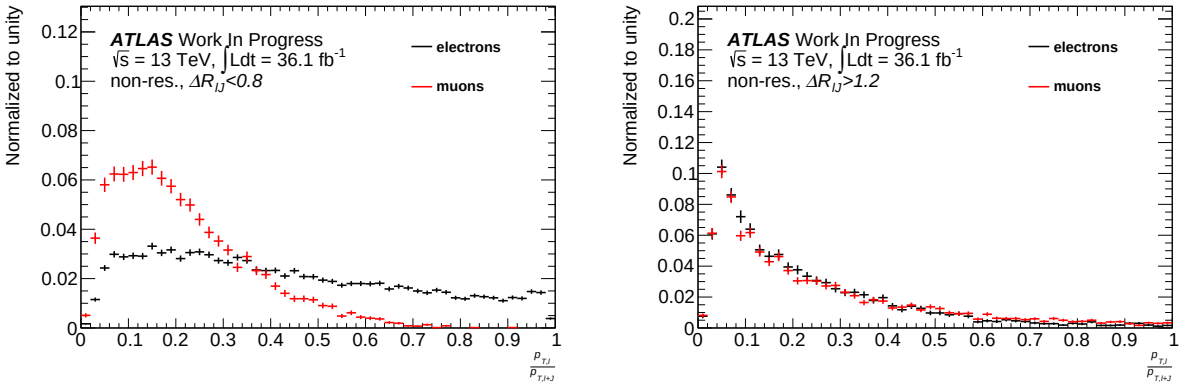

(a) *(b)*

Figure B.2.: Ratio of the transverse momentum of the lepton and the lepton-jet whereby the lepton is (a) inside and (b) outside the large-R jet for the non-resonant production mode.

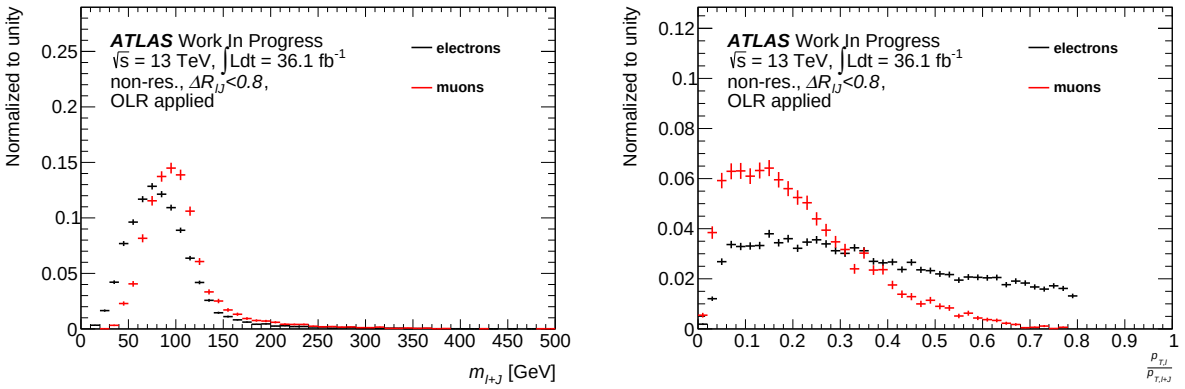

(a) *(b)*

Figure B.3.: Distributions of the (a) mass of the lepton-jet system and (b) the p_T ratio between lepton and lepton-jet for the non-resonant production mode after the OLR was applied.

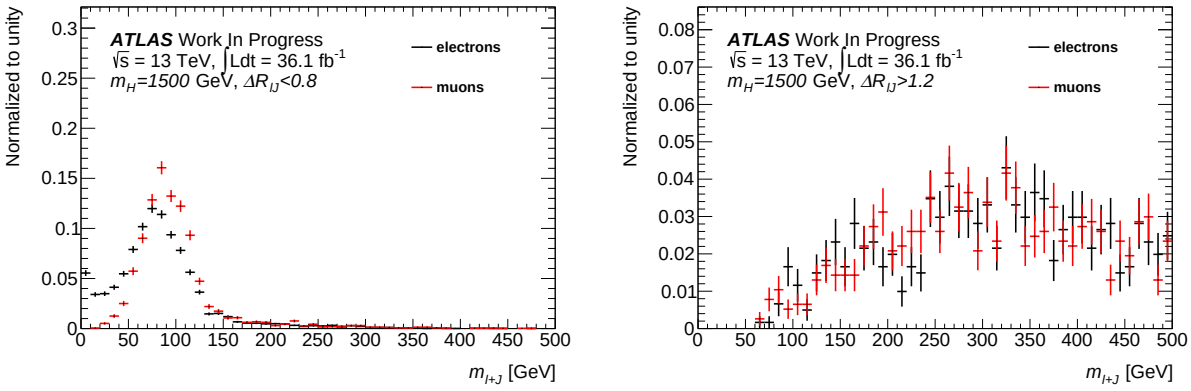

(a) ***(b)***

Figure B.4.: Mass of the lepton-jet whereby the lepton is (a) inside and (b) outside the large-R jet for the $m_H = 1500\,\text{GeV}$ mass point.

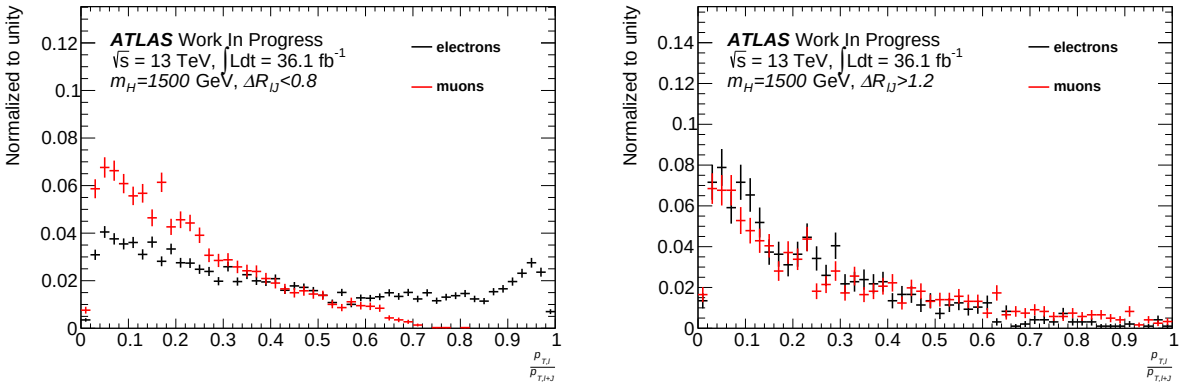

(a) ***(b)***

Figure B.5.: Ratio of the transverse momentum of the lepton and the lepton-jet whereby the lepton is (a) inside and (b) outside the large-R jet for the $m_H = 1500\,\text{GeV}$ mass point.

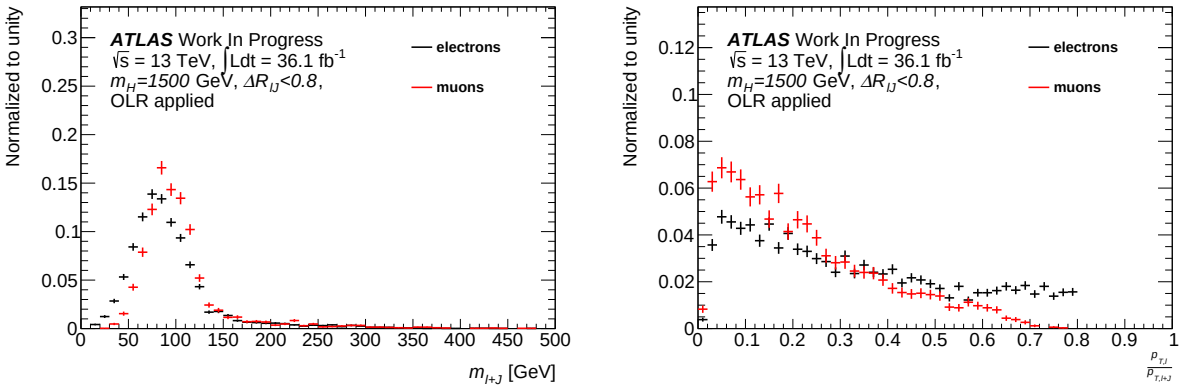

(a) *(b)*

Figure B.6.: Distributions of the (a) mass of the lepton-jet system and (b) the p_T ratio between lepton and lepton-jet for the $m_H = 1500\,\text{GeV}$ mass point after the OLR was applied.

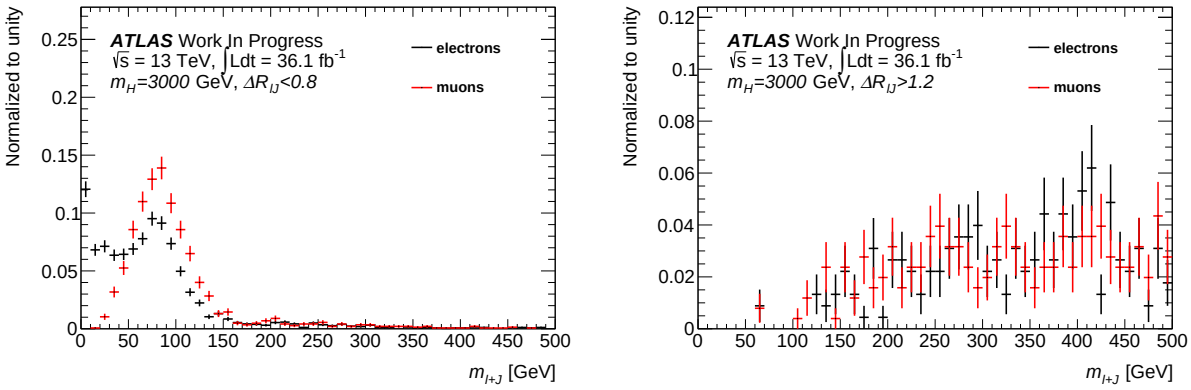

(a) *(b)*

Figure B.7.: Mass of the lepton-jet whereby the lepton is (a) inside and (b) outside the large-R jet for the $m_H = 3000\,\text{GeV}$ mass point.

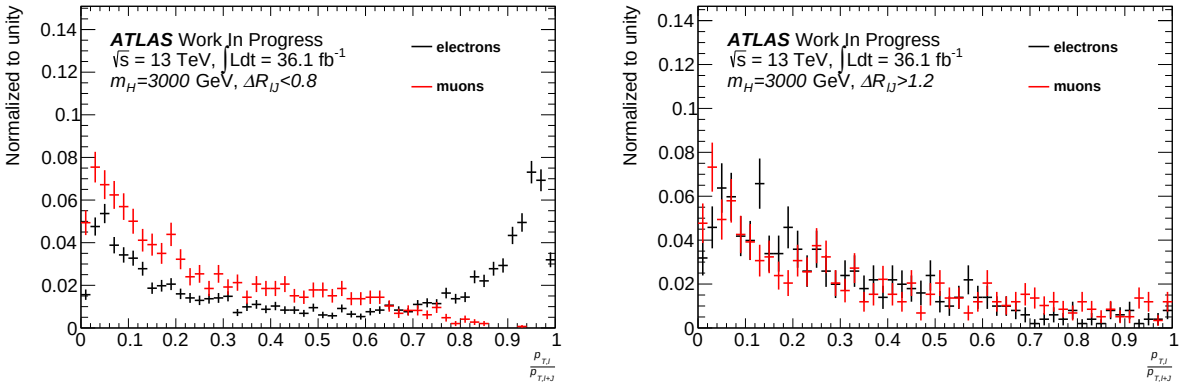

(a) *(b)*

Figure B.8.: Ratio of the transverse momentum of the lepton and the lepton-jet whereby the lepton is (a) inside and (b) outside the large-R jet for the $m_H = 3000\,\text{GeV}$ mass point.

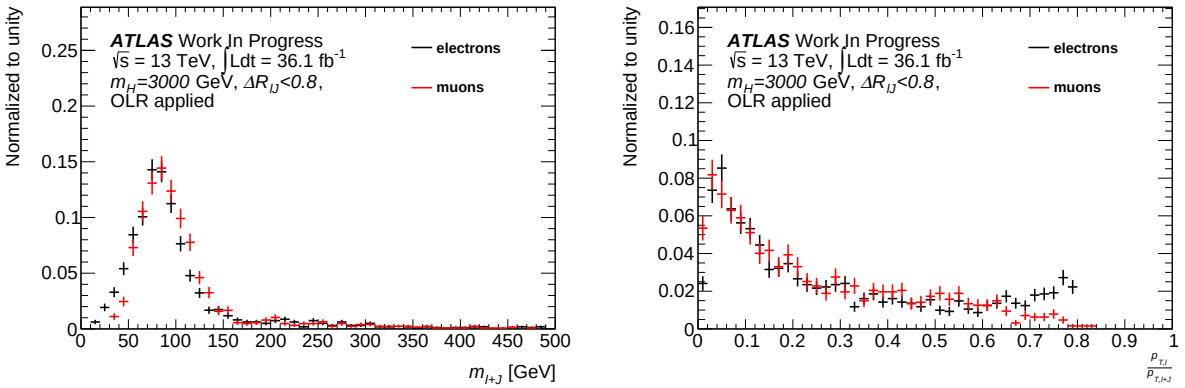

(a) *(b)*

Figure B.9.: Distributions of the (a) mass of the lepton-jet system and (b) the p_T ratio between lepton and lepton-jet for the $m_H = 3000\,\text{GeV}$ mass point after the OLR was applied.

B.2. Separation Power

In this section, the distributions of the in Sec. 4.7 variables are compared for the $m_H = 750\,\text{GeV}$ mass point and the dominating backgrounds (Wh, Zh and $t\bar{t}h$ and the continuum background) to have an estimate on the separation power after preselection.

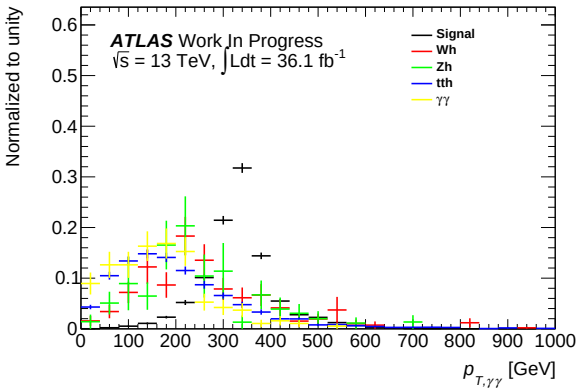

Figure B.10.: Comparison between the $m_H = 750\,\text{GeV}$ mass point and the dominating backgrounds of $p_{T,\gamma\gamma}$.

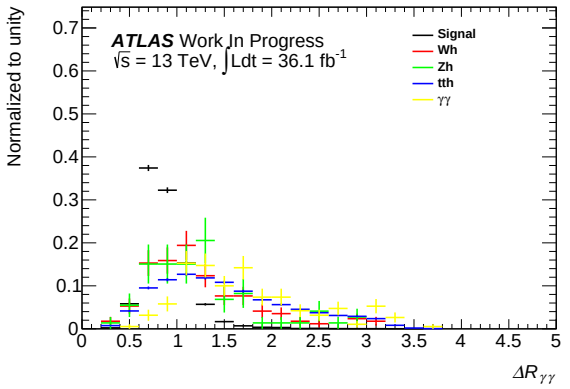

Figure B.11.: Comparison between the $m_H = 750\,\text{GeV}$ mass point and the dominating backgrounds of $\Delta R_{\gamma\gamma}$.

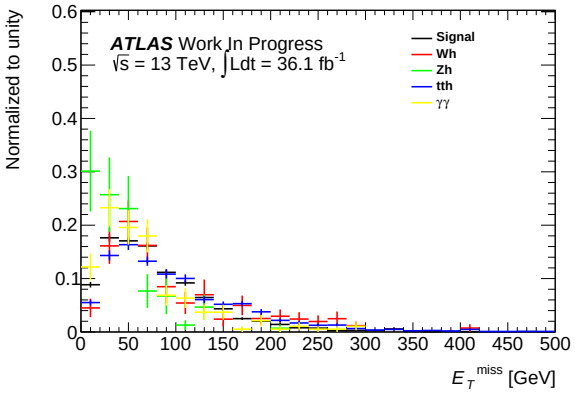

Figure B.12.: Comparison between the $m_H = 750\,\text{GeV}$ signal sample and the dominating backgrounds of E_T^{miss}.

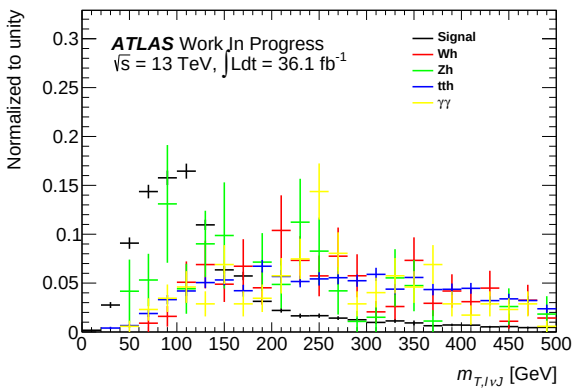

Figure B.13.: Comparison between the $m_H = 750\,\text{GeV}$ signal sample and the dominating backgrounds of $m_{T,\ell\nu J}$.

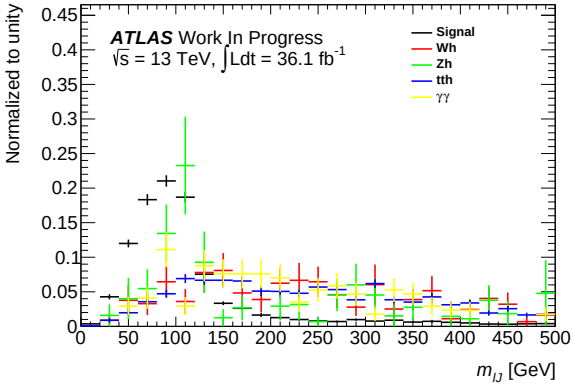

Figure B.14.: Comparison between the $m_H = 750\,\text{GeV}$ signal sample and the dominating backgrounds of $m_{\ell J}$.

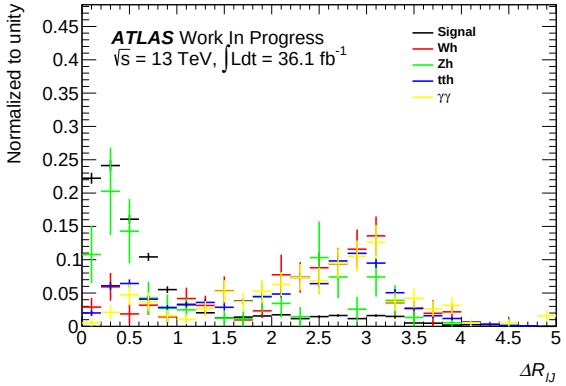

Figure B.15.: Comparison between the $m_H = 750\,\text{GeV}$ signal sample and the dominating backgrounds of $\Delta R_{\ell J}$.

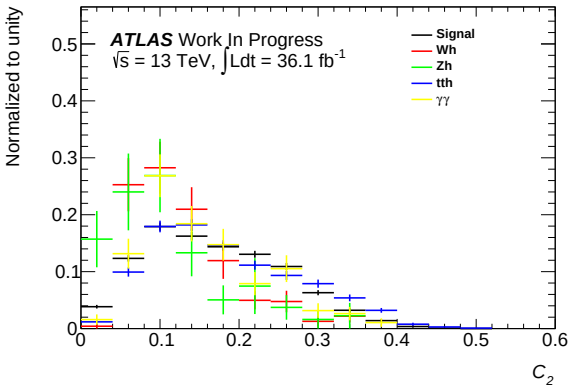

Figure B.16.: Comparison between the $m_H = 750\,\text{GeV}$ signal sample and the dominating backgrounds of C_2.

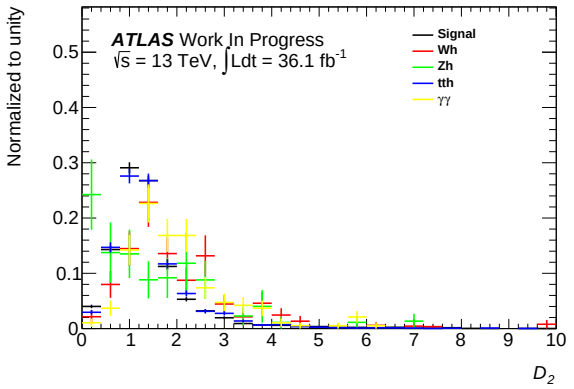

Figure B.17.: Comparison between the $m_H = 750\,\text{GeV}$ signal sample and the dominating backgrounds of D_2.

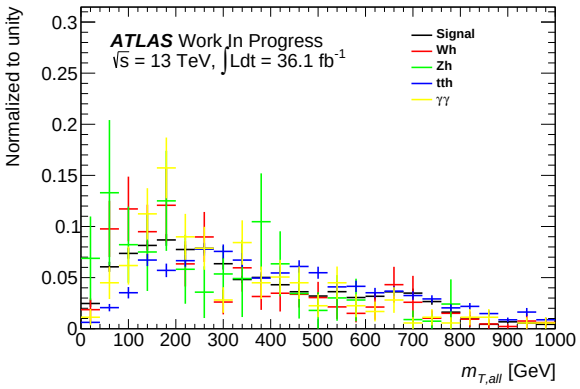

Figure B.18.: Comparison between the $m_H = 750\,\text{GeV}$ signal sample and the dominating backgrounds of the transverse mass of $m_{T,all}$.

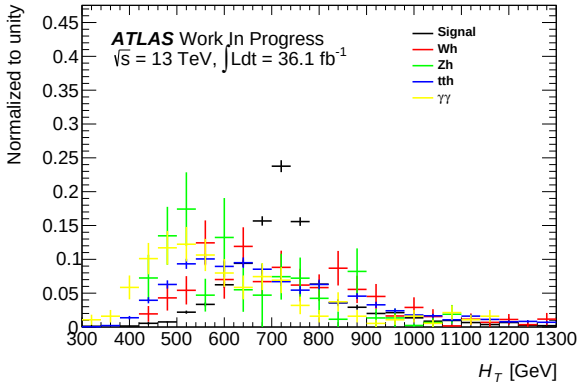

Figure B.19.: Comparison between the $m_H = 750\,\text{GeV}$ signal sample and the dominating backgrounds of H_T.

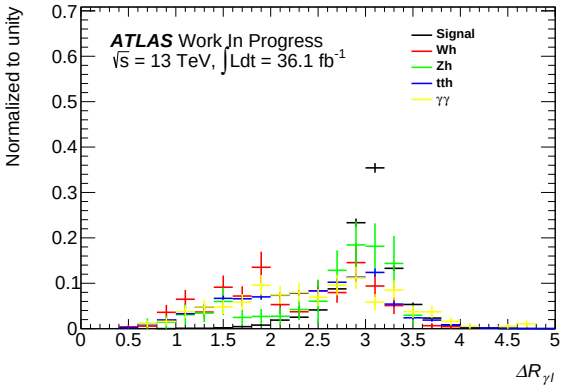

Figure B.20.: Comparison between the $m_H = 750\,\text{GeV}$ signal sample and the dominating backgrounds of $\Delta R_{\gamma\ell}$.

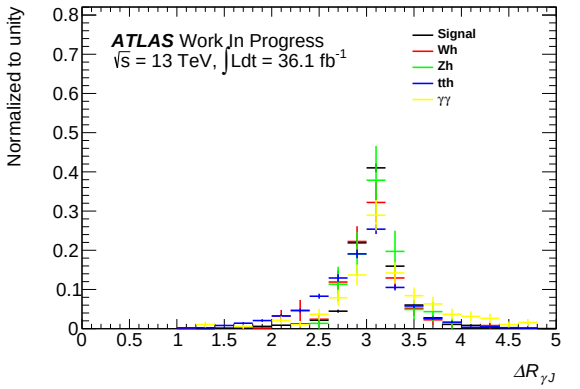

Figure B.21.: Comparison between the $m_H = 750\,\text{GeV}$ signal sample and the dominating backgrounds of $\Delta R_{\gamma J}$.

B.3. Consistency Check between Loose and Tight Photons

In this section, the consistency checks between the loose and tight photon criteria are presented. These checks are passed by all variables within the statistical uncertainties.

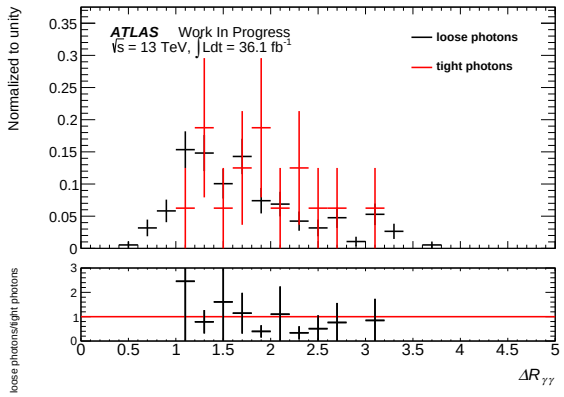

Figure B.22.: Consistency check between loose and tight photon criteria regarding $\Delta R_{\gamma\gamma}$.

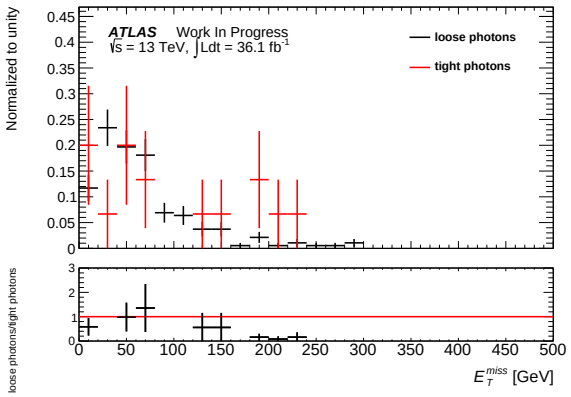

Figure B.23.: Consistency check between loose and tight photon criteria regarding E_T^{miss}.

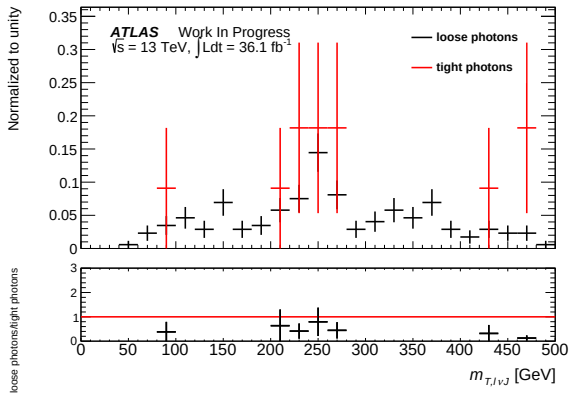

Figure B.24.: Consistency check between loose and tight photon criteria regarding $m_{T,\ell\nu J}$.

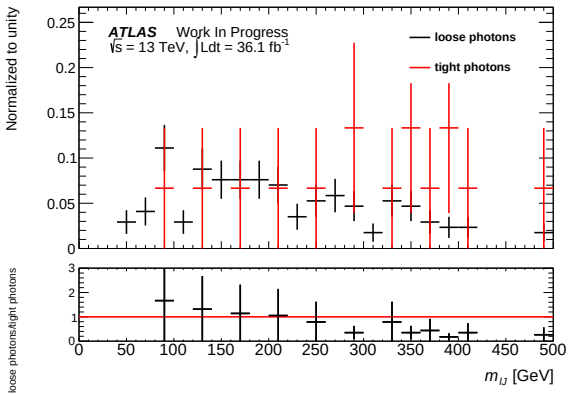

Figure B.25.: Consistency check between loose and tight photon criteria regarding $m_{\ell J}$.

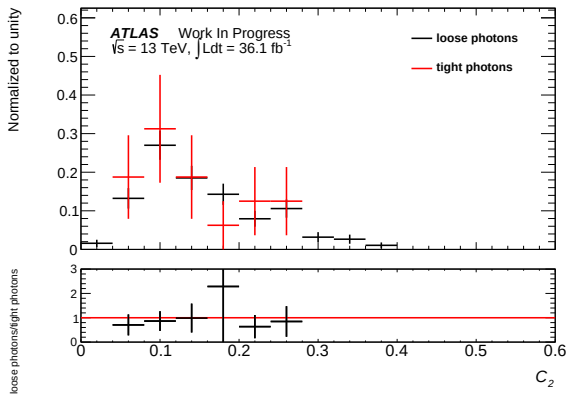

Figure B.26.: Consistency check between loose and tight photon criteria regarding C_2.

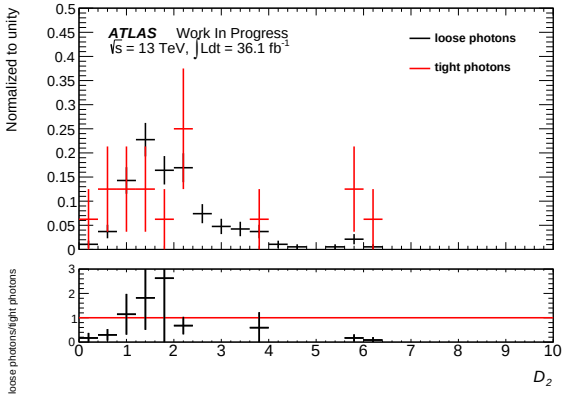

Figure B.27.: Consistency check between loose and tight photon criteria regarding $D2$.

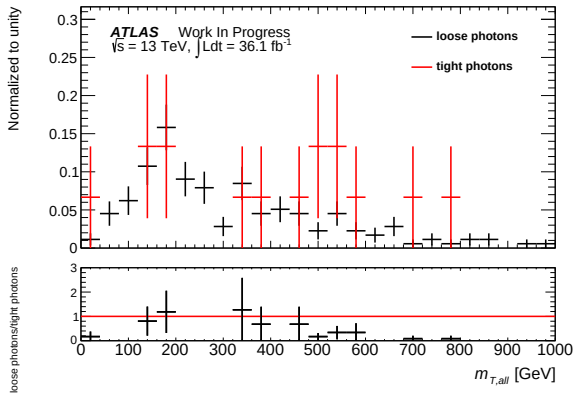

Figure B.28.: Consistency check between loose and tight photon criteria regarding $m_{T,\mathrm{all}}$.

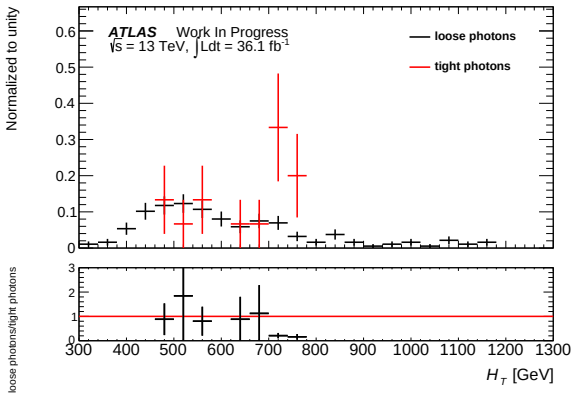

Figure B.29.: Consistency check between loose and tight photon criteria regarding H_T.

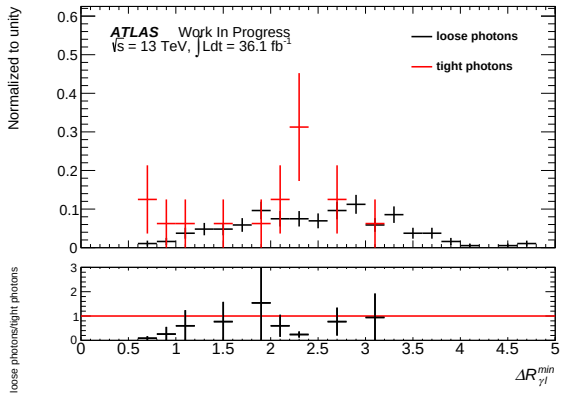

Figure B.30.: Consistency check between loose and tight photon criteria regarding $\Delta R_{\gamma\ell}$.

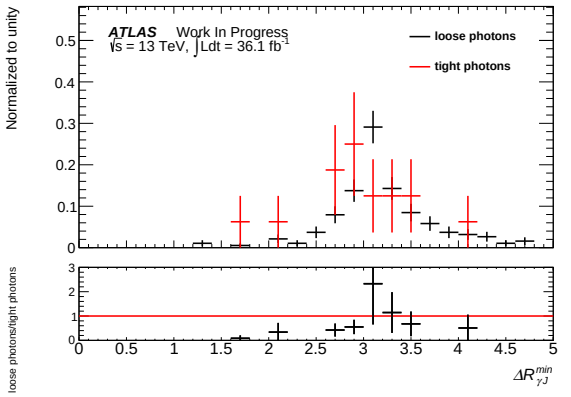

Figure B.31.: Consistency check between loose and tight photon criteria regarding $\Delta R_{\gamma J}$.

B.4. Consistency Check between Upper and Lower Sideband Events

In this section, the consistency checks between the upper and lower sidebands are presented. These checks are all passed within the statistical uncertainties.

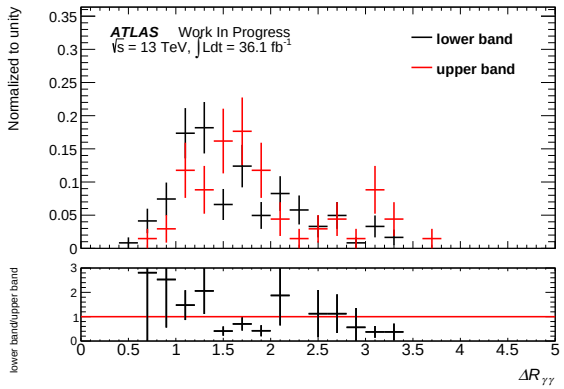

Figure B.32.: Consistency check between the upper and lower $m_{\gamma\gamma}$ sidebands regarding $\Delta R_{\gamma\gamma}$.

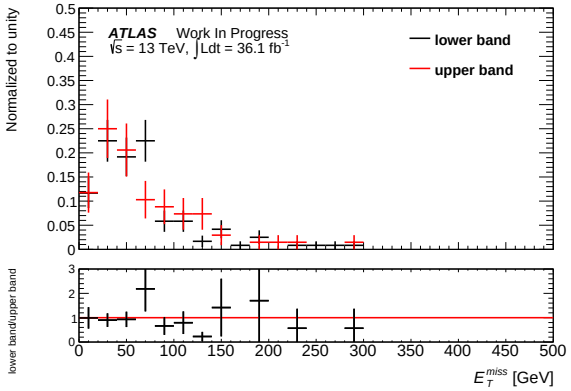

Figure B.33.: Consistency check between the upper and lower $m_{\gamma\gamma}$ sidebands regarding E_T^{miss}.

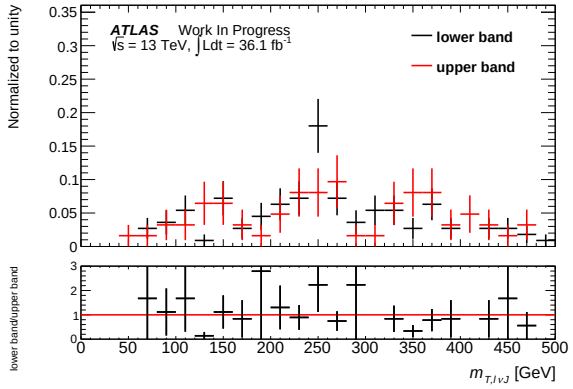

Figure B.34.: Consistency check between the upper and lower $m_{\gamma\gamma}$ sidebands regarding $m_{T,\ell\nu J}$.

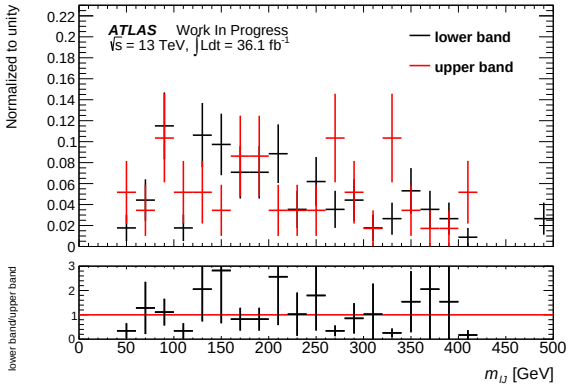

Figure B.35.: Consistency check between the upper and lower $m_{\gamma\gamma}$ sidebands regarding $m_{\ell J}$.

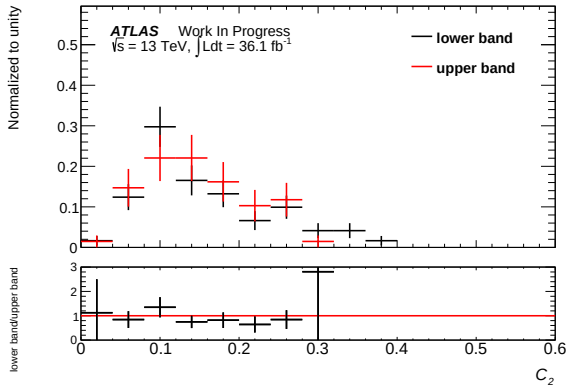

Figure B.36.: Consistency check between the upper and lower $m_{\gamma\gamma}$ sidebands regarding C_2.

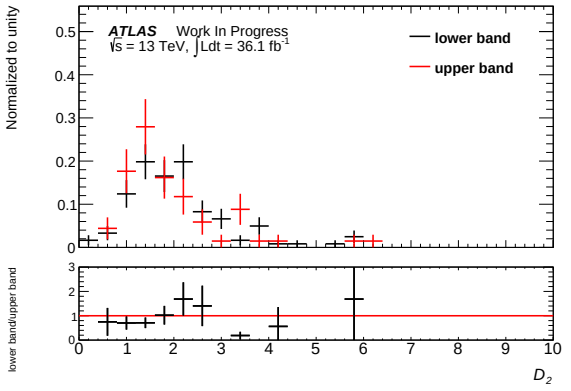

Figure B.37.: Consistency check between the upper and lower $m_{\gamma\gamma}$ sidebands regarding $D2$.

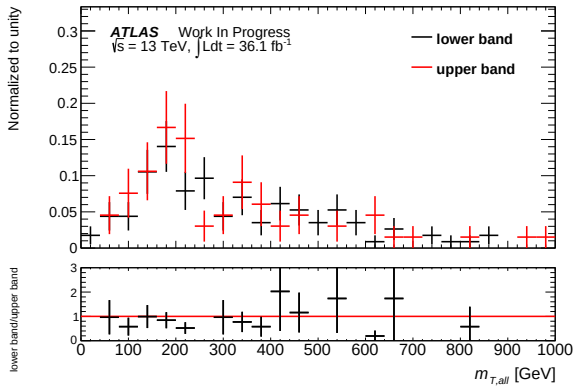

Figure B.38.: Consistency check between the upper and lower $m_{\gamma\gamma}$ sidebands regarding $m_{T,\mathrm{all}}$.

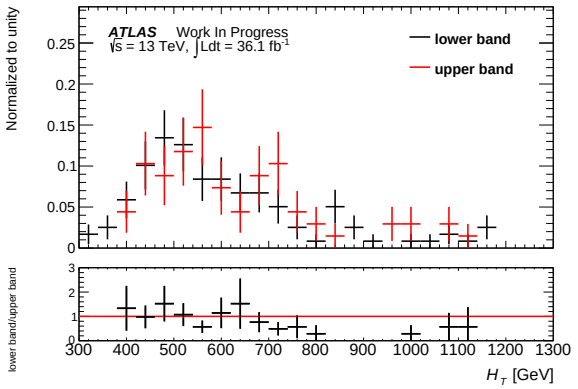

Figure B.39.: Consistency check between the upper and lower $m_{\gamma\gamma}$ sidebands regarding H_T.

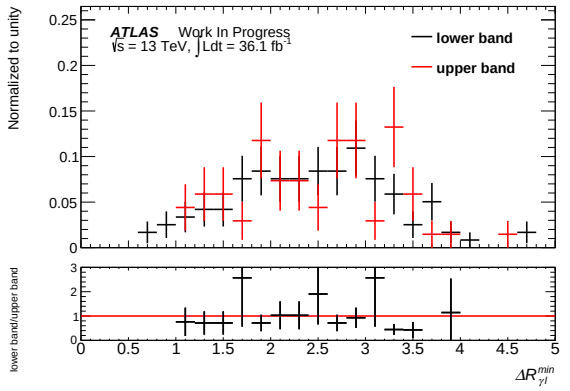

Figure B.40.: Consistency check between the upper and lower $m_{\gamma\gamma}$ sidebands regarding $\Delta R_{\gamma\ell}$.

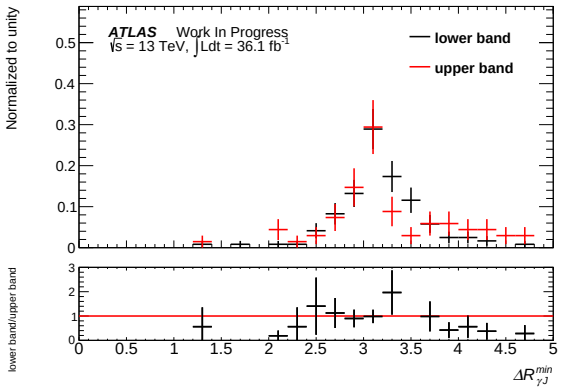

Figure B.41.: Consistency check between the upper and lower $m_{\gamma\gamma}$ sidebands regarding $\Delta R_{\gamma J}$.

B.5. Optimisation

In this section, the significance distributions are shown for the variables yielding the highest significances in both optimisation iterations. The corresponding variable distributions for the $m_H = 750\,\text{GeV}$ signal mass point and the dominating backgrounds are given with the cut value indicated by a pink line.

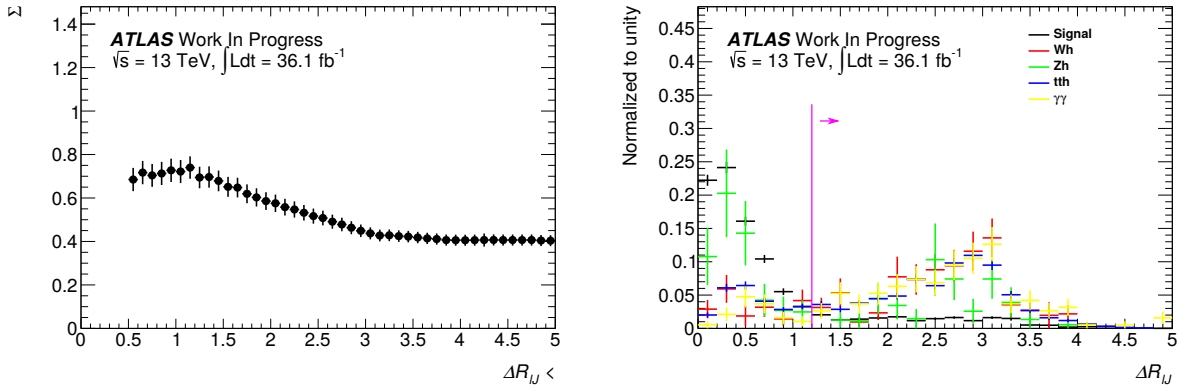

(a) *(b)*

Figure B.42.: Significance in (a) and distributions of the $m_H = 750\,\text{GeV}$ mass point and the main backgrounds in (b) for $\Delta R_{\ell J}$ as one of the best separation variables in the first optimisation iteration. The pink line gives the best cut value with the arrow indicating which part would be cut away.

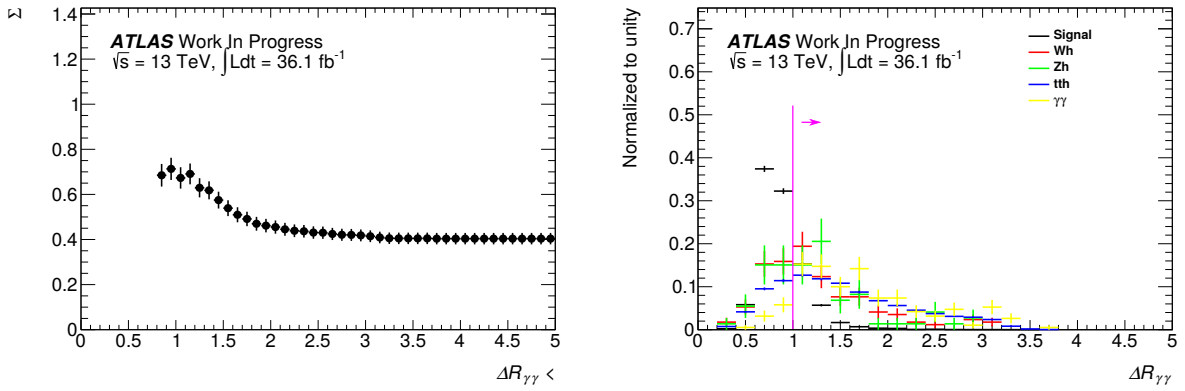

(a) *(b)*

Figure B.43.: Significance in (a) and distributions of the $m_H = 750\,\text{GeV}$ mass point and the main backgrounds in (b) for $\Delta R_{\gamma\gamma}$ as one of the best separation variables in the first optimisation iteration. The pink line gives the best cut value with the arrow indicating which part would be cut away.

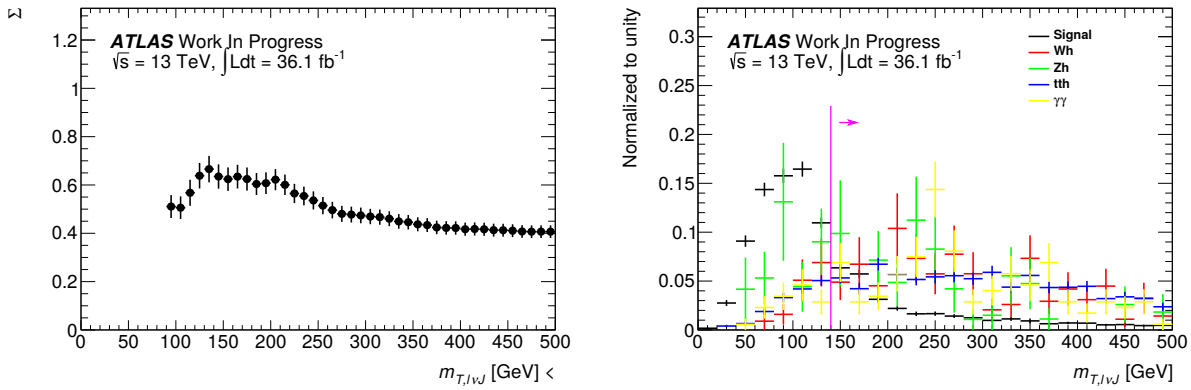

(a) *(b)*

Figure B.44.: Significance in (a) and distributions of the $m_H = 750\,\text{GeV}$ mass point and the main backgrounds in (b) for $m_{T,\ell\nu J}$ as one of the best separation variables in the first optimisation iteration. The pink line gives the best cut value with the arrow indicating which part would be cut away.

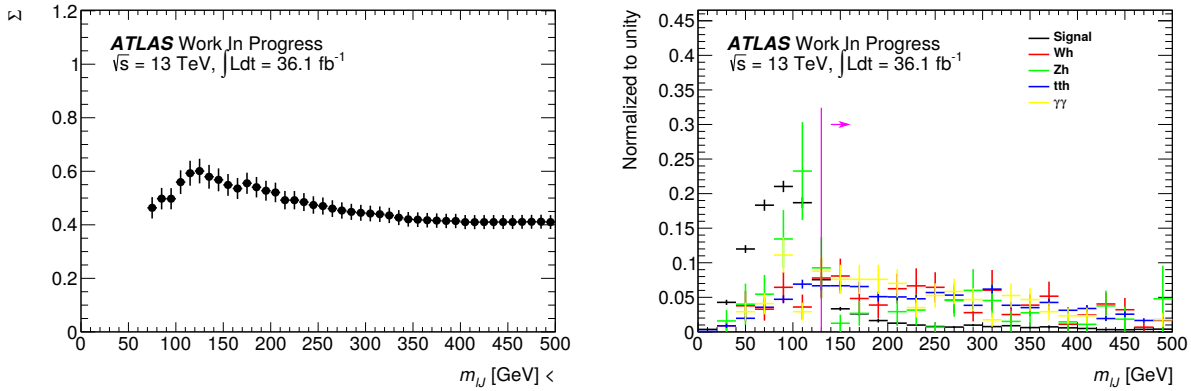

(a) *(b)*

Figure B.45.: Significance in (a) and distributions of the $m_H = 750\,\text{GeV}$ mass point and the main backgrounds in (b) for $m_{\ell J}$ as one of the best separation variables in the first optimisation iteration. The pink line gives the best cut value with the arrow indicating which part would be cut away.

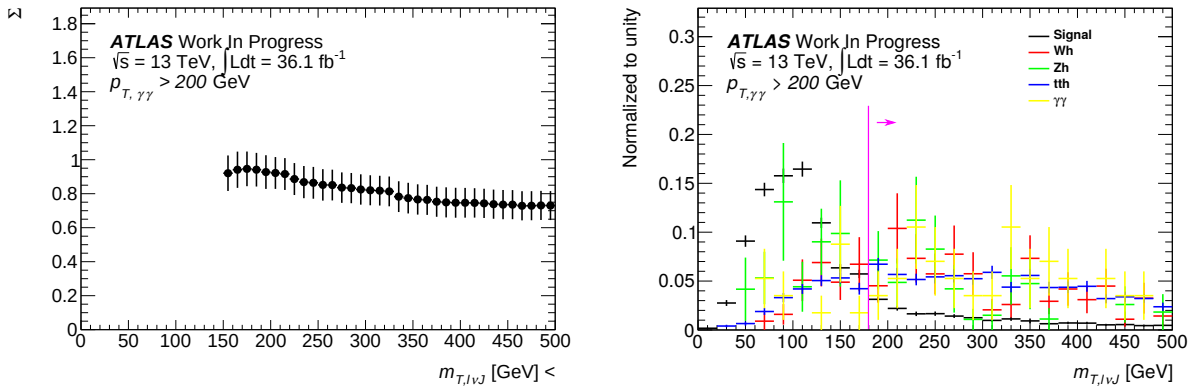

(a) *(b)*

Figure B.46.: Significance in (a) and distributions of the $m_H = 750\,\text{GeV}$ mass point and the main backgrounds in (b) for $m_{T,\ell\nu J}$ as one of the best separation variables in the second optimisation iteration. The pink line gives the best cut value with the arrow indicating which part would be cut away.

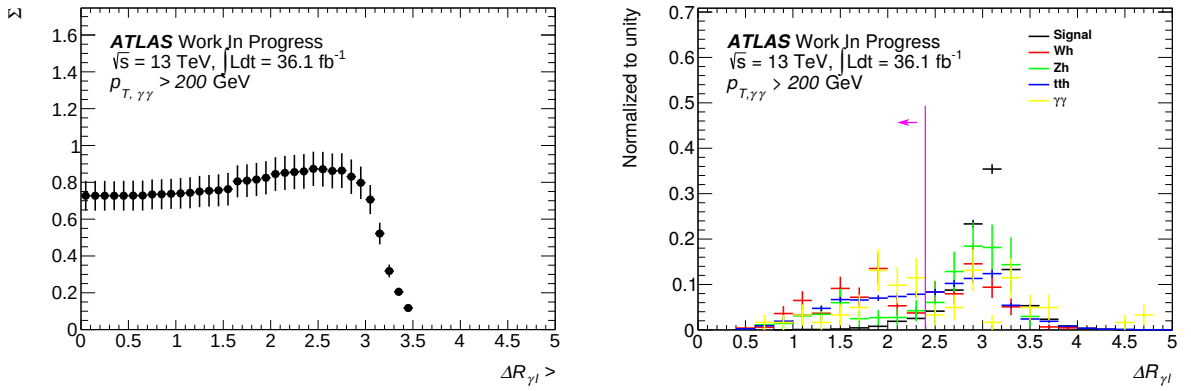

(a) *(b)*

Figure B.47.: Significance in (a) and distributions of the $m_H = 750\,\text{GeV}$ mass point and the main backgrounds in (b) for $\Delta R_{\gamma\ell}^{\text{min}}$ as one of the best separation variables in the second optimisation iteration. The pink line gives the best cut value with the arrow indicating which part would be cut away.

Bibliography

[1] G. Guralnik, C. Hagen, T. Kibble, *Global Conservation Laws and Massless Particles*, Phys. Rev. Lett. **13** (1964)

[2] F. Englert, R. Brout, *Broken Symmetry and the Mass of Gauge Vector Mesons*, Phys. Rev. Lett. **13** (1964)

[3] P. Higgs, *Broken Symmetries and the Masses of Gauge Bosons*, Phys. Rev. Lett. **13** (1964)

[4] ATLAS Collaboration, *Observation of a new particle in the search for the Standard Model Higgs boson with the ATLAS detector at the LHC*, Phys. Lett. **B716** (2012)

[5] CMS Collaboration, *Observation of a new boson at a mass of 125 GeV with the CMS experiment at the LHC*, Phys. Lett. **B716** (2012)

[6] G. Hinshaw, et al. (WMAP), *Nine-Year Wilkinson Microwave Anisotropy Probe (WMAP) Observations: Cosmological Parameter Results*, Astrophys. J. Suppl. **208** (2013)

[7] M. Kobayashi, T. Maskawa, *CP Violation in the Renormalizable Theory of Weak Interaction*, Prog. Theor. Phys. **49** (1973)

[8] M. Trodden, *Electroweak baryogenesis: A Brief review*, in *Moriond* (1998), arXiv:hep-ph/9805252

[9] Yu. A. Golfand, E. P. Likhtman, *Extension of the Algebra of Poincare Group Generators and Violation of p Invariance*, JETP Lett. **13** (1971)

[10] J. Wess, B. Zumino, *Supergauge Transformations in Four-Dimensions*, Nucl. Phys. **B70** (1974)

[11] J. Wess, B. Zumino, *Supergauge Invariant Extension of Quantum Electrodynamics*, Nucl. Phys. **B78** (1974)

[12] S. Ferrara, B. Zumino, *Supergauge Invariant Yang-Mills Theories*, Nucl. Phys. **B79** (1974)

[13] A. Salam, J. A. Strathdee, *Supersymmetry and Nonabelian Gauges*, Phys. Lett. **51B** (1974)

[14] P. Fayet, *Supergauge Invariant Extension of the Higgs Mechanism and a Model for the electron and Its Neutrino*, Nucl. Phys. **B90** (1975)

[15] P. Fayet, *Supersymmetry and Weak, Electromagnetic and Strong Interactions*, Phys. Lett. **64B** (1976)

[16] P. Fayet, *Spontaneously Broken Supersymmetric Theories of Weak, Electromagnetic and Strong Interactions*, Phys. Lett. **69B** (1977)

[17] P. Fayet, *Relations Between the Masses of the Superpartners of Leptons and Quarks, the Goldstino Couplings and the Neutral Currents*, Phys. Lett. **84B** (1979)

[18] K. Inoue, et al., *Aspects of Grand Unified Models with Softly Broken Supersymmetry*, Prog. Theor. Phys. **68** (1982), [Erratum: Prog. Theor. Phys.70 (1983)]

[19] T. D. Lee, *A Theory of Spontaneous T Violation*, Phys. Rev. **D8** (1973)

[20] M. Peskin, D. Schroeder, *An Introduction To Quantum Field Theory*, Westview Press (1995)

[21] M. Thomson, *Modern Particle Physics*, Cambridge University Press (2013)

[22] C. Patrignani, et al. (Particle Data Group), *The Review of Particle Physics*, Chin. Phys. **C40** (2016)

[23] A. Djouadi, *The Anatomy of electro-weak symmetry breaking. I: The Higgs boson in the standard model*, Phys. Rept. **457** (2008)

[24] P. A. M. Dirac, *Quantum theory of emission and absorption of radiation*, Proc. Roy. Soc. Lond. **A114** (1927)

[25] W. Heisenberg, W. Pauli, *On Quantum Field Theory. (In German)*, Z. Phys. **56** (1929)

[26] S. Glashow, *Partial Symmetries of Weak Interactions*, Nucl.Phys. **22** (1961)

[27] A. Salam, J. C. Ward, *Electromagnetic and weak interactions*, Phys.Lett. **13** (1964)

[28] S. Weinberg, *A Model of Leptons*, Phys. Rev. Lett. **19** (1967)

[29] M. Gell-Mann, *A Schematic Model of Baryons and Mesons*, Phys. Lett. **8** (1964)

[30] H. Fritzsch, M. Gell-Mann, H. Leutwyler, *Advantages of the Color Octet Gluon Picture*, Phys. Lett. **47B** (1973)

[31] G. Arnison, et al. (UA1), *Experimental Observation of Isolated Large Transverse Energy Electrons with Associated Missing Energy at* $\sqrt{s} = 540$ *GeV*, Phys.Lett. **B122** (1983)

[32] G. Arnison, et al. (UA1), *Experimental Observation of Lepton Pairs of Invariant Mass Around 95 GeV/*c^2 *at the CERN SPS Collider*, Phys.Lett. **B126** (1983)

[33] J. Goldstone, *Field theories with « Superconductor » solutions*, Il Nuovo Cimento **19** (1961)

[34] J. Goldstone, A. Salam, S. Weinberg, *Broken Symmetries*, Phys. Rev. **127** (1962)

[35] ATLAS Collaboration, CMS Collaboration, *Combined Measurement of the Higgs Boson Mass in pp Collisions at* $\sqrt{s} = 7$ *and 8 TeV with the ATLAS and CMS Experiments*, Phys. Rev. Lett. **114** (2015)

[36] M. J. G. Veltman, *The Infrared - Ultraviolet Connection*, Acta Phys. Polon. **B12** (1981)

[37] R. K. Kaul, P. Majumdar, *Cancellation of Quadratically Divergent Mass Corrections in Globally Supersymmetric Spontaneously Broken Gauge Theories*, Nucl. Phys. **B199** (1982)

[38] S. P. Martin, *A Supersymmetry primer*, Adv.Ser.Direct.High Energy Phys. **21** (2010)

[39] A. Djouadi, *The Anatomy of electro-weak symmetry breaking. II. The Higgs bosons in the minimal supersymmetric model*, Phys. Rept. **459** (2008)

[40] G. R. Farrar, P. Fayet, *Phenomenology of the Production, Decay, and Detection of New Hadronic States Associated with Supersymmetry*, Phys. Lett. **76B** (1978)

[41] L. Girardello, M. T. Grisaru, *Soft Breaking of Supersymmetry*, Nucl. Phys. **B194** (1982)

[42] A. H. Chamseddine, R. L. Arnowitt, P. Nath, *Locally Supersymmetric Grand Unification*, Phys. Rev. Lett. **49** (1982)

[43] R. Barbieri, S. Ferrara, C. A. Savoy, *Gauge Models with Spontaneously Broken Local Supersymmetry*, Phys. Lett. **119B** (1982)

[44] L. J. Hall, J. D. Lykken, S. Weinberg, *Supergravity as the Messenger of Supersymmetry Breaking*, Phys. Rev. **D27** (1983)

[45] S. Dimopoulos, D. W. Sutter, *The Supersymmetric flavor problem*, Nucl. Phys. **B452** (1995)

[46] H. E. Haber, *The Status of the minimal supersymmetric standard model and beyond*, Nucl. Phys. Proc. Suppl. **62** (1998)

[47] A. Djouadi, et al. (MSSM Working Group), *The Minimal supersymmetric standard model: Group summary report* (1998), arXiv:hep-ph/9901246

[48] H. Georgi, *A Model of Soft CP Violation*, Hadronic J. **1** (1978)

[49] J. F. Gunion, et al., *The Higgs hunter's guide*, volume 80, Brookhaven Nat. Lab. (1989)

[50] H. E. Haber, G. L. Kane, T. Sterling, *The Fermion Mass Scale and Possible Effects of Higgs Bosons on Experimental Observables*, Nucl. Phys. **B161** (1979)

[51] L. J. Hall, M. B. Wise, *Flavor Changing Higgs-Boson Couplings*, Nucl. Phys. **B187** (1981)

[52] J. F. Donoghue, L. F. Li, *Properties of Charged Higgs Bosons*, Phys. Rev. **D19** (1979)

[53] R. M. Barnett, et al., *Implications of a Light Higgs Scalar*, Phys. Lett. **136B** (1984)

[54] R. M. Barnett, G. Senjanovic, D. Wyler, *Tracking Down Higgs Scalars With Enhanced Couplings*, Phys. Rev. **D30** (1984)

[55] G. C. Branco, et al., *Theory and phenomenology of two-Higgs-doublet models*, Phys. Rept. **516** (2012)

[56] LHC Higgs Cross Section Working Group, *Handbook of LHC Higgs Cross Sections: 4. Deciphering the Nature of the Higgs Sector* (2016), arXiv:1610.07922

[57] M. J. Dolan, C. Englert, M. Spannowsky, *Higgs self-coupling measurements at the LHC*, JHEP **10** (2012)

[58] J. Baglio, et al., *The measurement of the Higgs self-coupling at the LHC: theoretical status*, JHEP **04** (2013)

[59] O. Brüning, *Vol. 1: LHC main ring*, LHC design report (2004)

[60] L. Evans, P. Bryant, *LHC Machine*, JINST **3** (2008)

[61] *LEP Design Report: Vol.2. The LEP Main Ring* **(CERN-LEP-84-01)** (1984)

[62] L. Evans, P. Bryant, *LHC Machine*, JINST **3** (2008)

[63] M. Lamont, *Status of the LHC*, J.Phys.Conf.Ser. **455(1)** (2013)

[64] J. P. Blewett, *200-GeV Intersecting Storage Accelerators*, eConf **C710920** (1971)

[65] ATLAS Collaboration, *The ATLAS Experiment at the CERN Large Hadron Collider*, JINST **3** (2008)

[66] CMS Collaboration, *The CMS experiment at the CERN LHC*, JINST **3** (2008)

[67] A. A. Alves Jr., et al. (LHCb), *The LHCb Detector at the LHC*, JINST **3** (2008)

[68] K. Aamodt, et al. (ALICE), *The ALICE experiment at the CERN LHC*, JINST **3** (2008)

[69] ATLAS Collaboration, *Technical Design Report for the Phase-I Upgrade of the ATLAS TDAQ System* **(CERN-LHCC-2013-018. ATLAS-TDR-023)** (2013)

[70] S. Höche, *Introduction to parton-shower event generators*, in *TASI* (2015), arXiv:1411.4085

[71] A. Buckley, et al., *General-purpose event generators for LHC physics*, Phys. Rept. **504** (2011)

[72] ATLAS Collaboration, *The ATLAS Simulation Infrastructure*, Eur. Phys. J. **C70** (2010)

[73] S. Agostinelli, et al. (GEANT4), *GEANT4: A Simulation toolkit*, Nucl. Instrum. Meth. **A506** (2003)

[74] ATLAS Collaboration, *Performance of the Fast ATLAS Tracking Simulation (FATRAS) and the ATLAS Fast Calorimeter Simulation (FastCaloSim) with single particles* **(ATL-SOFT-PUB-2014-001)** (2014)

[75] ATLAS Collaboration, *The simulation principle and performance of the ATLAS fast calorimeter simulation FastCaloSim* **(ATL-PHYS-PUB-2010-013)** (2010)

[76] G. C. Blazey, et al., *Run II jet physics*, in *QCD and weak boson physics in Run II*

[77] S. Catani, et al., *Longitudinally invariant K_t clustering algorithms for hadron hadron collisions*, Nucl. Phys. **B406** (1993)

[78] S. D. Ellis, D. E. Soper, *Successive combination jet algorithm for hadron collisions*, Phys. Rev. **D48** (1993)

[79] Y. L. Dokshitzer, et al., *Better jet clustering algorithms*, JHEP **08** (1997)

[80] M. Cacciari, G. P. Salam, G. Soyez, *The Anti-k(t) jet clustering algorithm*, JHEP **04** (2008)

[81] J. Thaler, K. Van Tilburg, *Identifying Boosted Objects with N-subjettiness*, JHEP **03** (2011)

[82] A. J. Larkoski, G. P. Salam, J. Thaler, *Energy Correlation Functions for Jet Substructure*, JHEP **06** (2013)

[83] A. J. Larkoski, I. Moult, D. Neill, *Power Counting to Better Jet Observables*, JHEP **12** (2014)

[84] A. J. Larkoski, I. Moult, D. Neill, *Analytic Boosted Boson Discrimination*, JHEP **05** (2016)

[85] ATLAS Collaboration, *Search for Higgs boson pair production in the final state of $\gamma\gamma WW^*(\to l\nu jj)$ using 13.3 fb^{-1} of pp collision data recorded at $\sqrt{s}$ = 13 TeV with the ATLAS detector* **(ATLAS-CONF-2016-071)** (2016)

[86] ATLAS Collaboration, *Search for Higgs boson pair production in the $b\bar{b}\gamma\gamma$ final state using pp collision data at $\sqrt{s} = 13$ TeV with the ATLAS detector* **(ATLAS-CONF-2016-004)** (2016)

[87] R. Brun, F. Rademakers, *ROOT - An Object Oriented Data Analysis Framework*, Nucl. Inst. Meth. in Phys. Res. **A 389** (1997)

[88] K. Cranmer, et al. (ROOT), *HistFactory: A tool for creating statistical models for use with RooFit and RooStats* **(CERN-OPEN-2012-016)** (2012)

[89] J. Alwall, et al., *The automated computation of tree-level and next-to-leading order differential cross sections, and their matching to parton shower simulations*, JHEP **07** (2014)

[90] J. Gao, et al., *CT10 next-to-next-to-leading order global analysis of QCD*, Phys. Rev. D **89** (2014)

[91] M. Bahr, et al., *Herwig++ Physics and Manual*, Eur. Phys. J. **C58** (2008)

[92] S. Gieseke, C. Rohr, A. Siodmok, *The Underlying Event in Herwig++*, in *DIS* (2012), arXiv:1206.2205

[93] S. Gieseke, C. Rohr, A. Siodmok, *Colour reconnections in Herwig++*, Eur. Phys. J. **C72** (2012)

[94] J. Pumplin, et al., *New generation of parton distributions with uncertainties from global QCD analysis*, JHEP **07** (2002)

[95] S. Alioli, et al., *A general framework for implementing NLO calculations in shower Monte Carlo programs: the POWHEG BOX*, JHEP **06** (2010)

[96] T. Sjostrand, S. Mrenna, P. Z. Skands, *A Brief Introduction to PYTHIA 8.1*, Comput. Phys. Commun. **178** (2008)

[97] ATLAS Collaboration, *Example ATLAS tunes of Pythia8, Pythia6 and Powheg to an observable sensitive to Z boson transverse momentum*

[98] ATLAS Collaboration, *ATLAS Run 1 Pythia8 tunes* **(ATL-PHYS-PUB-2014-021)** (2014)

[99] R. D. Ball, et al., *Parton distributions with LHC data*, Nucl. Phys. **B867** (2013)

[100] ATLAS Collaboration, *Luminosity determination in pp collisions at $\sqrt{s}$ = 8 TeV using the ATLAS detector at the LHC*, Eur. Phys. J. **C76(12)** (2016)

[101] ATLAS Collaboration, *Searches for Higgs boson pair production in the hh $\rightarrow$ $bb\tau\tau, \gamma\gamma WW^*, \gamma\gamma bb, bbbb$ channels with the ATLAS detector*, Phys. Rev. **D92** (2015)

[102] ATLAS Collaboration, *Measurement of the photon identification efficiencies with the ATLAS detector using LHC Run-1 data*, Eur. Phys. J. **C76(12)** (2016)

[103] ATLAS Collaboration, *Electron efficiency measurements with the ATLAS detector using 2012 LHC proton–proton collision data*, Eur. Phys. J. **C77(3)** (2017)

[104] ATLAS Collaboration, *Muon reconstruction performance of the ATLAS detector in proton–proton collision data at* $\sqrt{s}$ *=13 TeV*, Eur. Phys. J. **C76(5)** (2016)

[105] ATLAS Collaboration, *Monte Carlo Calibration and Combination of In-situ Measurements of Jet Energy Scale, Jet Energy Resolution and Jet Mass in ATLAS* **(ATLAS-CONF-2015-037)** (2015)

[106] ATLAS Collaboration, *Jet Calibration and Systematic Uncertainties for Jets Reconstructed in the ATLAS Detector at* $\sqrt{s} = 13$ *TeV* **(ATL-PHYS-PUB-2015-015)** (2015)

[107] ATLAS Collaboration, *Performance of b-Jet Identification in the ATLAS Experiment*, JINST **11(04)** (2016)

[108] G. Cowan, et al., *Asymptotic formulae for likelihood-based tests of new physics*, Eur. Phys. J. **C71** (2011), [Erratum: Eur. Phys. J.C73,2501(2013)]

[109] K. Pearson, *On the Criterion That a Given System of Deviations from the Probable in the Case of a Correlated System of Variables Is Such That It Can Be Reasonably Supposed to Have Arisen from Random Sampling*, Phil. Mag. Series **5(50)** (1900)

[110] J. F. Beirer, *Search for di-Higgs production in the* $\gamma\gamma WW^*$ *decay channel in the boosted topology* **(II. Physik-UniGö-BSc-2017/04)** (2017)

[111] A. L. Read, *Presentation of search results: The CL(s) technique*, J. Phys. **G28** (2002)

[112] ATLAS Collaboration, *Performance of the ATLAS Trigger System in 2010*, Eur. Phys. J. **C72** (2012)

[113] ATLAS Collaboration, *Summary of ATLAS Pythia 8 tunes* **(ATL-PHYS-PUB-2012-003)** (2012)

[114] A. D. Martin, et al., *Parton distributions for the LHC*, Eur. Phys. J. **C63** (2009)

[115] T. Gleisberg, et al., *Event generation with SHERPA 1.1*, JHEP **02** (2009)

Erklärung nach §17(9) der Prüfungsordnung für den Bachelor-Studiengang Physik und den Master-Studiengang Physik an der Universität Göttingen:

Hiermit erkläre ich, dass ich diese Abschlussarbeit selbständig verfasst habe, keine anderen als die angegebenen Quellen und Hilfsmittel benutzt habe und alle Stellen, die wörtlich oder sinngemäß aus veröffentlichten Schriften entnommen wurden, als solche kenntlich gemacht habe.
Darüberhinaus erkläre ich, dass diese Abschlussarbeit nicht, auch nicht auszugsweise, im Rahmen einer nichtbestandenen Prüfung an dieser oder einer anderen Hochschule eingereicht wurde.

Göttingen, den 5. Februar 2018

(Kira Abeling)